Spectroscopy and Kinetics of Atmospheric and Astrochemical Reactions

Thesis by

Joseph Peter Herman Messinger

In Partial Fulfillment of the Requirements for
the degree of
Doctor of Philosophy

Caltech

CALIFORNIA INSTITUTE OF TECHNOLOGY
Pasadena, California

2021
(Defended October 27, 2020)

Joseph Peter Herman Messinger
ORCID: 0000-0001-7305-3945

ACKNOWLEDGEMENTS

Of all the parts of my thesis, the acknowledgements may (somehow) be one of the trickiest to write – how does one distill everything that went into producing this thesis?

To start off, I clearly need to acknowledge my advisor, Mitchio Okumura, for helping me become a better scientist, but also allowing me the freedom to pursue my own interests along the way. One of the best things about the Okumura group is everyone's willingness to help each other whenever someone asks. Back when I first joined the group, I was trained largely by Laura Mertens and Matt Smarte, who were incredibly valuable mentors. The other senior students in the group when I joined – Linhan Shen, Aileen Hui, and Elizabeth Lunny – I never formally worked on projects with, but they were also willing to help me whenever I needed it. I trained two undergrads during my time here, Jamie Vinson and Sylvia Meng, as well as rotating student Haw-Wei Lin, all of whom were fantastic. More recently, I've worked with Wen Chao and briefly with Charlie Markus to pass on my CRDS, and I'm sure they'll be able to do some fantastic things with it. The rest of the group I've overlapped with, Doug Ober, Greg Jones, Hannah Szentkuti, Tzu-Lynn Chen, Matt Cich and Leah Stevenson, are all great and kind scientists as well.

Another incredibly important figure during my degree is Ian Sims, who I was lucky enough to work with during the year I spent in Rennes, France, working in the Institut de Physique de Rennes at the University of Rennes 1. This time was incredible, both on a professional level, where I busted out a lot of data, and on a personal level, as someone who has never really had the opportunity to travel prior. I worked with a great team there; much of my work was in collaboration with Ilsa Cooke, Divita Gupta, and Omar Abdelkader Khedaoui. While I worked closely with all of them on taking and analyzing the CRESU data, Divita also performed the theoretical calculations and Omar designed many of the low temperature N_2 Laval nozzles that were critical to the work in Chapter 5 on the OH + CO Reaction. Other members of the team included Théo Guillaume, Brian Hays and Tom Hearne, all of whom were also tremendously helpful both scientifically and with navigating the French system. The rest of the large IPR team were all incredible as well, particularly Sébastien Le Picard and his student Olivier Durif, who I assisted with on experiments at the SOLEIL synchrotron.

I've been lucky enough to have assistance from many others throughout my degree as well. In particular, Stan Sander and Fred Winiberg from JPL have always been willing to help me and provide feedback whenever I've needed it. More recently, work with John Barker from the University of Michigan, John Stanton and Lam Nguyen, both from University of Florida, has been crucial in understanding our experimental results on the OH + CO reaction.

Of course, I'd also like to thank my committee – John Seinfeld, Geoff Blake and Brian Stoltz, for all of the helpful conversations, guidance and support they've given me throughout my time in graduate school.

Caltech and the Chemistry option are really kept running by the staff. In particular, Alison Ross has been one of the most helpful resources in my graduate career, always willing to offer me help or point me in the right direction (or just talk about knitting). Her predecessor, Agnes Tong, was likewise incredibly supportive. For dealing with Okumura group logistics, our administrative assistants, Monica Brito and Elisha Jung Okawa have always been able to help me. The facilities people, especially Joe Drew, have quickly solved any problems I've had. Nate Siladke, as the safety officer, has been a key resource in making the department and lab safer. I'd also like to thank Doug Rees and Kate McAnulty from Graduate Studies Office for their help over the years as well.

I probably wouldn't have made it through my PhD without the support from all of my friends and family. As members of the same Chemistry cohort as me, Jeremy Tran and Mary Arrastia were two of the first people I met at Caltech and I have many good memories of us exploring different restaurants/playing games/watching dumb videos/complaining about our experiments/reading over each other's work that they were instrumental to my graduate school experience. Crysta Song was one of my first friends at Amherst, and I was so delighted when she moved out to LA. I learned a lot from Olivia Wilkins, especially about astrochemistry, and have been so impressed by her advocacy work. I was a member of the CGSC for a number of years and was happy to work with others with strong opinions and the desire to make Caltech better. And of course, my parents and sister have been so supportive and proud of me every step of the way.

My PhD work has been funded by the NSF GRFP Fellowship, the NSF GROW Fellowship and the Chateaubriand Fellowship from the Embassy of France in the United States. This work was supported by the National Science Foundation Grant CHE-1413712, National Aeronautics and Space administration, Upper Atmospheric Research Program, Contract NNX12AE01G and Solar Systems Workings Program, Contract .80NSSC18K0263, and the Petroleum Research Fund of the American Chemical Society. Work in collaboration with the University of Rennes 1 was supported by the European Union's Horizon 2020 research and innovation programme under the European Research Council (ERC) grant agreement 695724-CRESUCHIRP, the European Regional Development Fund, the Region of Brittany and Rennes Metropole and the French National Programme "Physique et Chimie du Milieu Interstellaire" (PCMI) of CNRS/INSU with INC/INP co-funded by CEA and CNES.

ABSTRACT

The reactions between reactive radicals and other neutral compounds have long been known to be important in atmospheric chemistry and astrochemistry. This work uses pulsed-laser photolysis cavity ringdown spectroscopy and laser-induced fluorescence to measure the rate constants and branching ratios of chemical reactions over a wide range of temperatures and pressures relevant to both polluted atmospheres, and the interstellar medium. This includes studying the OH + NO_2 reaction in the 253 – 333 K range, the reaction of CN with benzene (C_6H_6) and toluene (C_7H_8) down to 16 K, and the OH + CO reaction down to 30 K.

PUBLISHED CONTENT AND CONTRIBUTIONS

Messinger, J. P.; Gupta, D.; Cooke, I. R.; Okumura, M.; Sims, I. R. “Rate constants of the CN + Toluene Reaction from 16 – 294 K and Interstellar Implications” *Journal of Physical Chemistry A* 124, 39, 7950-7958 (2020). DOI: https://doi.org/10.1021/acs.jpca.0c06900

J. P. M. participated in conception of project, experimental measurements, data analysis and wrote the manuscript.

Cooke, I. R., Gupta, D., Messinger, J. P., Sims, I. R. “Benzonitrile as a Proxy for Benzene in the Cold ISM: Low-temperature Rate Coefficients for CN + C_6H_6” *Astrophysical Journal Letters* 891:L41 (2020). DOI: https://doi.org/10.3847/2041-8213/ab7a9c

J. P. M. participated in experimental measurements and data analysis

TABLE OF CONTENTS

LIST OF FIGURES AND TABLES

Chapter 1

Chapter 2

Chapter 3

Chapter 4

Chapter 5

Chapter 1 – Introduction

1.1 – Scientific Background

Knowledge of gas phase compounds and their chemical reactions are pivotal to our understanding of chemistry. The conditions these molecules are in can vary dramatically, from temperatures as low as 10 K in the depths of the interstellar medium, to more than 1000 K in the combustion of hydrocarbons in engines. The chemistry in these systems is dominated by highly reactive, unstable compounds, leading to fast and complex chemistry occurring. In order to accurately understand these systems, we must be able to observe these unstable species and measure the kinetics of their formation and destruction. While molecular spectra and reaction rate constants of these reactive compounds can be computed with theoretical calculations, they must be benchmarked with experimental measurements to determine their accuracy. To that end, one major focus in experimental gas phase chemistry is to better understand these unstable molecules and their reactions in systems such as atmospheric chemistry and astrochemistry.

1.1a – Atmospheric Chemistry

Understanding Earth's atmosphere and the chemistry behind it has been a major topic in gas phase chemistry since the mid-20th century, when the impact of fossil fuel usage and air pollution resulting from the Industrial Revolution became apparent. The dominant molecule in Earth's atmosphere is N_2 (77% of the atmosphere) followed by O_2 (21%) and argon (1%). The remaining components are largely stable molecules, such as CO_2 and H_2O.

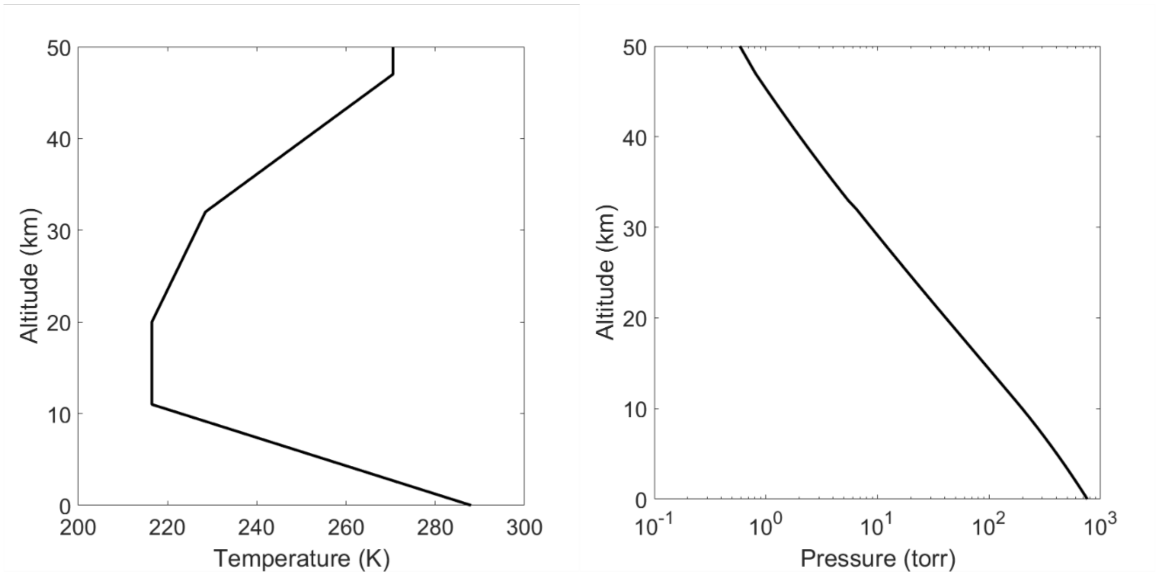

Figure 1.1: The average temperature (left) and pressure (right) profiles of the Earth's lower atmosphere, consisting of the troposphere and stratosphere.

Earth's atmosphere is divided into different regions, the lowest of which are the troposphere (roughly 0 – 18 km), and the stratosphere (roughly 18 – 50 km). The tropopause is the boundary layer between the two and is roughly 11 – 18 km in height. The exact location of the tropopause and the boundary above the stratosphere changes with the longitude and latitude. The average temperatures and pressures within the troposphere, tropopause and stratosphere is shown in Figure 1.1. Much of the reactive chemistry in the troposphere and stratosphere originates from the photolysis of O_3 by short wavelengths of sunlight,[1] which results in the formation of $O(^1D)$

$O_3 + h\nu\ (\lambda < 340\ \text{nm}) \rightarrow O(^1D) + O_2$ (R1.1)

This $O(^1D)$ can subsequently be quenched through collision with a nonreactive partner, such as N_2, or react with H_2O:

$O(^1D) + M \rightarrow O(^3P) + M$ (R1.2)

$O(^1D) + H_2O \rightarrow 2OH$ (R1.3)

In addition to the OH radical, NO_3 and O_3 are also important oxidizers throughout the atmosphere, particularly during night, when no OH is formed through R1.1-R1.3 due to the lack of sunlight.[2]

The subsequent chemistry of the OH radical is closely linked to HO_2 chemistry, so for this reason, OH and HO_2 are collectively known as HO_x. There is rapid cycling between the two, through reactions

$$OH + CO (+ O_2) \rightarrow HO_2 + CO_2 \quad (R1.4)$$

$$OH + O_3 \rightarrow HO_2 + O_2 \quad (R1.5)$$

and

$$HO_2 + NO \rightarrow OH + NO_2 \quad (R1.6)$$

$$HO_2 + O_3 \rightarrow OH + 2O_2 \quad (R1.7)$$

In urban environments, where high pollution leads to the presence of large amounts of NO and NO_2 (collectively known as NO_x), the termolecular reaction of OH is important

$$OH + NO + M \rightarrow HONO + M \quad (R1.8)$$

$$OH + NO_2 + M \rightarrow HONO_2 + M \quad (R1.9)$$

These reactions serve as a sink of OH. While HONO can photolyze to reform OH and NO readily, $HONO_2$ is largely stable, and so R1.9 is an important reservoir of HO_x.[3]

Another important sink for the OH radical is the reaction with hydrocarbons, which are constantly emitted into the atmosphere through both anthropogenic and biogenic sources. Depending on the structure of the hydrocarbon, OH can either abstract a hydrogen, such as in the reaction with CH_4, or add to an unsaturated bond, such as in the reaction with isoprene (C_5H_8, 2-methyl-1,3-butadiene). Both of these mechanisms lead to formation of an alkyl peroxy radical, RO_2

$OH + RH (+ O_2) \rightarrow RO_2$ (R1.10)

The chemistry of these RO_2 compounds is complex and an active area of study in atmospheric chemistry. In urban areas with high NO_x concentrations, the most common reaction is

$RO_2 + NO \rightarrow RO + NO_2$ (R1.11)

$RO + O_2 \rightarrow HO_2 + R`CHO$ (R1.12)

where R`CHO is an aldehyde species. Note the reformation of HO_x through R1.12, which leads to additional formation of OH. In low NO_x environments, the most common fates of RO_2 are reactions with HO_2 or other RO_2 molecules.

$RO_2 + HO_2 \rightarrow ROOH + O_2$ (R1.13)

$RO_2 + RO_2 \rightarrow ROOR + O_2$ (R1.14)

$RO_2 + RO_2 \rightarrow RO + RO + O_2$ (R1.15)

$RO_2 + RO_2 \rightarrow ROH + R`CHO + O_2$ (R1.16)

The two RO_2 reactants in R1.14 – R1.16 may or may not have the same alkyl group. Like in the high NO_x case, many of these reactions lead to the reformation of HO_x, through R1.12 or the photolysis of ROOH to form RO and OH. Recent work on RO_2 radicals in low NO_x environments has also shown that isomerization, through intramolecular hydrogen atom transfers, can play an important role in the formation of highly oxygenated molecules (HOMs).[4]

$RO_2 \rightarrow QOOH$ (R1.17)

$QOOH + O_2 \rightarrow OOQOOH$ (R1.18)

The subsequent chemistry of the OOQOOH radical leads to the formation of stable HOMs, which are important precursors in secondary organic aerosols (SOAs) due to their low vapor pressure. Recent work has also suggested that the ROOR accretion products from R1.14 are also important HOMs.[5]

The reaction network of the troposphere and stratosphere is complex, and the reaction rates and product branching ratios must be accurately determined. These parameters are used in widely used atmospheric models and influence policy decisions. While many of these reactions have been well characterized, models are still unable to match field measurements, particularly measurements of the concentration of the OH radical in low NO_x environments.[1, 6] leading to the need for further refinement and evaluation of the experimental values.

1.1b – Astrochemistry

The interstellar medium (ISM), the diffuse material present in space that is not part of stars or other large celestial bodies, holds about 10 – 15% of the total mass of our galaxy.[7] This mass consists of both gasses (atoms, molecules, ions and electrons) and solids (dust or ice particles). Despite the diffusivity of the ISM, discrete clouds can form. Molecular clouds are cold, with temperatures of 10 – 20 K and gas densities of $10^2 – 10^6$ cm^{-3}, while atomic clouds can be either cold (50 – 100 K, 20 – 50 cm^{-3}) or hot ($6 \times 10^3 – 10^4$ K, 0.2 – 0.5 cm^{-3}).[7] Larger molecular clouds are on the order of tens of parsecs (1 parsec = 3.09×10^{16} meters) with densities of $10^2 – 10^3$ cm^{-3}, while smaller molecular clouds are denser, with sizes of tenths of parsecs and densities of $10^4 – 10^6$ cm^{-3}.[7]

The earliest molecules detected in the ISM date to observations made in the late 1930s of small molecules such as CH, CN and CH^+ with optical spectroscopy.[7] The advent of radio astronomy, allowing molecules to be detected through their rotational transitions, has allowed for many new discoveries in the ISM. To date, over 200 molecules have been discovered in the ISM, from small diatomics to compounds as large as C_{60} and C_{70} (though the majority of detected species contain ten atoms or less).[8] H_2 is by far the most common molecule in the ISM, while CO is the second most abundant, with the CO/H_2 fraction ranging from $10^{-7} – 10^{-5}$.[9] As H_2 has no permanent dipole moment, CO is commonly used as a tracer for identifying cold molecular clouds in the ISM. With the advent of new and more sensitive telescopes such as Atacama Large Millimeter/submillimeter Array (ALMA) and the upcoming James Webb Space Telescope, our knowledge of molecules in the ISM and their distribution is rapidly expanding.

The extreme conditions present in the ISM leads to the presence of large amounts of unstable species in the ISM. Radiation from cosmic rays leads to complex ion chemistry, much of which is driven through the ionization of hydrogen, which subsequently leads to the formation of H_3^+, which subsequently reacts with other atoms and molecules to produce a wide array of cations.[10] Anions are formed through radiative attachment of electrons to neutral atoms and molecules, and subsequent chemical reactions of these anions.[11] The low temperature means that unstable compounds are not able to isomerize to more stable isomers, leading to the high abundance of molecules such as HNC.[12]

Many of the molecules detected in the ISM are neutral radicals, from the early discovered molecules such as CH and CN, to molecules as large as C_8H.[8] While ion chemistry has historically dominated chemical networks for astrochemistry, many reactions between these neutral radicals and neutral closed-shell compounds have been shown to be fast at low temperatures.[13] The rate constants of many of these neutral-neutral display non-Arrhenius behavior at the low temperatures relevant to the ISM. An extreme example of these non-Arrhenius rate constants is the turn-around displayed by a number of reactions, where the rate constant reaches a minimum, before becoming faster at lower temperatures. This has been seen in the rate constants of the CN radical with hydrocarbons such as ethane (C_2H_6)[14] and rate constants of OH with oxygenated hydrocarbons such as methanol (CH_3OH)[15-16] and ethanol (CH_3CH_2OH)[17-20], the latter of which can be seen in Figure 1.2. Therefore, measurements of the rate constants of reactions relevant to the ISM must be studied down to the relevant temperatures and can not necessarily be extrapolated from higher temperature experiments.

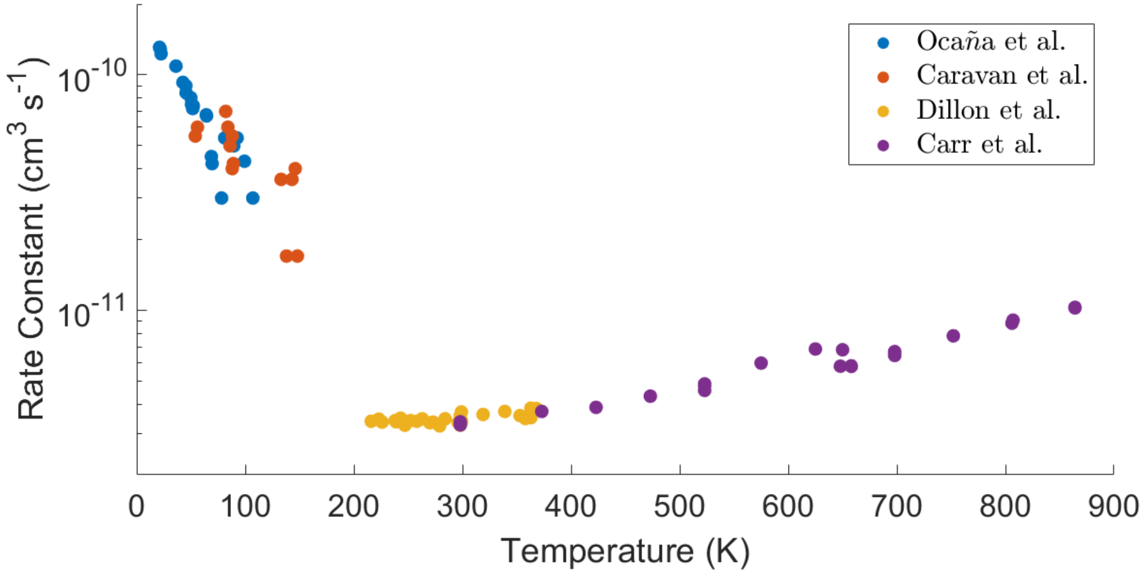

Figure 1.2: The rate constants of the OH + CH_3CH_2OH reaction over the 10 – 900 K range showing the minimum at ~200 K. Data taken from Ocaña et al.,[17] Caravan et al.,[18] Dillon et al.,[19] and Carr et al.[20]

1.2 – Summary of Thesis Work

This work presented here covers experiments done at Caltech and the University of Rennes 1 to study the temperature-dependent spectroscopy and kinetics of radical reactions with neutral species relevant to atmospheric and astrochemistry. Chapter 2 covers the experimental techniques used throughout this thesis. Chapter 3 discusses mid-infrared cavity ringdown spectroscopy experiments of the temperature- and pressure- dependent branching ratio of the OH + NO_2 reaction at conditions relevant to atmospheric chemistry. This reaction is critical in determining ozone formation in urban environments, which is a major component of smog. Chapter 4 discusses the rate constants of the reactions of the CN radical with benzene and toluene down to 15 K, as inspired by the 2018 detection of benzonitrile in the ISM.[21] Chapter 5 focuses on the rate constants of the reaction of OH and CO, two of the most abundant interstellar molecules, down to 30 K, and the unusual temperature dependence of the reaction.

1.3 – References

1. Stone, D.; Whalley, L. K.; Heard, D. E., Tropospheric OH and HO_2 Radicals: Field Measurements and Model Comparisons. *Chem Soc Rev* **2012**, *41*, 6348-6404.

2. Brown, S. S.; Stutz, J., Nighttime Radical Observations and Chemistry. *Chem Soc Rev* **2012**, *41*, 6405-6447.

3. Seinfeld, J. H.; Pandis, S. N., *Atmospheric Chemistry and Physics : From Air Pollution to Climate Change*, Third edition. ed.; John Wiley & Sons, Inc.: Hoboken, New Jersey, 2016, p xxvi, 1120 pages.

4. Crounse, J. D.; Nielsen, L. B.; Jorgensen, S.; Kjaergaard, H. G.; Wennberg, P. O., Autoxidation of Organic Compounds in the Atmosphere. *J Phys Chem Lett* **2013**, *4*, 3513-3520.

5. Berndt, T.; Scholz, W.; Mentler, B.; Fischer, L.; Herrmann, H.; Kulmala, M.; Hansel, A., Accretion Product Formation from Self- and Cross-Reactions of RO_2 Radicals in the Atmosphere. *Angew Chem Int Edit* **2018**, *57*, 3820-3824.

6. Ferracci, V.; Heimann, I.; Abraham, N. L.; Pyle, J. A.; Archibald, A. T., Global Modelling of the Total OH Reactivity: Investigations on the "Missing" OH Sink and Its Atmospheric Implications. *Atmos Chem Phys* **2018**, *18*, 7109-7129.

7. Ferriere, K. M., The Interstellar Environment of Our Galaxy. *Rev Mod Phys* **2001**, *73*, 1031-1066.

8. McGuire, B. A., 2018 Census of Interstellar, Circumstellar, Extragalactic, Protoplanetary Disk, and Exoplanetary Molecules. *Astrophys J Suppl S* **2018**, *239*.

9. Burgh, E. B.; France, K.; McCandliss, S. R., Direct Measurement of the Ratio of Carbon Monoxide to Molecular Hydrogen in the Diffuse Interstellar Medium. *Astrophys J* **2007**, *658*, 446-454.

10. Herbst, E., The Astrochemistry of H_3^+. *Philos T R Soc A* **2000**, *358*, 2523-2533.

11. Millar, T. J.; Walsh, C.; Field, T. A., Negative Ions in Space. *Chem Rev* **2017**, *117*, 1765-1795.

12. Graninger, D. M.; Herbst, E.; Oberg, K. I.; Vasyunin, A. I., The HNC/HCN Ratio in Star-Forming Regions. *Astrophys J* **2014**, *787*.

13. Smith, I. W. M.; Herbst, E.; Chang, Q., Rapid Neutral-Neutral Reactions at Low Temperatures: A New Network and First Results for TMC-1. *Mon Not R Astron Soc* **2004**, *350*, 323-330.

14. Sims, I. R.; Queffelec, J. L.; Travers, D.; Rowe, B. R.; Herbert, L. B.; Karthauser, J.; Smith, I. W. M., Rate Constants for the Reactions of CN with Hydrocarbons at Low and Ultra-Low Temperatures. *Chem Phys Lett* **1993**, *211*, 461-468.

15. Shannon, R. J.; Blitz, M. A.; Goddard, A.; Heard, D. E., Accelerated Chemistry in the Reaction between the Hydroxyl Radical and Methanol at Interstellar Temperatures Facilitated by Tunnelling. *Nat Chem* **2013**, *5*, 745-749.

16. Antinolo, M.; Agundez, M.; Jimenez, E.; Ballesteros, B.; Canosa, A.; El Dib, G.; Albaladejo, J.; Cernicharo, J., Reactivity of OH and CH_3OH between 22 and 64 K: Modeling the Gas Phase Production of CH_3O in Barnard 1b. *Astrophys J* **2016**, *823*.

17. Ocana, A. J.; Blazquez, S.; Ballesteros, B.; Canosa, A.; Antinolo, M.; Albaladejo, J.; Jimenez, E., Gas Phase Kinetics of the OH + CH_3CH_2OH Reaction at Temperatures of the Interstellar Medium (T=21-107 K). *Phys Chem Chem Phys* **2018**, *20*, 5865-5873.

18. Caravan, R. L.; Shannon, R. J.; Lewis, T.; Blitz, M. A.; Heard, D. E., Measurements of Rate Coefficients for Reactions of OH with Ethanol and Propan-2-ol at Very Low Temperatures. *J Phys Chem A* **2015**, *119*, 7130-7137.

19. Dillon, T. J.; Holscher, D.; Sivakumaran, V.; Horowitz, A.; Crowley, J. N., Kinetics of the Reactions of HO with Methanol (210-351 K) and with Ethanol (216-368 K). *Phys Chem Chem Phys* **2005**, *7*, 349-355.

20. Carr, S. A.; Blitz, M. A.; Seakins, P. W., Site-Specific Rate Coefficients for Reaction of OH with Ethanol from 298 to 900 K. *J Phys Chem A* **2011**, *115*, 3335-3345.

21. McGuire, B. A.; Burkhardt, A. M.; Kalenskii, S.; Shingledecker, C. N.; Remijan, A. J.; Herbst, E.; McCarthy, M. C., Detection of the Aromatic Molecule Benzonitrile (c-C_6H_5CN) in the Interstellar Medium. *Science* **2018**, *359*, 202-205.

Chapter 2 – Experimental Methods

2.1 – Detection Methods

A chemical reaction can be studied through monitoring the reactants, intermediates, products, or some combination thereof, depending on the nature of the reaction and the method involved. Consequently, many different techniques have been developed, particularly for studying reactive molecules with short lifetimes and low abundances. There are generally tradeoffs in different techniques, involving a combination of the method's time resolution, sensitivity, spectral resolution, and the ability to identify different molecules.

The work presented in this thesis uses two main techniques, cavity ringdown spectroscopy (CRDS) and laser-induced fluorescence (LIF), to study the reactants and products of chemical reactions.

2.1a – Cavity Ringdown Spectroscopy

For light passing through a chemical sample, the amount of light absorbed is governed by the Beer-Lambert law, which states

$$\ln\left(\frac{I_0}{I_t}\right) = \sigma(\lambda)LN \qquad \text{(Equation 2.1)}$$

where I_0 is the initial intensity of the light, I_t is the intensity of the transmitted light after passing through the sample, σ is the cross section(s) of the sample at wavelength λ (with units of cm^2), L is the pathlength of the sample (units of cm), and N is the number density of the sample (units of cm^{-3}).

For the detection of species that have low concentrations, such as reactive radicals or products of their reactions, Equation 2.1 indicates that the trace molecule must either have a large cross section or be contained in a long chamber. The former is an inherent property of the molecule, which therefore can not be altered experimentally. One method to the increase the sample length is through cavity ringdown spectroscopy, which can produce pathlengths on the order of kilometers or more. This technique, originally developed in the 1980s, was originally based on methods to precisely and accurately measure the reflectivity of highly reflective mirrors (R > 0.9995)[1] and was first used to measure doubly forbidden electronic transitions of O_2 to demonstrate its sensitivity.[2]

CRDS has been reviewed extensively in the past.[3-4] These measurements rely on two highly reflective mirrors, often plano-concave, attached to the ends of a cell with distance L, as seen in Figure 2.1, to form an optical cavity. Light is transmitted into the cavity, bouncing back and forth between the two mirrors. As light hits each mirror, a small portion (1 – R) of the light leaks out and hits a detector. The resulting exponential decay is known as a ringdown. The intensity of the light at time *t,* $i(t)$, in an empty cavity with no absorption of the light, is governed by

$$i(t) = i_0 e^{-(1-R)\frac{tc}{L}} \qquad \text{(Equation 2.2)}$$

where i_0 is the initial intensity of the ringdown, *L* is the distance between the two mirrors, and *c* is the speed of light. The ringdown time, τ, is characterized by the time the ringdown takes to reach $i_0 e^{-1}$, which can be determined by Equation 2.1 to be

$$\tau = \frac{L}{c(1-R)} \qquad \text{(Equation 2.3)}$$

When a molecular absorber is present, the intensity at time *t* instead becomes

$$i(t) = i_0 e^{-\frac{tc}{L}[(1-R)+\sum \alpha_i L]} \qquad \text{(Equation 2.4)}$$

where α_i is the absorption coefficient of species *i* and is defined as

$$\alpha_i = \sigma_i N_i \qquad \text{(Equation 2.5)}$$

With the presence of molecular absorbers, the ringdown time therefore decreases, as the signal decays quicker than without an absorber. The ringdown time then becomes

$$\tau = \frac{L}{c[(1-R)+\sum \alpha_i L]} \qquad \text{(Equation 2.6)}$$

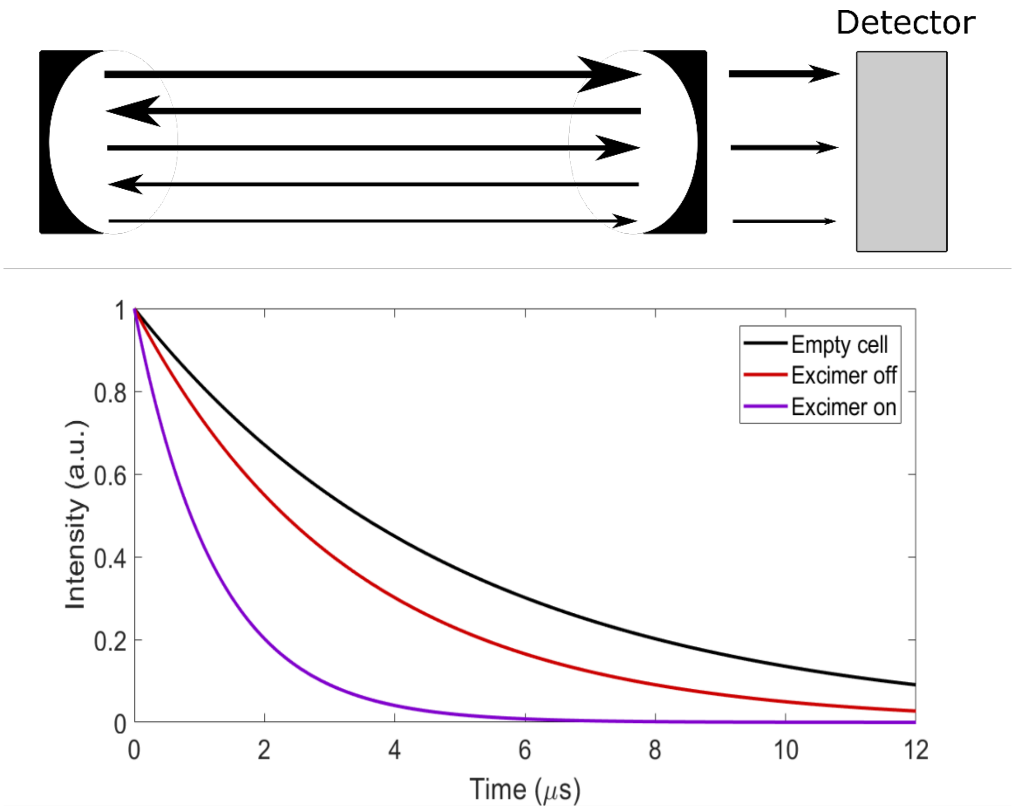

Figure 2.1: Diagram of a cavity ringdown cell (top), showing the light inside the cavity decreasing as it bounces back and forth, and simulated ringdown decays (bottom) of an empty cell (black), with precursor gases (red), and with photolysis and precursor gases (purple).

In the case where these is only one molecular absorber, Equations 2.3 and 2.6 can be combined to determine α

$$\alpha = \frac{1}{c}\left(\frac{1}{\tau_1} - \frac{1}{\tau_2}\right) \qquad \text{(Equation 2.7)}$$

where τ_1 is the ringdown time with the molecular absorber, and τ_2 is the ringdown time of the empty cavity. In the case where precursor gases are photolyzed, as in the experiments in this work, Equation 2.7 can be altered to take into account the absorbance due to the photolytic species and their resulting chemistry, as seen in Figure 2.1

$$\alpha = \frac{1}{c}\left(\frac{1}{\tau_{Photolysis\ on}} - \frac{1}{\tau_{Photolysis\ off}}\right) \qquad \text{(Equation 2.8)}$$

Since its inception, CRDS has gained widespread usage due to its sensitivity, using both pulsed and continuous sources. Many of its applications have been for studying molecules with low concentrations, such as reactive radicals, molecular clusters, or isotopologues, where the high sensitivity is required.[4] Weak transitions, such as overtones or forbidden transitions have also been extensively studied with CRDS.[2] With the development of time-dependent methods of spectral analysis, it has been used to measure reaction rate constants,[5] and for fast reactions, the Simultaneous Kinetics and Ringdown (SKaR) method has been developed.[6] Its range of application extends as far as usage in atmospheric field campaigns,[7-8] and for medical diagnostics of human breath.[9]

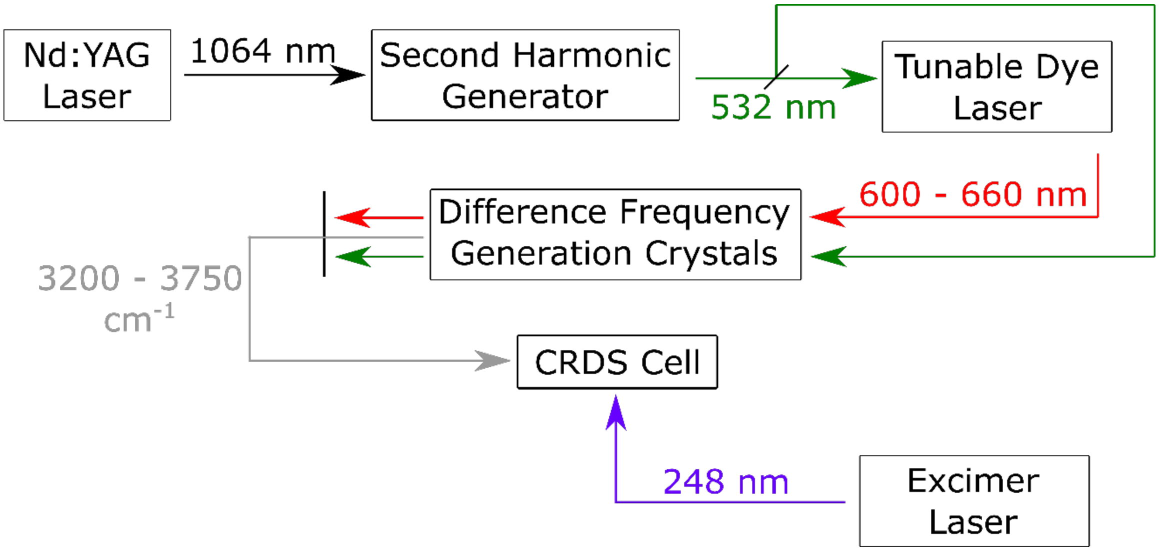

Figure 2.2: The pulsed laser photolysis, mid-infrared cavity ringdown spectrometer used in these experiments.

A schematic of the CRDS instrument used in this work can be seen in Figure 2.2. The pulsed laser used here provides a wider tunability than available in continuous lasers, at the cost of broader linewidths (estimated to be ~1 cm^{-1} in the mid-infrared design used here.) This instrument operates in the mid-infrared (3200 – 3750 cm^{-1}) to look at the OH-stretches of molecules. The second harmonic (532 nm) of a 10 Hz Nd:YAG laser (Continuum Surelite III) is passed through a 30/70 beam splitter. 30% of the 532 nm light is sent through a tunable dye laser (Quanta Ray PDL-3) containing DCM (4-(dicyanomethylene)-2-methyl-6-(4-dimethylaminostyryl)-4H-pyran, Exciton) dye in a methanol solution, producing light in the 600 – 660 nm range. This output is recombined with the remaining 70% of the 532 nm light. This then goes through two KTP (potassium titanyl phosphate) crystals, where a mid-IR photon is produced through difference frequency generation[10] and therefore has a frequency equal to that of the difference of the two pump beams. Filters block the remaining green and red beams and the mid-IR beam is sent into the CRDS cell containing ringdown mirrors with R = 0.9998 (2.8 μm, Los Gatos Research); the mirror reflectivity of these mirrors over the mid-infrared range can be seen in Figure 2.3. Perpendicularly to the CRDS axis, a KrF excimer laser (Lambda Physik LPX 210i), also operating at 10 Hz, fires at 248 nm to initiate the chemistry through pulsed laser photolysis. The resulting signal, collected for 80-100 microseconds at 25 MHz, is detected by a liquid nitrogen cooled InSb detector (Infrared Associates Inc., IS-0.50) and digitized with an analog-to-digital converter (Gage). Custom written LabView is used to collect and average 16 ringdowns, which are subsequently fit using a Levenberg-Marquadt algorithm.

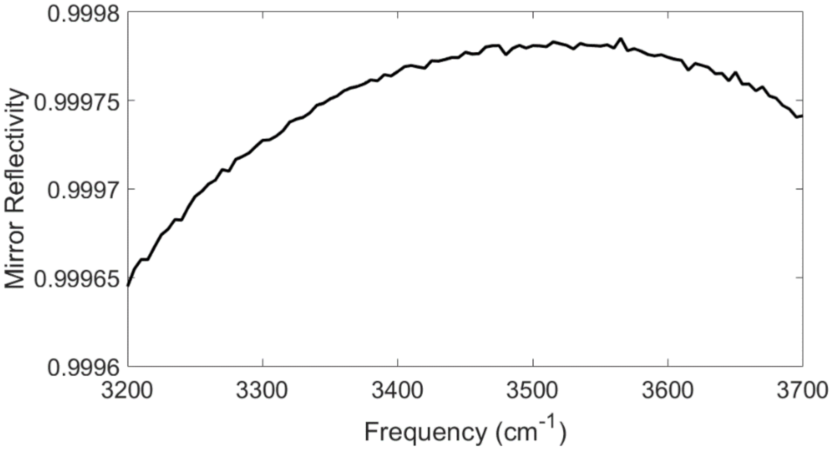

Figure 2.3: The reflectivity of the mid-infrared CRDS mirrors centered at 2.8 μm used in experiments.

2.1b – Laser-Induced Fluorescence

Laser-induced fluorescence, first developed in 1968,[11] is a method in which first, a specific transition is excited. The excited state that emits a photon through spontaneous emission (fluorescence) within a time frame of nanoseconds to microseconds, depending on the transition and conditions of the excited molecule. The emitted photon can either be at the same wavelength as the initial excitation laser, in a process known as 'on-resonance fluorescence', or at a different wavelength to end up in a different state than the initial state, known as 'off-resonance fluorescence'. Many experiments use a narrowband filter to prevent fluorescence at multiple wavelengths from being detected by the photomultiplier tube detector. An example of an off-resonance detection scheme, used to detect OH (v = 0), can be seen in Figure 2.4.

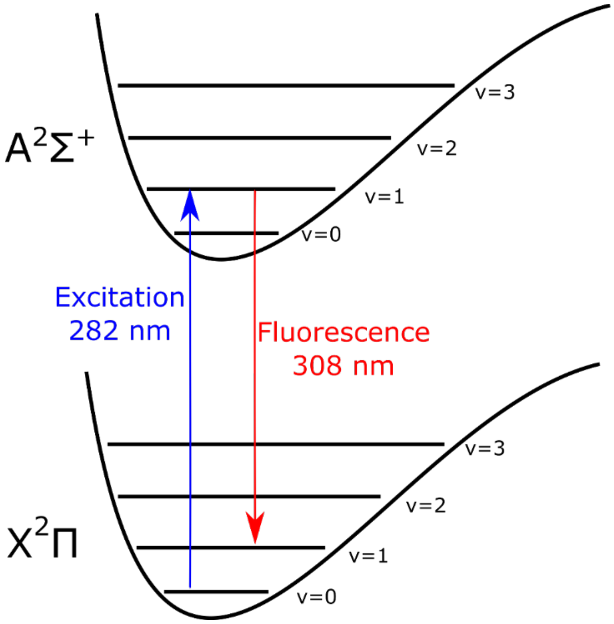

Figure 2.4: The LIF excitation and detection scheme for detecting OH (v = 0) with the $A^2\Sigma^+$ - $X^2\Pi$ electronic transition.

LIF is a highly sensitive technique and has been used to detect concentrations as low as 10^6 cm^{-3}.[12] It is commonly used in pulsed laser photolysis gas phase kinetics measurements, by varying the time delay between the photolysis laser and the LIF excitation laser, which is used to detect a reactive radical, such as OH or CN, under pseudo-first order conditions.

Two LIF excitation schemes are used in this work to detect the CN and OH (v = 0, 1) radicals. To detect the CN radical, the 355 nm third harmonic of a Nd:YAG laser (Continuum Powerlite Precision II) firing at 10 Hz is put into a dye laser (Laser Analytical Systems, , LDL 20505) containing Exalite 389 dye (Exciton) in 1,4-dioxane (Sigma Aldirch, 99.8%), to produce light at ~389 nm to excite the CN $B^2\Sigma^+$ - $X^2\Sigma^+$ (0,0) transition. Fluorescence is then detected from the (0,1) transition at ~420 nm. An excimer laser (Coherent LPXPro 210), also operating at 10 Hz, is used to initiate the radical chemistry.

Fluorescence was detected from the CN (0,1) transition at ~420 nm by a photomultiplier tube (Thorn EMI 6723) preceded by a 420 nm bandpass filter (Ealing Optics).

To detect the OH radical, the 532 nm second harmonic of a 10 Hz Nd:YAG (Continuum Powerlite Precision II) laser is used to excite a dye laser containing either Rhodamine 6G (Exciton), for OH $\nu = 0$, or a mix of Rhodamine 6G and Rhodamine B (Exicton), for $\nu = 1$, the output of which is sent through BBO doubling crystals to produce ~1 mJ of UV light to excite the OH radicals. The (1,0) and (2,1) bands of the $A^2\Sigma^+ \leftarrow X^2\Pi$ electronic transition are used to excite the OH ($\nu = 0$) and OH ($\nu = 1$) radicals, respectively, at ~282 and ~289 nm. The resulting fluorescence is detected by a photomultiplier tube proceeded by either a 310 (for OH $\nu = 0$) or 320 nm (for OH $\nu = 1$) bandpass filter. An excimer laser (Lambda Physics COMPexPro 201) operating at either 193 or 248 nm at 10 Hz is used to create the radicals of interest.

2.2 – Flow Cells

In order to study the temperature-dependence of reactions, different methods may be used depending on the desired temperature range. Here, we use a temperature-controlled flow cell for studying atmospheric chemistry experiments over the range of 253 – 333 K and 50 – 700 torr. Experiments studying astrochemical reactions use the CRESU (*Cinétique de Réaction en Ecoulement Supersonique Uniforme*; a French acronym for 'reaction kinetics in a uniform supersonic flow'), which allows for a cold flow in thermal equilibrium to temperatures as cold as a few K.

2.2a – Temperature-Controlled Flow Cell

To measure the temperature-dependent branching ratios of the OH + NO_2 reaction, a custom-designed temperature-controlled flow cell, as seen in Figure 2.5 was developed by Luis Gomez and used in this work. This flow cell uses thermoelectric coolers (TECs, TE Technologies TE-63-1.4-1.15), controlled by a temperature controller (ILX Lightwave LDT-5948) to cool or heat the cell between 253 and 333 K, as measured by a resistance temperature detector (RTD) attached to the cell. A circulator filled with water, methanol, or a mixture of the two, helps stabilize the temperature throughout the cell and reduce any temperature gradients. Before entering the cell, gas flows through a stainless-steel pre-cooling block that is also in thermal contact with the bottom of the cell.

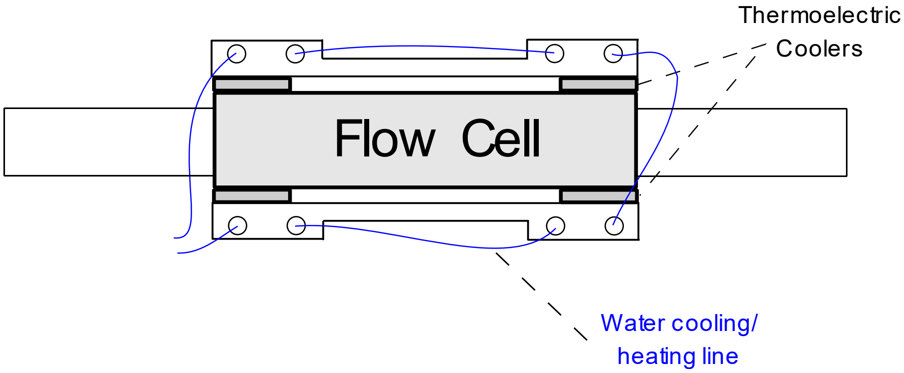

Figure 2.5: Top view of the temperature-controlled flow cell used in CRDS experiments in this work. TECs are placed on each corner of the cell. To stabilize the temperature, circulated water, methanol or mixtures thereof are in thermal contact with the cell.

2.2b – CRESU

In order to study bimolecular or termolecular reaction kinetics, the gases must be in thermal equilibrium. However, achieving this is difficult at the very cold temperatures relevant to astrochemistry (~10 K). Liquid N_2 has a temperature of 77 K,[13] and therefore cannot cool gas flows below that. Furthermore, even at 77 K and above, the wall-cooling method means that at these cold temperatures, many species with lower vapor pressures will stick to the wall upon collision. This further limits the number of reactions that can be studied through liquid N_2 cooling. One of the most common techniques for cooling molecules to < 10 K is the supersonic free jet expansion, where molecules are expanded through a narrow nozzle into a low-pressure chamber. While extensively used in spectroscopy to measure cold spectra of unstable species, the low number of collisions means the system does not reach thermal equilibrium and in fact has large temperature and pressure gradients.[14] In recent years, helium buffer gas cooling has been developed to effectively cool molecules to < 10 K,[15] but has not yet been applied to *in situ* studies of bimolecular reactions. Ultracold (500 nK) chemical reactions have been directly observed after laser cooling the reactants,[16] but the number of compounds that can be cooled to these temperatures is extremely limited.

The CRESU technique was developed in the 1980s[17] for studying astrochemical reactions and energy transfer processes and has been the subject of previous reviews[18-20]. While initially used in conjunction with a mass spectrometer to measure the rate constants of ion-neutral reactions, it has since been combined with a wide range of sensitive detection methods. CRESU flows have been used to reach temperatures as low as 6 K.[21]

Briefly, the core of the CRESU technique is the Laval nozzle (also known as a de Laval nozzle), which are specially designed convergence-divergence nozzles. Laval nozzles were originally developed in the late 19th century and have been used extensively in mechanical engineering, including in the propulsion of rockets. As can be seen in Figure 2.6A, in CRESU experiments, gas is pumped from a high pressure reservoir, typically but not always held at room temperature, through a Laval nozzle, before being isentropically expanded into a low pressure chamber at supersonic speeds. As the gas is compressed and expanded through the nozzle, it is cooled, allowing the cold temperatures necessary for astrochemical experiments to be reached. Surrounding the cold, uniform flow (known as the core), boundary layers with varying temperatures and pressures are also formed. A key advantage of the CRESU method is that it does not require collisions with a wall to cool the molecules and is functionally wall-less.[19] This allows for molecules with low vapor pressures to be studied at these cold temperatures.

The temperature of a CRESU flow, T_{flow}, can be calculated with

$$T_{flow} = T_0 \left(1 + \frac{\gamma - 1}{2} M^2\right)^{-1} \qquad \text{(Equation 2.9)}$$

where T_0 is the temperature of the reservoir, γ is the ratio of the specific heat capacities C_p/C_v of the buffer gas (typically N_2, He or Ar), and M is the Mach number of the expansion. This value is experimentally measured to characterize the nozzle before use in chemical kinetics measurements, as described below.

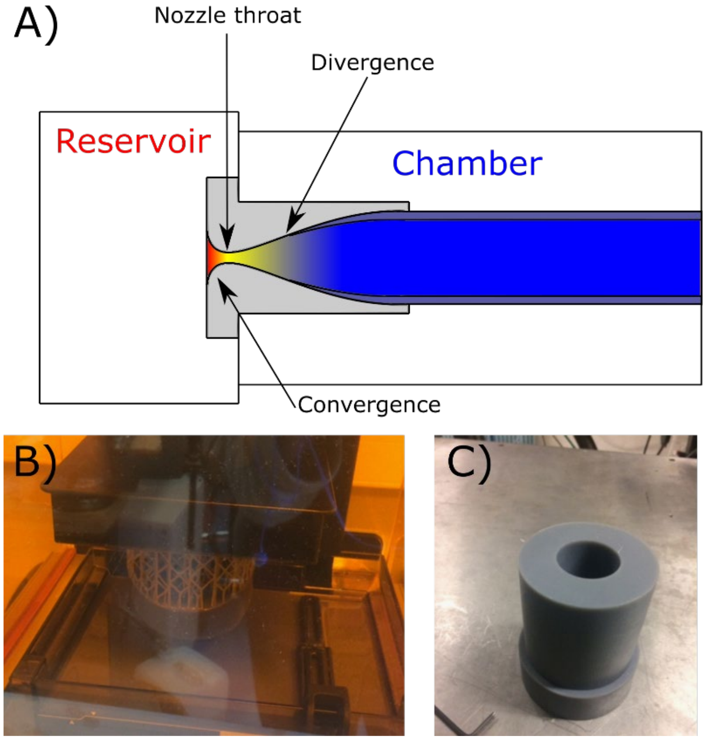

Figure 2.6: (A): A diagram of a Laval nozzle, showing gas being compressed in the convergent portion of the nozzle, before reaching the minimum diameter at the throat and being expanded through the divergent portion of the nozzle to produce a cold uniform flow. (B): A Laval nozzle being 3D printed. (C): Example of a Laval nozzle.

The temperature and density of the cold uniform flow is a function of the nozzle's geometry, and they must be carefully designed to create suitable nozzles. The advent of high precision 3D printers has allowed for faster manufacturing of Laval nozzles, as can be seen in Figure 2.6B and 2.6C. Due to imperfections in the manufacturing, however, all nozzles must be tested prior to use in experiments to characterize the flow and determine the necessary conditions for achieving a stable flow.

The method for testing the nozzle uses a Pitot probe to conduct impact pressure measurements. This probe is a hollow tube inserted into the flow; impact of the supersonic flow with the Pitot probe creates a shockwave. The impact pressure from this shockwave is measured by a pressure sensor attached to the Pitot tube. The pressure measured by the Pitot can then be related to the reservoir pressure with

$$P_i = P_r \left(\frac{(\gamma+1)M^2}{(\gamma-1)M^2+2}\right)^{\frac{\gamma}{\gamma-1}} \left(\frac{\gamma+1}{2\gamma M^2-\gamma+1}\right)^{\frac{1}{\gamma-1}} \qquad \text{(Equation 2.10)}$$

Which allows for the Mach number M to be determined. From that, the temperature can then be determined using Equation 2.9. By varying the position of the Pitot tube throughout the supersonic flow, the width and length of the uniform core can be determined. An example of Pitot measurements can be seen in Figure 2.7.

The typical densities of these uniform supersonic flows are 10^{16} – 10^{17} cm^{-3}.[19] Concentrations of the reactants and precursors must be kept under < 1% of the total flow rate to not disturb the uniformity of the flow. At concentrations higher than this, the uniformity of the flow is destroyed, making it unable to be used in spectroscopy and kinetics experiments. This imposes an upper limit on the rate constants that can be measured with CRESU to roughly ≥ 10^{-12} cm^3 s^{-1}.[19] However, if the reactant is also the buffer gas, then faster rates can be measured. This was done in Tizniti et al.,[22] who measured the rate constant of the F + H_2 reaction down to 11 K, where its rate is 2.48 × 10^{-13} cm^3 s^{-1}, by using a buffer gas of pure H_2 at the lowest temperatures.

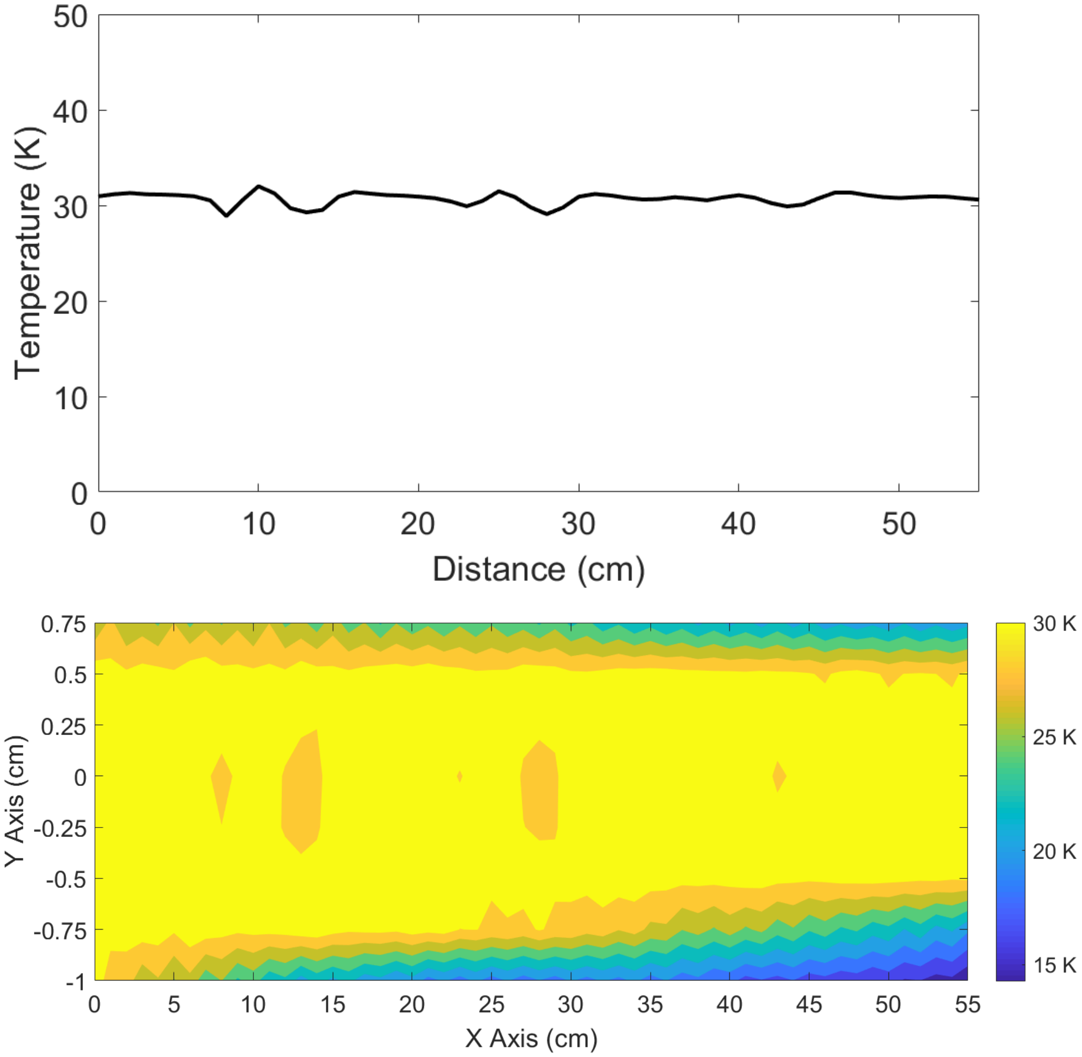

Figure 2.7: One-dimensional (top), along the y = 0 cm position, and two-dimensional (bottom) Pitot probe impact measurements of a 30 K N_2 Laval nozzle. Note that outside of the core, the flow is not isentropic with the reservoir and thus the temperature is not accurately calculated with Equations 2.9 and 2.10.

The gas flows used in CRESU experiments can be continuous or pulsed; pulsed CRESU instruments can be pulsed between the gas inlet and the reservoir, or between the reservoir and the chamber. Continuous CRESU flows require extremely powerful pumps in order to pump the gas at the necessary supersonic speeds in the chamber. Pulsed CRESU has historically pulsed between the gas inlet and the reservoir, which is unable to reach as low temperatures as continuous flows due to a smaller pressure differential between the reservoir and chamber. In recent years, a new method of pulsed CRESU, which uses a rapidly rotating aerodynamic chopper between the reservoir and the chamber, has been developed and allows pulsed CRESU to reach lower temperatures, but is technically demanding.[23]

In the experiments presented in this thesis, CRESU flows are used in conjunction with PLP-LIF in order to measure bimolecular rate constants down to 15 K in experiments done in collaboration with the University of Rennes 1. Figure 2.8 shows a schematic of the instrument used in this work. The LIF excitation beam passes into the CRESU flow through the nozzle. The LIF emission is then detected by a photomultiplier tube (PMT) placed above the supersonic flow, with an appropriate filter to exclude other wavelengths. To initiate the radical chemistry, an excimer laser fires through the CRESU flow; the timing between the excimer and the Nd:YAG lasers is controlled by a delay generator.

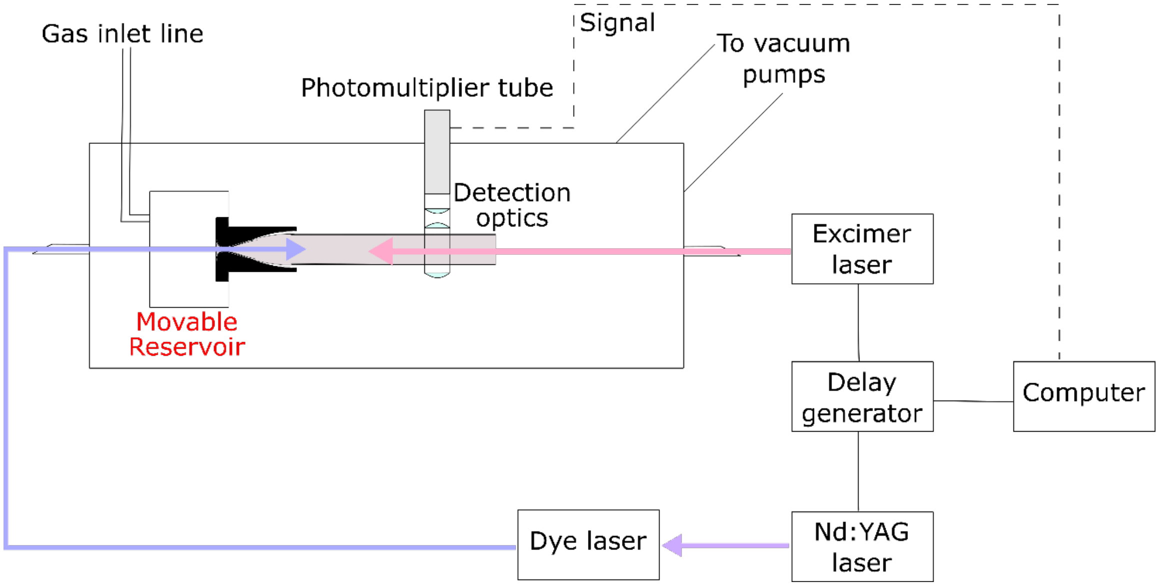

Figure 2.8: The CRESU PLP-LIF instrument used to measure bimolecular reaction rate constants in this work.

2.3 – References

1. Anderson, D. Z.; Frisch, J. C.; Masser, C. S., Mirror Reflectometer Based on Optical Cavity Decay Time. *Appl Optics* **1984**, *23*, 1238-1245.

2. O'Keefe, A.; Deacon, D. A. G., Cavity Ring-Down Optical Spectrometer for Absorption-Measurements Using Pulsed Laser Sources. *Rev Sci Instrum* **1988**, *59*, 2544-2551.

3. Busch, K. W.; Busch, M. A., *Cavity-Ringdown Spectroscopy : An Ultratrace-Absorption Measurement Technique*; American Chemical Society ; Distributed by Oxford University Press: Washington, DC New York, 1999, p xii, 269 p.

4. Scherer, J. J.; Paul, J. B.; O'Keefe, A.; Saykally, R. J., Cavity Ringdown Laser Absorption Spectroscopy: History, Development, and Application to Pulsed Molecular Beams. *Chem Rev* **1997**, *97*, 25-51.

5. Yu, T.; Lin, M. C., Kinetics of Phenyl Radical Reactions Studied by the Cavity-Ring-Down Method. *J Am Chem Soc* **1993**, *115*, 4371-4372.

6. Brown, S. S.; Ravishankara, A. R.; Stark, H., Simultaneous Kinetics and Ring-Down: Rate Coefficients from Single Cavity Loss Temporal Profiles. *J Phys Chem A* **2000**, *104*, 7044-7052.

7. Richardson, S. J.; Miles, N. L.; Davis, K. J.; Crosson, E. R.; Rella, C. W.; Andrews, A. E., Field Testing of Cavity Ring-Down Spectroscopy Analyzers Measuring Carbon Dioxide and Water Vapor. *J Atmos Ocean Tech* **2012**, *29*, 397-406.

8. Bitter, M.; Ball, S. M.; Povey, I. M.; Jones, R. L., A Broadband Cavity Ringdown Spectrometer for in-situ Measurements of Atmospheric Trace Gases. *Atmos Chem Phys* **2005**, *5*, 2547-2560.

9. Sun, M. X.; Jiang, C. Y.; Gong, Z. Y.; Zhao, X. M.; Chen, Z. Y.; Wang, Z. N.; Kang, M. L.; Li, Y. X.; Wang, C. J., A Fully Integrated Standalone Portable Cavity Ringdown Breath Acetone Analyzer. *Rev Sci Instrum* **2015**, *86*.

10. Reid, S. A.; Tang, Y., Generation of Tunable, Narrow-Band Mid-Infrared Radiation through a 532 nm Pumped KTP Optical Parametric Amplifier. *Appl Optics* **1996**, *35*, 1473-1477.

11. Tango, W. J.; Link, J. K.; Zare, R. N., Spectroscopy of K_2 Using Laser-Induced Fluorescence. *J Chem Phys* **1968**, *49*, 4264-&.

12. Heard, D. E.; Pilling, M. J., Measurement of OH and HO_2 in the Troposphere. *Chem Rev* **2003**, *103*, 5163-5198.

13. Jacobsen, R. T.; Stewart, R. B.; Jahangiri, M., Thermodynamic Properties of Nitrogen from the Freezing Line to 2000 K at Pressures to 1000 MPa. *J Phys Chem Ref Data* **1986**, *15*, 735-909.

14. Smalley, R. E.; Wharton, L.; Levy, D. H., Molecular Optical Spectroscopy with Supersonic Beams and Jets. *Accounts Chem Res* **1977**, *10*, 139-145.

15. Hutzler, N. R.; Lu, H. I.; Doyle, J. M., The Buffer Gas Beam: An Intense, Cold, and Slow Source for Atoms and Molecules. *Chem Rev* **2012**, *112*, 4803-4827.

16. Hu, M. G.; Liu, Y.; Grimes, D. D.; Lin, Y. W.; Gheorghe, A. H.; Vexiau, R.; Bouloufa-Maafa, N.; Dulieu, O.; Rosenband, T.; Ni, K. K., Direct Observation of Bimolecular Reactions of Ultracold KRb Molecules. *Science* **2019**, *366*, 1111-+.

17. Rowe, B. R.; Dupeyrat, G.; Marquette, J. B.; Gaucherel, P., Study of the Reactions $N_2^+ + 2\,N_2 \rightarrow N_4^+ + N_2$ and $O_2^+ + 2\,O_2 \rightarrow O_4^+ + O_2$ from 20 to 160 K by the CRESU Technique. *J Chem Phys* **1984**, *80*, 4915-4921.

18. Sims, I. R.; Queffelec, J. L.; Defrance, A.; Rebrionrowe, C.; Travers, D.; Bocherel, P.; Rowe, B. R.; Smith, I. W. M., Ultralow Temperature Kinetics of Neutral-Neutral Reactions - the Technique and Results for the Reactions $CN+O_2$ Down to 13 K and $CN+NH_3$ Down to 25 K. *J Chem Phys* **1994**, *100*, 4229-4241.

19. Fournier, M.; Le Picard, S. D.; Sims, I. R., Chapter 1: Low-Temperature Chemistry in Uniform Supersonic Flows. In *Cold Chemistry: Molecular Scattering and Reactivity near Absolute Zero*, The Royal Society of Chemistry: 2018; pp 1-45.

20. Cooke, I. R.; Sims, I. R., Experimental Studies of Gas-Phase Reactivity in Relation to Complex Organic Molecules in Star-Forming Regions. *ACS Earth Space Chem* **2019**, *3*, 1109-1134.

21. Lara, M.; Berteloite, C.; Paniagua, M.; Dayou, F.; Picard, S. D.; Launay, J. M., Experimental and Theoretical Study of the Collisional Quenching of $S(^1D)$ by Ar. *Phys Chem Chem Phys* **2017**, *19*, 28555-28571.

22. Tizniti, M.; Le Picard, S. D.; Lique, F.; Berteloite, C.; Canosa, A.; Alexander, M. H.; Sims, I. R., The Rate of the $F + H_2$ Reaction at Very Low Temperatures. *Nat Chem* **2014**, *6*, 141-145.

23. Jimenez, E.; Ballesteros, B.; Canosa, A.; Townsend, T. M.; Maigler, F. J.; Napal, V.; Rowe, B. R.; Albaladejo, J., Development of a Pulsed Uniform Supersonic Gas Expansion System Based on an Aerodynamic Chopper for Gas Phase Reaction Kinetic Studies at Ultra-Low Temperatures. *Rev Sci Instrum* **2015**, *86*.

Chapter 3 – Temperature- and Pressure-Dependent Branching Ratios of the OH + NO_2 Reaction Using Cavity Ringdown Spectroscopy

3.1 – Abstract

The reaction between OH and NO_2 has long been known to play an important role in ozone production over urban areas, due to its ability to sequester NO_x as nitric acid ($HONO_2$). However, a minor channel leading to peroxynitrous acid (HOONO) formation can also occur. Due to the instability of this molecule, it is believed to quickly redissociate back to OH and NO_2, thereby decreasing this reaction's efficiency as a sink for nitrogen oxides (NO_x). The branching ratio between these channels, denoted α = [HOONO]/ [$HONO_2$], varies as a function of temperature and pressure, but experimental measurements of these values are limited. Here, we present measurements of the temperature- and pressure-dependence of the branching ratio of this reaction over a range of temperatures (255 – 333 K) and pressures (50 – 700 torr). Reactions were initiated by pulsed laser photolysis in a flow reactor, and HOONO and $HONO_2$ formed in real time were detected by mid-infrared cavity ringdown spectroscopy. By combining our results with the latest recommendations of the total OH + NO_2 rate constant from the JPL data evaluation, we provide individual rate constants for the formation of HOONO and of $HONO_2$.

3.2 – Introduction

Throughout the troposphere and stratosphere, the coupling of the HO_x (HO_x = OH and HO_2) and NO_x (NO_x = NO and NO_2) families plays an important role in a region's air quality. OH radicals are the primary source that oxidize stable, long-lived molecules in the atmosphere, while NO_2 radicals lead to the formation of photochemical smog in urban environments.[1] The most important coupling between the HO_x and NO_x families is the termolecular radical-terminating reaction between OH and NO_2.

$OH + NO_2 + M \rightarrow HONO_2 + M$ (R3.1a)

$OH + NO_2 + M \rightarrow HOONO + M$ (R3.1b)

The nitric acid, $HONO_2$, formed from R3.1a is long-lived in the atmosphere, thus serving as a sink for both HO_x and NO_x. This reaction plays an important role in atmospheric modelling by sequestering radical concentrations; a sensitivity analysis studying the impact of over 900 model inputs on the modelled ozone concentration in urban environments found that the total rate constant $k_{3.1}$ ($k_{3.1} = k_{3.1a} + k_{3.1b}$) was the most important rate constant, and second-most important parameter overall.[2] Under urban conditions (low VOCs, high NO_x), R3.1a is responsible for a paradoxical decrease in ozone production with increasing NO_x, by removing OH and inhibiting OH-initiated oxidation of VOCs.

The alternate pathway, shown in R3.1b, leads to the formation of peroxynitrous acid, HOONO, was first proposed in 1983 by Robertshaw and Smith.[3] HOONO was not observed until 2002, when the HOONO arising from R3.1b was detected through vibrational overtone photodissociation spectroscopy.[4] Since then, it has been the subject of several experimental studies[4-8] in order to better understand the molecule. HOONO quickly decomposes to regenerate OH and NO_2 at room temperature and consequently reduces efficiency of R3.1 as a sink.[9] The potential energy surface of the reaction can be seen in Figure 3.1. These results indicate that there are two conformers of HOONO that can be formed, known as *cis-cis* and *trans-perp*, with the *cis-cis* being the lower energy of the two, as seen in Figure 3.1. Under atmospheric conditions, the *trans-perp* HOONO isomerizes to *cis-cis*, which is stabilized by an internal hydrogen bond between the hydrogen and terminal oxygen.[7]

While there have been a number of experimental studies measuring $k_{3.1}$ at a wide range of temperatures and pressures by monitoring the decay of OH in an excess of NO_2, as summarized and evaluated by JPL[9] and IUPAC,[10] experimental measurements of the branching ratio of the products, $\alpha = k_{3.1b}/k_{3.1a}$ (= [HOONO]/[$HONO_2$]), are scarce. Furthermore, α changes as a function of both temperature and pressure, making it necessary to measure over a wide range of conditions. The only two direct measurements of the branching ratio are from Mollner et al.,[11] who measured it between 50 and 750 torr at room temperature, and Bean et al.,[6] who studied it at 20 torr from 270 to 360 K; both studies used pulsed laser photolysis in conjunction with mid-IR spectroscopy to measure the ν_1 bands of HOONO and $HONO_2$. Hippler et al.[12-13] extracted rate constants for the two channels from their high pressure measurements and fall-off curve analysis of the OH decay. Troe[14] re-analyzed the data of Mollner et al. and Hippler et al. in order to separately determine the rate constants $k_{3.1a}$ and $k_{3.1b}$.

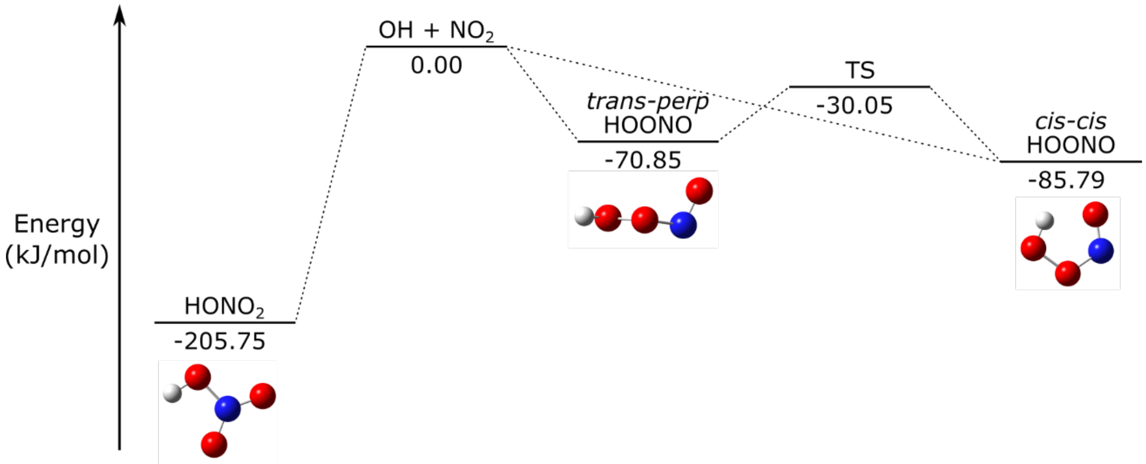

Figure 3.1: Simplified potential energy surface of the OH + NO_2 reaction in kJ/mol; molecular geometries are from the Active Thermochemical Tables[15] and the transition state energy is the experimental value of Fry et al.[7]

Current recommendations for the branching ratio (and thus, $k_{3.1a}$ and $k_{3.1b}$) from the JPL data evaluation are based on the RRKM (Rice–Ramsperger–Kassel–Marcus) master equation calculations performed by Golden et al.,[16] while IUPAC's evaluation is based on the results of Mollner et al. and Troe. The uncertainties present in the determined parameters are large: JPL recommends an uncertainty factor 1.3 for $k_{3.1a}$ and 1.5 for $k_{3.1b}$ at 298 K, with increasing uncertainty at other temperatures. IUPAC recommends uncertainty factors of 1.12 and 2.0 for the low and high-pressure limits of $k_{3.1a}$, respectively, and 1.26 and 2.0 for the low and high-pressure limits of $k_{3.1b}$ at 300 K. As the temperature moves away from 298 K, these uncertainties will further increase. These large uncertainties propagate into the atmospheric models that are reliant on these evaluations. A recent modeling analysis studied the impact of these uncertainties on four key metrics from the GEOS-Chem chemical transport model: annual tropospheric ozone burden, surface ozone concentration, tropospheric OH concentration and tropospheric methane lifetime.[17] Their results found that R3.1a was the single largest source of uncertainty among inorganic rate constants and photolysis rates across all metrics, and recommend focusing efforts on improving this rate constant among others to improve our knowledge of atmospheric composition.

Due to both the high uncertainty of these rate constants in current recommendations and the importance of this reaction for atmospheric modelling, we have extended the work of Mollner et al. and Bean et al. In this study, we have measured the pressure-dependent branching ratio α over a wide range of temperatures, from 255 to 333 K, and pressures 50 to 700 torr. By combining these measurements with previous measurements of $k_{3.1}$, we have also determined $k_{3.1a}$ and $k_{3.1b}$.

3.3 – Experimental Methods

These experiments used a pulsed laser photolysis-cavity ringdown spectroscopy (PLP-CRDS) apparatus, which has been described previously in the literature[11, 18-19] and in Chapter 2. Briefly, reactions are initiated in a temperature-controlled flow cell, described in Chapter 2, by pulsed UV light at 248 nm to generate OH in the presence of NO_2. The v_1 OH-stretch bands of the primary $HONO_2$ and HOONO products were detected at a fixed delay time after the completion of the reaction, by pulsed mid-infrared cavity ringdown spectroscopy. Concentrations were determined by integrating the absorption bands, using computed absorption band intensities.

The 532 nm light pulses from a frequency-doubled Nd:YAG laser, operated at 10 Hz, passed through a 70/30 beamsplitter, where 30% of the 532 nm light pumped a tuneable dye laser containing DCM dye. The output of the dye laser was recombined with the remaining (70% transmitted) 532 nm light and sent into nonlinear KDP crystals, which produced mid-IR light as the idler by difference frequency generation. The mid-IR light was filtered to remove pump and signal radiation and then coupled into an optical cavity formed by two highly reflective mirrors (R > 0.9998, CRD Optics) enclosing the reaction volume in the flow cell. The output was detected by a liquid nitrogen cooled InSb detector. This instrument operates in the 3200 – 3750 cm^{-1} range, limited by the mirror reflectivity, which allowed us to detect the v_1 OH stretches of HOONO and $HONO_2$, as has been previously observed with this instrument in our group.[6, 11] UV pulses at 248 nm were generated by an excimer laser (Lambda Physik 210i) and focused into the reaction cell perpendicularly to the IR cavity axis to generate OH radicals. Experiments were performed at 10 Hz. The total gas flow rate was sufficient to ensure complete exchange of gas in the flow reactor between pulses.

Sixteen ringdowns decay traces were recorded and averaged at each frequency; each were taken with and without the excimer firing at each point in our spectrum (referred to subsequently as the 'excimer-on' and 'excimer-off' spectra, respectively). A mirror curve, taken under vacuum at each temperature studied, was recorded daily, and fit to determine the reflectivity of the mirrors as a function of frequency.

3.3.1 – Radical Chemistry

OH was generated via the photolysis of O_3 at 248 nm, followed by subsequent reaction with H_2:

$$O_3 + hv \rightarrow O(^1D) + O_2 \qquad \text{(R3.2)}$$

$$O(^1D) + H_2 \rightarrow OH + H \qquad \text{(R3.3)}$$

NO_2 was added in excess, such that the OH + NO_2 reaction is under pseudo-first order conditions; typical gas concentrations were $[O_3] = 1 - 15 \times 10^{15}$ cm^{-3}, $[NO_2] = 1 - 10 \times 10^{15}$ cm^{-3}, and $[H_2] = 5 - 25 \times 10^{17}$ cm^{-3}, with the balance N_2. H_2 concentrations were increased at higher pressures to minimize quenching of the $O(^1D)$ by N_2. Ozone was generated from flowing O_2 through a corona discharge ozonizer. To minimize secondary chemistry, the ozone was purified to remove O_2, by condensing the ozone on silica gel in a metal trap cooled by a dry ice/acetone bath. The O_2 was removed by vacuum. During the experiment, the ozone was introduced into the flow cell by flowing N_2 through the trapped ozone. Before mixing with other gases, the O_3 concentration was measured by flowing the O_3/N_2 mixture through a 1 m long flow cell. UV light at 307.6 nm ($\sigma_{307.6} = 1.4 \times 10^{-19}$ cm^2)[9] from a Zn lamp was passed through the cell and was detected with a monochromator and photomultiplier tube. The ozone concentration was recorded at the beginning and end of each scan to observe any fluctuations in O_3 concentration; typical O_3 concentrations were stable to within 15%. Measurements with larger fluctuations in [O_3] were excluded from fits.

The hydrogen atoms formed as a by-product of R3.3 can undergo two fates: reaction with NO_2 or with O_3.

$H + NO_2 \rightarrow OH + NO$ (R3.4)

$H + O_3 \rightarrow OH + O_2$ (R3.5)

These additional OH radicals from both channels undergo further reaction with NO_2. The presence of NO and O_2 from this chemistry may lead to side chemistry that interferes with our spectroscopic measurements, as the reactions with NO lead to the production of HONO from

$OH + NO + M \rightarrow HONO + M$ (R3.6)

While O_2 could lead to HO_2 formation

$H + O_2 + M \rightarrow HO_2 + M$ (R3.7)

Spectral features arising from small concentrations of HONO were observed and therefore were included in our spectral fitting program. HO_2 and its likely end product, HO_2NO_2, were not observed and were therefore omitted.

OH produced from R3.3 is known to be vibrationally excited, resulting in up to OH ($v = 4$).[20] Mollner et al., who also used R3.3 to produce OH, performed several experiments to verify whether this affected the measured branching ratio, by using an alternate source of OH, $O(^1D) + CH_4$, which produces a much smaller quantity of excited OH radicals.[21] They did not find any change in their measured values from these experiments, suggesting that the presence of hot OH does not affect the branching ratios. While vibrational relaxation rates for OH ($v = 1 – 4$) with the gases present in our system have not been measured, Smith and Williams previously measured the rate constant for OH ($v = 1$) relaxation by NO_2 at room temperature to be 4.8×10^{-11} cm^3 s^{-1}.[22] Assuming that higher vibrational states of OH relax at the same rate, a kinetic model indicates that all OH is vibrationally cooled within 10 – 100 μs under our NO_2 concentrations. This is likely an overestimate of the lifetime of vibrationally-excited OH within our system, as higher vibrational levels are likely to have larger rate constants for vibrational relaxation. Together, these results suggest that influence of vibrationally-excited OH on our branching ratio measurements is negligible.

Spectra were measured 500 μs after photolysis. As can be seen in Figure 3.2, time-dependent measurements of HOONO and $HONO_2$ indicated that this reaction is complete in roughly 150 μs; the signal remains stable for up to 3 ms in our system before being vacuumed out, even at our highest temperatures of 333 K. The time-dependent measurements agree well with a simple model of the product appearance based on $k_{3.1}$, the experimental conditions and NO_2 concentration used in experiments (4.4×10^{15} cm^{-3}).

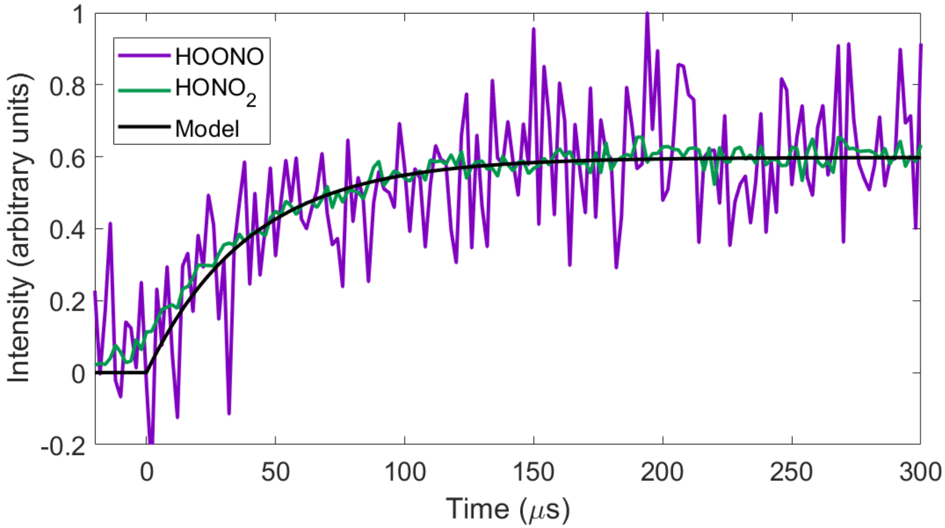

Figure 3.2: Time traces of HOONO at 3307 cm^{-1} (purple) and $HONO_2$ at 3520 cm^{-1} (green) at 333 K and 300 torr showing the formation of products; the excimer fires at 0 μs to initiate radical chemistry. The modelled appearance of products, based on the experimental conditions and NO_2 concentrations used is shown in black.

3.3.2 – Spectroscopy and Spectral Fitting

A typical experimental spectrum, measured from 3250 – 3630 cm^{-1} with a step size of 2 cm^{-1}, is shown in Figure 3.3. This step size was used because it provided sufficient resolution to clearly identify the key spectral features, while allowing us to minimize uncertainties from fluctuations in ozone concentration during a scan. Typical scan times were 25 minutes to record a full spectrum. The ν_1 band of $HONO_2$, centered at 3550 cm^{-1}, was the dominant feature, while its $2\nu_2$ band can be seen in the inset at 3400 cm^{-1}. The *cis-cis* conformer of HOONO was observed at 3306 cm^{-1}. Weak features of both c*is*-HONO and *trans*-HONO arising from secondary chemistry could be also be observed in some spectra, most notably the Q-branch of the ν_1 OH stretch of *trans*-HONO at 3590 cm^{-1}.

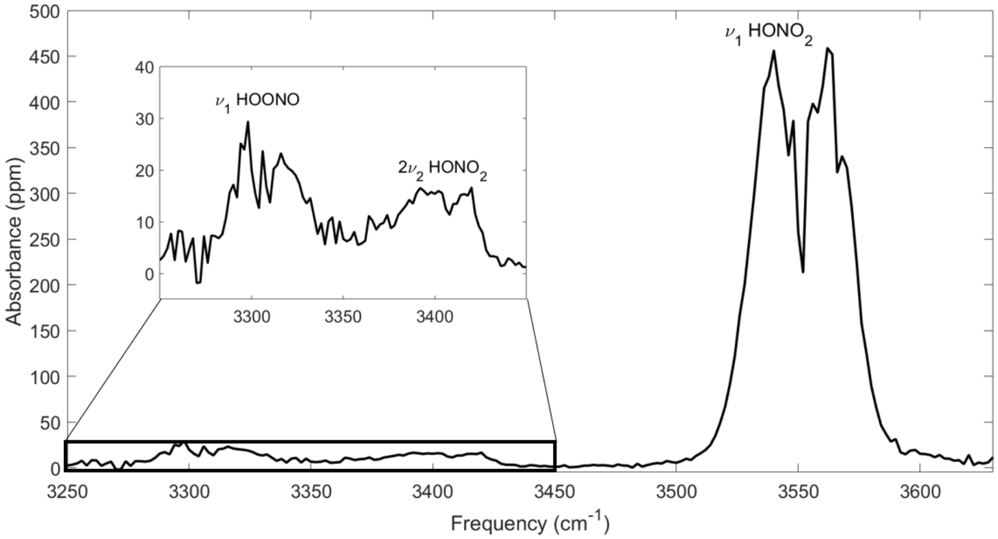

Figure 3.3: Experimental spectrum taken at 283 K and 500 torr, 500 μs after photolysis, showing the ν_1 bands of HOONO and HONO$_2$ and the $2\nu_2$ band of HONO$_2$. This spectrum is obtained by subtracting the excimer-off spectrum from the corresponding excimer-on spectrum.

Each spectrum was fit using a nonlinear least squares fit in Matlab to a sum of reference spectra. The reference spectra were either from the PNNL spectral database[23] or, for HOONO, measured in our lab.[6] The PNNL spectral database shows that HONO$_2$, N$_2$O$_4$ and HONO spectra do not change with temperature. Any change in the spectrum of HOONO will be accounted for by $f_{Boltz}(T)$, as discussed below in Section 3.3.3. The total absorbances of HOONO and HONO$_2$ (A_{HOONO} and A_{HONO_2} respectively) was obtained by integrating the spectral features from our fits, as discussed below. The branching ratio α(T, p) was obtained:

$$\alpha = \frac{\int A_{HOONO}}{\int A_{HONO_2}} \frac{\sigma_{HONO_2}}{\sigma_{HOONO}} f_{Boltz}(T) \qquad \text{(Equation 4.1)}$$

The ratio of the cross sections ($\sigma_{HONO_2}/\sigma_{HOONO}$) has previously been calculated by Mollner et al.[11] using CCSD(T)/ANO to be 2.71, while $f_{Boltz}(T)$ is a temperature-dependent correction factor for the impact of the stretch-torsion coupling of HOONO on our measurements of A_{HOONO}, as discussed in the following section.

3.3.3 – HOONO Spectroscopy

As discussed in Section 3.1, there are two stable conformers of HOONO, *trans-perp* HOONO and *cis-cis* HOONO; only the latter of which we observe in our spectrum due to the rapid isomerization of *trans-perp* HOONO.[7] The presence of the internal hydrogen bond between the terminal oxygen and the hydrogen in *cis-cis* HOONO redshifts its ν_1 OH stretch; previous mid-IR measurements found that this band is centered at 3306 cm^{-1}.[6] Based on these measurements, we have determined A_{HOONO} by fitting our experimental measurements of the *cis-cis* HOONO stretch region (3264 – 3352 cm^{-1}) to a room-temperature reference spectrum from Mollner et al.[11]

However, stretch-torsion coupling between the OH stretch and two low-lying torsional states must be corrected for in our analysis. These torsional modes, belonging to the ν_9 HOON (n = 1 mode centered at 312 cm^{-1}) and ν_8 OONO (n = 1 mode centered at 484 cm^{-1}) modes,[24] have significant populations at room temperature. These torsionally-excited states change the position of the HOONO ν_1 stretch; extensive calculations have been done by McCoy et al.[24] on this effect for up to n = 8 of ν_9 and n = 2 of ν_8, as well as combinations of these modes. These calculations indicate that the ν_1 band can shift out of our integration range in some of these torsionally excited states. In order to account for how this affects the determination of A_{HOONO}, we incorporated a correction factor, $f_{Boltz}(T)$, based on the Boltzmann distribution of torsionally excited states and whether the center frequency of the ν_1 state is inside the A_{HOONO} integration region. Further details of these calculations and $f_{Boltz}(T)$ can be found in Mollner et al.[11] and McCoy et al.[24]

A_{HOONO} was fit by subtracting the excimer-off spectrum from the excimer-on spectrum, which removes any background absorbance from non-photolytically generated molecules. Spectra were fit between 3250 and 3440 cm^{-1} to avoid ν_1 stretch of $HONO_2$, which is the most intense peak in our spectra. The intensities of the ν_1 stretch of HOONO and $2\nu_2$ stretch of $HONO_2$ were fit, along with background absorbance of HONO and a sloped baseline. The intensity of the ν_1 stretch of HOONO was subsequently integrated to determine A_{HOONO}.

3.3.4 – $HONO_2$ Spectroscopy

The ν_1 band of $HONO_2$ has been the subject of numerous studies. Chackerian et al. studied the integrated cross sections from 278 to 323 K and observed no change in the cross sections of this band.[25] Measurements taken at 255 and 333 K with our CRDS system also found no change in the spectral shape. Therefore, we assumed the shape of the ν_1 band of $HONO_2$ to be temperature-independent over the temperature range studied here. Spectra were fit to a reference from PNNL,[23] which was integrated between 3476 and 3630 cm^{-1} to determine A_{HONO_2}.

Our previous measurements of the ν_1 stretch of $HONO_2$ have found that a correction factor is necessary in order to accurately quantify [$HONO_2$].[11] This correction factor arises from an effect in cavity ringdown spectroscopy originally described by Yalin and Zare,[26] which occurs when the linewidth of the laser is larger than spectroscopic features being probed. This leads to multiexponential ringdowns that, when fit to a single exponential decay, provide a value that underestimates the true absorbance. This effect is dependent on the pressure of the system, and the intensity of the absorption features. As the most intense feature in our experimental spectrum, our quantification of [$HONO_2$] from its ν_1 stretch is impacted and must be corrected for to obtain accurate branching ratios. We applied this correction to the most intense parts of our spectrum, 3524 - 3576 cm^{-1}. The correction factor, previously used in Mollner et al. and checked with extensive measurements of $HONO_2$ at varying pressures and concentrations,[11] convolves a high resolution spectrum of the $HONO_2$ ν_1 stretch with pressure broadening parameters and a 1 cm^{-1} bandwidth laser pulse to simulate the experimental ringdown decay and convert to A_{HONO_2}.

The ν_1 stretch of $HONO_2$ was observed in our excimer-off spectra, indicating that some level of $HONO_2$ was present in our system before photolysis occurs, most likely due to heterogeneous chemistry occurring within the gas lines. While not as intense as the excimer-on $HONO_2$, in order to accurately determine A_{HONO_2}, we separately analyzed the excimer-on and excimer-off spectra. The absorbance due to the reflectivity of the mirrors is removed from these spectra. The excimer-off spectra are fit with the ν_1 and $2\nu_2$ peaks of $HONO_2$ as well as an overtone of N_2O_4. For the excimer-on spectra, the spectra of HOONO and HONO are also included in the fit. Both spectra also include a sloped baseline, or when necessary due to differences between our mirror curve and experimental spectrum, a quadratic baseline. The correction factor for multiexponential ringdowns is applied to the ν_1 band of $HONO_2$, as discussed in Section 3.3.4. The intensity of both the excimer-on and excimer-off spectra are subsequently integrated and the difference is taken as our value of A_{HONO_2}.

Our fitting routine found that the intensity of the Q-branch of the ν_1 band of $HONO_2$, located at 3552 cm^{-1} is not consistent throughout our data or with the intensity predicted by our fitting routine, likely due the sharpness of the feature and small calibration offsets in our frequency axis. This point is therefore excluded from our fit. We do not find any evidence of these frequency offsets affecting the rest of our experimental spectra.

3.4 – Results and Discussion

3.4.1 – Branching Ratio Measurements

Measurements were taken at nine temperatures between 255 and 333 K in roughly 10 K steps, with pressures varying from 50 to 700 torr at each temperature. For each temperature and pressure point, spectra were recorded multiple times (typically five). Each spectrum was fit with our reference spectra, as discussed above, to determine the final $HONO_2$ and HOONO concentrations, and the resulting branching ratio was determined from a weighted average.

As the reaction between OH and NO_2 is a termolecular reaction, we investigated whether the identity of the third body affected our results. H_2 was a present in excess in our experiments to form OH, and therefore we varied the ratio of H_2 in the total flow at 293 K and 100 torr to determine the effect of the bath gases on our branching ratio measurements. As can be seen in Figure 3.4, we do not observe a change in the branching ratio as a function of the bath gas ratio.

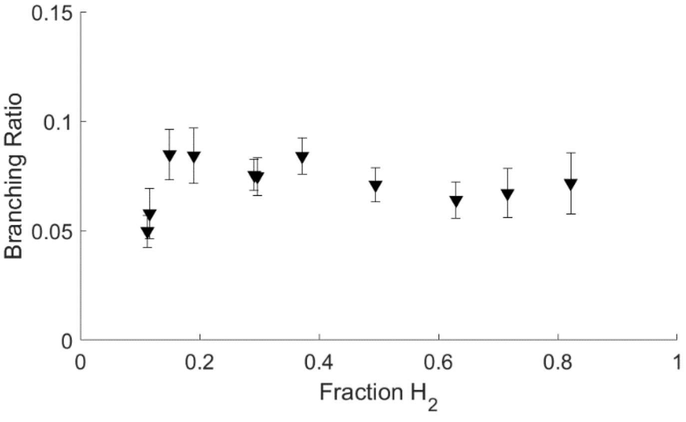

Figure 3.4. Experiments measuring the branching ratio as a function of H_2 fraction at 100 torr and 293 K, indicating that our measurements do not change as a function of H_2 concentration.

The weighted averages for the branching ratios can be seen in Table 3.1 A comparison between our measured branching ratios and those predicted by the JPL and IUPAC evaluations at 283 and 323 K can be seen in Figure 3.5. We find that at higher temperatures, the branching ratios from the data evaluations are close to our measurements, while at colder temperatures more relevant to the troposphere, the predictions overestimate α. This implies that either HOONO production is overestimated or $HONO_2$ production is underestimated in the current evaluations at these temperatures.

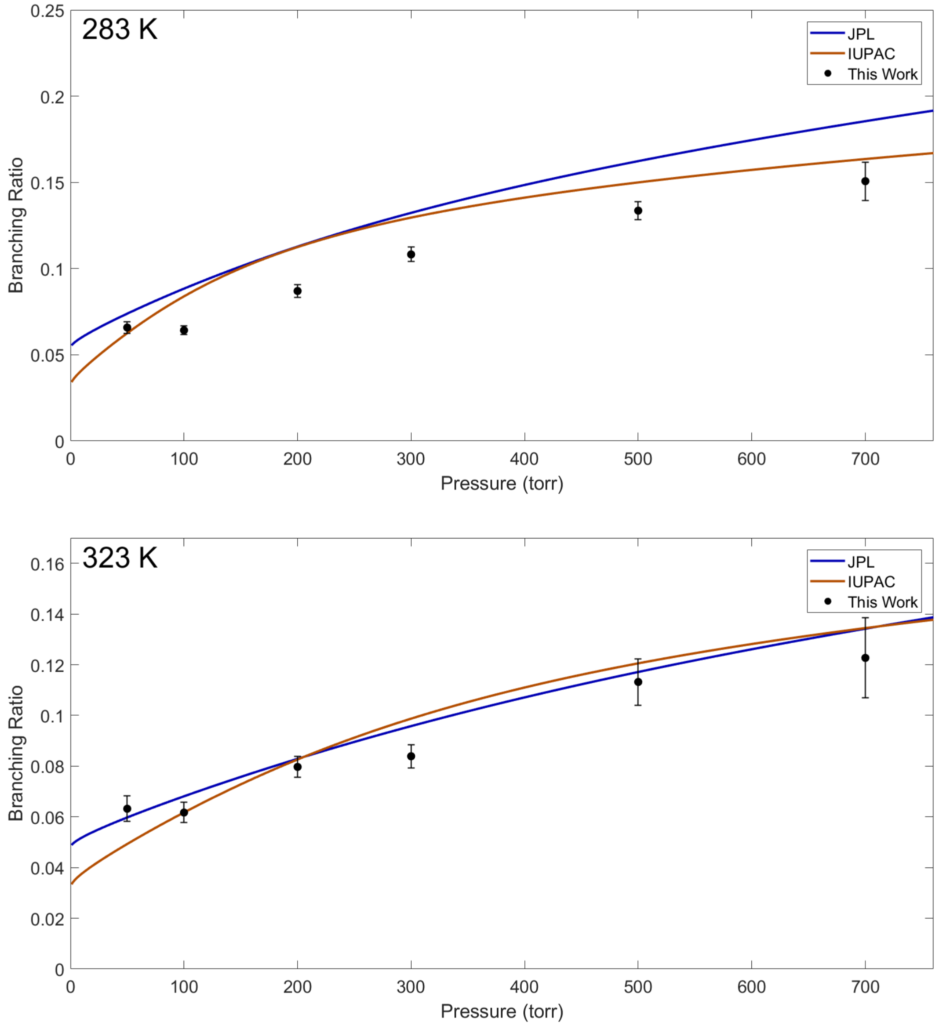

Figure 3.5: The branching ratios $k_{3.1b}/k_{3.1a}$ from the JPL and IUPAC data evaluations at 283 and 323 K, as compared to the experimental values measured in this work.

Table 3.1: The weighted averages of all branching ratios measured in this work.

Temp (K)	Pressure (torr)	Branching Ratio	Uncertainty	Number of Measurements
333	50	0.0749	0.0067	10
333	100	0.0625	0.0054	7
333	200	0.0819	0.0067	7
333	300	0.0831	0.0071	5
333	500	0.0958	0.0068	4
333	700	0.1214	0.0102	5
323	50	0.0632	0.0050	5
323	100	0.0617	0.0040	5
323	200	0.0797	0.0041	6
323	300	0.0839	0.0046	6
323	500	0.1132	0.0092	4
323	700	0.1227	0.0158	5
313	50	0.0459	0.0025	7
313	100	0.0549	0.0031	7
313	200	0.0687	0.0034	6
313	300	0.0847	0.0039	6
313	500	0.0858	0.0047	5
313	700	0.1164	0.0051	5
303	50	0.0564	0.0037	4
303	100	0.0657	0.0033	5
303	200	0.0834	0.0038	5
303	300	0.0882	0.0051	3
303	500	0.1060	0.0062	4
303	700	0.1593	0.0101	4
293	50	0.0437	0.0025	6
293	100	0.0651	0.0022	14
293	200	0.0811	0.0036	6
293	300	0.0901	0.0039	6
293	500	0.1269	0.0057	5
293	700	0.1448	0.0075	5
283	50	0.0658	0.0034	5
283	100	0.0642	0.0025	6
283	200	0.0870	0.0037	6
283	300	0.1082	0.0042	6
283	500	0.1336	0.0052	6
283	700	0.1507	0.0111	4
273	50	0.0607	0.0025	8
273	100	0.0751	0.0030	7
273	200	0.1066	0.0041	7
273	300	0.1163	0.0043	7

273	500	0.1363	0.0048	8
265	50	0.0677	0.0037	4
265	100	0.0846	0.0038	4
265	200	0.1069	0.0053	4
265	300	0.1211	0.0053	4
265	500	0.1616	0.0088	4
254	50	0.0735	0.0042	5
254	100	0.0744	0.0041	4
254	200	0.0929	0.0047	5
254	300	0.1212	0.0050	5
254	400	0.1461	0.0069	5

3.4.2 – Rate Constants for HOONO and $HONO_2$ Formation

Our measurements of α can be combined with measurements of the total rate constant k to determine individual rate constants for the formation of $HONO_2$ ($k_{3.1a}$) and HOONO ($k_{3.1b}$). Here, we use the $k_{3.1}$ measurements from the 2015 JPL data evaluation in order to determine these values. For termolecular reactions, we must fit data considering both the low-pressure and high-pressure limit, and thus the rate constants can be determined from

$$k(T) = \frac{k_0(T)M}{1+\frac{k_0(T)M}{k_\infty}} \times F_c^{\left(1+\log_{10}\left(\frac{k_0(T)M}{k_\infty(T)}\right)^2\right)^{-1}} \qquad \text{(Equation 3.2)}$$

$$k_0(T) = k_0^{300}\left(\frac{T}{300}\right)^{-n} \qquad \text{(Equation 3.3)}$$

$$k_\infty(T) = k_\infty^{300}\left(\frac{T}{300}\right)^{-m} \qquad \text{(Equation 3.4)}$$

where k_0^{300} is the low-pressure limit rate constant at 300 K in cm^6 s^{-1}, k_∞^{300} is the high-pressure limit rate constant at 300 K in cm^3 s^{-1}, T is the temperature in K, M is the total density in cm^{-3}, and n and m are the temperature dependence of the low- and high-pressure rate constants, respectively, and are dimensionless. F_c describes the falloff region between the low- and high-pressure limits; here we use the JPL data evaluation recommendation of

$F_c = 0.6$, though it is worth noting that the IUPAC data evaluation recommends $F_c = 0.41$ for this reaction based on the calculations by Troe.[10]

The values obtained for $k_{3.1a}$ and $k_{3.1b}$ can be seen in Tables 3.2 and 3.3, respectively, as compared to the current recommendations from JPL and IUPAC. As can be seen in Figure 3.6, $k_{3.1b}$ is in the low-pressure limit for all experimental conditions studied here and therefore, the data is fit to

$$k(T) = k_0^{300}\left(\frac{T}{300}\right)^{-n} M \qquad \text{(Equation 3.5)}$$

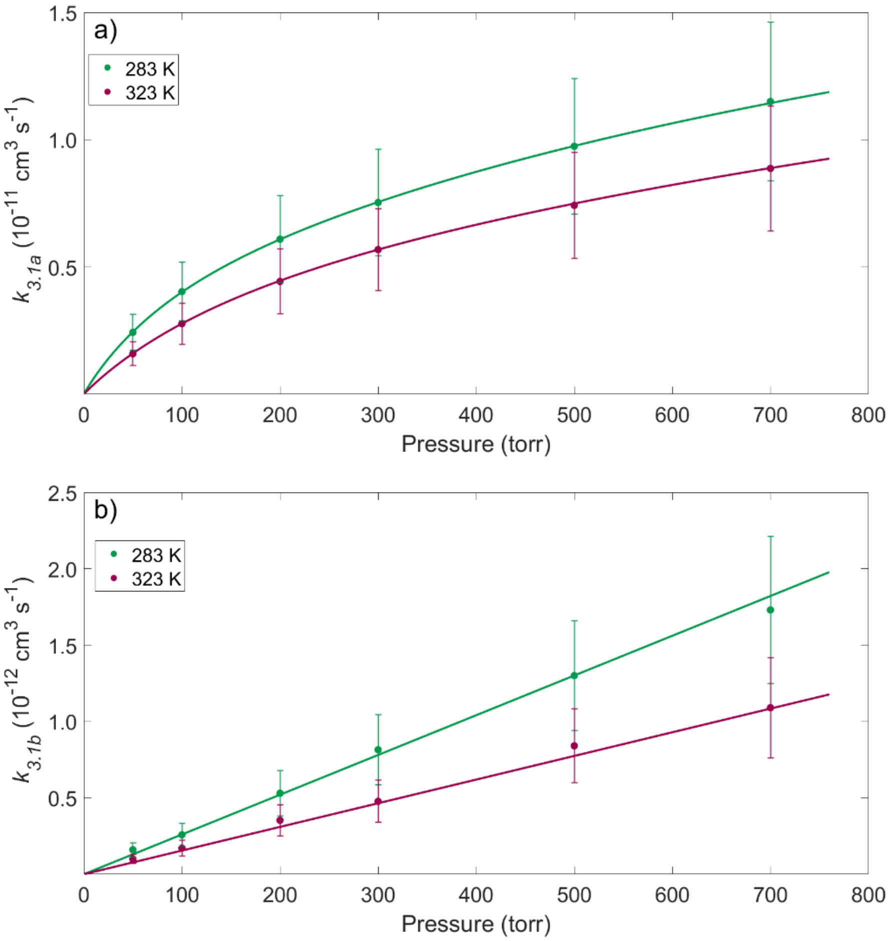

Figure 3.6: Rates of $k_{3.1a}$ (a) and $k_{3.1b}$ (b) at 283 and 323 K.

As Figure 3.7a and Table 3.2 demonstrate, the results from our determination of $k_{3.1a}$ is very close to the values from JPL. As we use the JPL value of $k_{3.1}$ and $F_c = 0.6$, this similarity is unsurprising. The IUPAC values for $k_{3.1a}$, on the other hand, are much larger than our value at low pressures, while there is still an offset at higher pressures. The difference between our $k_{3.1a}$ measurements and those from IUPAC are due to different values of $k_{3.1}$ between the JPL and IUPAC data evaluations. Resolution of this discrepancy in the total rate constant may bring all three of the measurements in line.

Table 3.2: Values of $k_{3.1a}$ determined in this work as compared to recommendations from the JPL and IUPAC data evaluations.

$k_{3.1a}$	k_0 (10^{-30} cm^6 s^{-1})	n	k_∞ (10^{-11} cm^3 s^{-1})	m	F_c
This work	1.80 ± 0.04	3.02 ± 0.023	2.90 ± 0.06	-0.04 ± 0.25	0.6[a]
JPL	1.8	3.0	2.8	0	0.6[a]
IUPAC	3.2	4.5	3.0	0	0.41

[a] Value fixed to 0.6

Table 3.3: Values of $k_{3.1b}$ determined in this work as compared to recommendations from the JPL and IUPAC data evaluations.

$k_{3.1b}$	k_0 (10^{-32} cm^6 s^{-1})	n	k_∞ (10^{-11} cm^3 s^{-1})	m	F_c
This work	6.43 ± 0.15	2.92 ± 0.25	-	-	0.6[a]
JPL	9.1	3.9	4.2	0.5	0.6[a]
IUPAC	10	4.5	3.5	0	0.41

[a] Value fixed to 0.6

Figure 3.7b shows that both the JPL and IUPAC values are much larger than our value of $k_{3.1b}$, as their k_0^{300} values are both almost 50% larger than our k_0^{300}. The IUPAC values do approach our measurements at high pressures, however. Both the JPL and IUPAC data evaluations suggest that $k_{3.1b}$ is in the fall-off region under our experimental conditions, which is not consistent with our results. Further experiments extending our pressure and temperature range are clearly necessary in order to determine the high-pressure limit rate constants for $k_{3.1b}$.

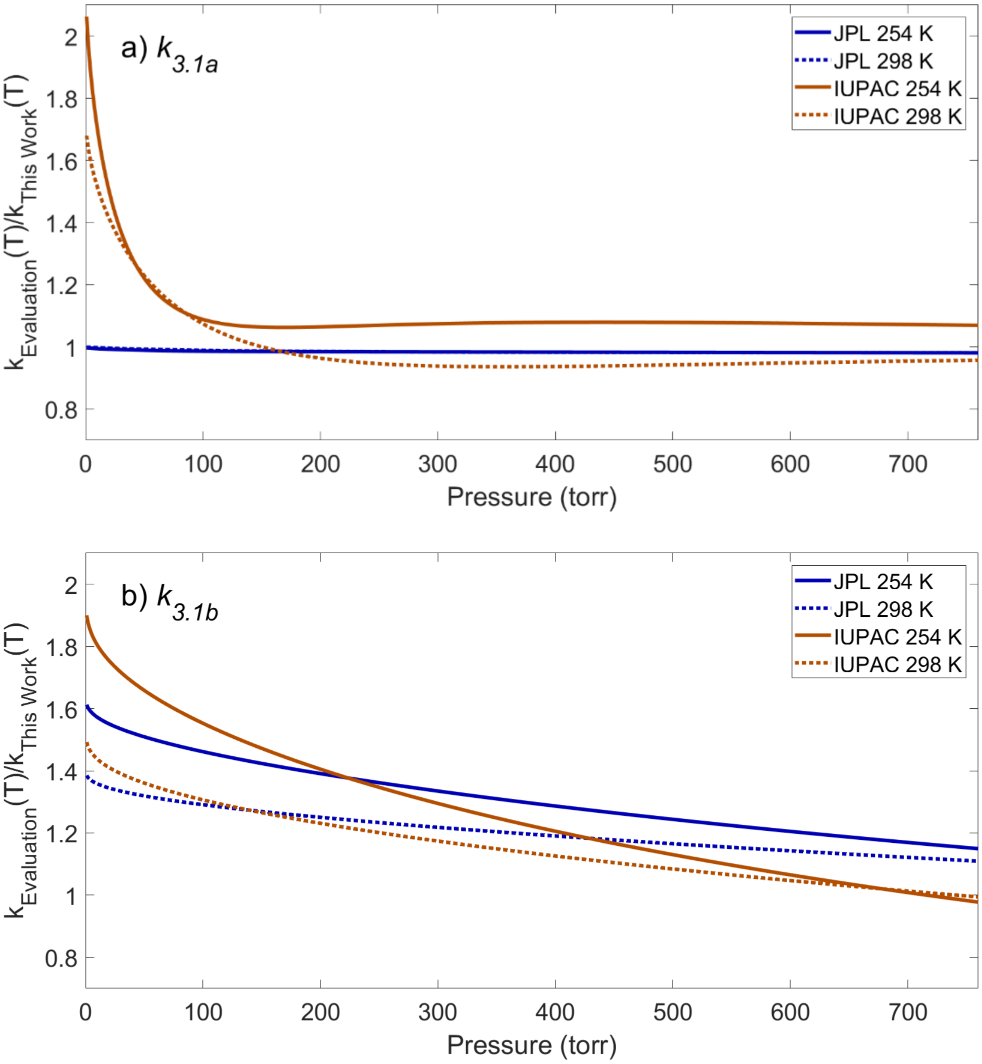

Figure 3.7: The ratio of the rate constants determined in this work for a) $k_{3.1a}$ and b) $k_{3.1b}$ to the values from the JPL and IUPAC data evaluations at 254 K and 298 K.

Despite the formation of HOONO representing a significant pathway for $k_{3.1}$ under atmospheric conditions, fate of HOONO is largely unknown. There are few experimental or theoretical studies on its gas-phase photolysis or on reactions that lead to its destruction, with the exception of the calculations done by Fry et al.[7] They calculated the oscillator strengths of the $2\nu_1$ band of *cis-cis* HOONO in conjunction with the actinic flux at 1.4 μm and suggest its lifetime is less than 45 daylight hours. They also perform thermal decomposition calculations, which suggest that the lifetime of HOONO ranges from seconds at the surface to 38 days at the tropopause, making it the dominant loss mechanism in the lower troposphere. Current widely used models, such as GEOS-Chem[27] 12.6.1 (http://www.geos-chem.org/, accessed November 2019), do not include $k_{3.1b}$ at all, presumably assuming its lifetime is negligible before dissociating to $OH + NO_2$. Additional measurements of these loss mechanisms would further our knowledge of the fate of HOONO in the atmosphere.

3.5 – Conclusion

We have directly measured the branching ratio of the $OH + NO_2$ reaction as a function of both temperature and pressure over the ranges of 255 – 333 K and 50 – 700 torr using mid-infrared CRDS in the OH stretch region (3250 – 3630 cm^{-1}) and a newly developed temperature-controlled flow cell. By combining our data with previous measurements of the total rate constant, we have determined rate constants for both the HOONO and $HONO_2$ channels of this reaction. Comparison to the current JPL and IUPAC recommendations of these rate constants reveals disagreement between our $k_{3.1b}$ values, as they overestimate the production of HOONO, while our $k_{3.1a}$ measurements largely agree with the recommended values.

The reaction between OH and NO_2, despite its importance in urban environments and being the subject of numerous studies, remains a large source of uncertainty in current atmospheric models. The inclusion of the data measured here into these recommendations may allow for refinement of these rates, particularly for $k_{3.1b}$. Further studies that extend the temperature and pressure range of these branching ratio measurements, and study the fate of HOONO in the atmosphere, are also necessary to better understand this reaction and its implications.

3.6 – References

1. Seinfeld, J. H.; Pandis, S. N., *Atmospheric Chemistry and Physics : From Air Pollution to Climate Change*, Third edition. ed.; John Wiley & Sons, Inc.: Hoboken, New Jersey, 2016, p xxvi, 1120 pages.

2. Martien, P. T.; Harley, R. A., Adjoint Sensitivity Analysis for a Three-Dimensional Photochemical Model: Application to Southern California. *Environ Sci Technol* **2006**, *40*, 4200-4210.

3. Robertshaw, J. S.; Smith, I. W. M., Kinetics of the OH + NO_2 + M Reaction at High Total Pressures. *J Phys Chem* **1982**, *86*, 785-790.

4. Nizkorodov, S. A.; Wennberg, P. O., First Spectroscopic Observation of Gas-Phase HOONO. *J Phys Chem A* **2002**, *106*, 855-859.

5. Drouin, B. J.; Fry, J. L.; Miller, C. E., Rotational Spectrum of *cis-cis* HOONO. *J Chem Phys* **2004**, *120*, 5505-5508.

6. Bean, B. D.; Mollner, A. K.; Nizkorodov, S. A.; Nair, G.; Okumura, M.; Sander, S. P.; Peterson, K. A.; Francisco, J. S., Cavity Ringdown Spectroscopy of *cis-cis* HOONO and the HOONO/$HONO_2$ Branching Ratio in the Reaction OH+NO_2+M. *J Phys Chem A* **2003**, *107*, 6974-6985.

7. Fry, J. L.; Nizkorodov, S. A.; Okumura, M.; Roehl, C. M.; Francisco, J. S.; Wennberg, P. O., *Cis-cis* and *trans-perp* HOONO: Action Spectroscopy and Isomerization Kinetics. *J Chem Phys* **2004**, *121*, 1432-1448.

8. Zhang, X.; Nimlos, M. R.; Ellison, G. B.; Varner, M. E.; Stanton, J. F., Infrared Absorption Spectra of Matrix-Isolated *cis-cis* HOONO and Its Ab Initio CCSD(T) Anharmonic Vibrational Bands. *J Chem Phys* **2006**, *124*.

9. Burkholder, J. B. S. S. P. A., J.; Barker, J. R.; Huie, R. E.; Kolb, C. E.; Kurylo, M. J.; Orkin, V. L.; Wilmouth, D. M.; Wine, P. H., Chemical Kinetics and Photochemical Data for Use in Atmospheric Studies, Evaluation No. 18. *JPL Publication 15-10, Jet Propulsion Laboratory, Pasadena, 2015* http://jpldataeval.jpl.nasa.gov **2015**.

10. Atkinson, R.; Baulch, D. L.; Cox, R. A.; Crowley, J. N.; Hampson, R. F.; Hynes, R. G.; Jenkin, M. E.; Rossi, M. J.; Troe, J., Evaluated Kinetic and Photochemical Data for Atmospheric Chemistry: Volume I - Gas Phase Reactions of O_x, HO_x, NO_x and SO_x Species. *Atmos Chem Phys* **2004**, *4*, 1461-1738.

11. Mollner, A. K.; Valluvadasan, S.; Feng, L.; Sprague, M. K.; Okumura, M.; Milligan, D. B.; Bloss, W. J.; Sander, S. P.; Martien, P. T.; Harley, R. A.; McCoy, A. B.; Carter, W. P. L.., Rate of Gas Phase Association of Hydroxyl Radical and Nitrogen Dioxide. *Science* **2010**, *330*, 646-649.

12. Hippler, H.; Krasteva, N.; Nasterlack, S.; Striebel, F., Reaction of $OH+NO_2$: High Pressure Experiments and Falloff Analysis. *J Phys Chem A* **2006**, *110*, 6781-6788.

13. Hippler, H.; Nasterlack, S.; Striebel, F., Reaction of $OH+NO_2+M$: Kinetic Evidence of Isomer Formation. *Phys Chem Chem Phys* **2002**, *4*, 2959-2964.

14. Troe, J., Refined Representation of Falloff Curves for the Reaction $HO+NO_2+N_2 \rightarrow (HONO_2, HOONO)+N_2$. *J Phys Chem A* **2012**, *116*, 6387-6393.

15. B. Ruscic and D. H. Bross, *Active Thermochemical Tables (ATcT) values based on ver. 1.122g of the Thermochemical Network (2019); available at ATcT.anl.gov*.

16. Golden, D. M.; Barker, J. R.; Lohr, L. L., Master Equation Models for the Pressure- and Temperature-Dependant Reactions $HO+NO_2 \rightarrow HONO_2$ and $HO+NO_2 \rightarrow HOONO$. *J Phys Chem A* **2003**, *107*, 11057-11071.

17. Newsome, B.; Evans, M., Impact of Uncertainties in Inorganic Chemical Rate Constants on Tropospheric Composition and Ozone Radiative Forcing. *Atmos Chem Phys* **2017**, *17*, 14333-14352.

18. Sprague, M. K.; Garland, E. R.; Mollner, A. K.; Bloss, C.; Bean, B. D.; Weichman, M. L.; Mertens, L. A.; Okumura, M.; Sander, S. P., Kinetics of *n*-Butoxy and 2-Pentoxy Isomerization and Detection of Primary Products by Infrared Cavity Ringdown Spectroscopy. *J Phys Chem A* **2012**, *116*, 6327-6340.

19. Sprague, M. K.; Mertens, L. A.; Widgren, H. N.; Okumura, M.; Sander, S. P.; McCoy, A. B., Cavity Ringdown Spectroscopy of the Hydroxy-Methyl-Peroxy Radical. *J Phys Chem A* **2013**, *117*, 10006-10017.

20. Aker, P. M.; Sloan, J. J., The Initial Product Vibrational-Energy Distribution in the Reaction between $O(^1D_2)$ and H_2. *J Chem Phys* **1986**, *85*, 1412-1417.

21. Cheskis, S. G.; Iogansen, A. A.; Kulakov, P. V.; Razuvaev, I. Y.; Sarkisov, O. M.; Titov, A. A., OH Vibrational Distribution in the Reaction $O(^1D)+CH_4$. *Chem Phys Lett* **1989**, *155*, 37-42.

22. Smith, I. W. M.; Williams, M. D., Vibrational Relaxation of OH (v=1) and OD (v=1) by HNO_3, DNO_3, H_2O, NO and NO_2. *J Chem Soc Farad T 2* **1985**, *81*, 1849-1860.

23. Sharpe, S. W.; Johnson, T. J.; Sams, R. L.; Chu, P. M.; Rhoderick, G. C.; Johnson, P. A., Gas-Phase Databases for Quantitative Infrared Spectroscopy. *Appl Spectrosc* **2004**, *58*, 1452-1461.

24. McCoy, A. B.; Sprague, M. K.; Okumura, M., The Role of Torsion/Torsion Coupling in the Vibrational Spectrum of *cis-cis* HOONO. *J Phys Chem A* **2010**, *114*, 1324-1333.

25. Chackerian, C.; Sharpe, S. W.; Blake, T. A., Anhydrous Nitric Acid Integrated Absorption Cross Sections: 820-5300 cm^{-1}. *J Quant Spectrosc Ra* **2003**, *82*, 429-441.

26. Yalin, A. P.; Zare, R. N., Effect of Laser Lineshape on the Quantitative Analysis of Cavity Ring-Down Signals. *Laser Phys* **2002**, *12*, 1065-1072.

27. Bey, I.; Jacob, D. J.; Yantosca, R. M.; Logan, J. A.; Field, B. D.; Fiore, A. M.; Li, Q. B.; Liu, H. G. Y.; Mickley, L. J.; Schultz, M. G., Global Modeling of Tropospheric Chemistry with Assimilated Meteorology: Model Description and Evaluation. *J Geophys Res-Atmos* **2001**, *106*, 23073-23095.

Chapter 4 – Rate Constants of the CN + Benzene and CN + Toluene Reactions from 15 – 294 K, and Interstellar Implications

This chapter is reprinted and adapted with permission from J. Phys. Chem. A 2020, 124, 39, 7950–7958. Copyright 2020, American Chemical Society. Additional data is from Astrophys. J. Lett. 2020, 891:L41

4.1 – Abstract

CN is known for its fast reactions with hydrocarbons at low temperatures, but relatively few studies have focused on the reactions between CN and aromatic molecules. The recent detection of benzonitrile in the interstellar medium, believed to be produced by the reaction of CN and benzene, has ignited interest in studying these reactions. Here, we report rate constants of the CN + benzene (C_6H_6) and CN + toluene (C_7H_8) reactions between 15 and 294 K using a CRESU apparatus coupled with the pulsed laser photolysis – laser induced fluorescence (PLP-LIF) technique. We also present the stationary points on the CN + toluene potential energy surface of this reaction to study the available reaction pathways. We find that both rate constants do not change over this temperature range, with an average value of $(4.4 \pm 0.2) \times 10^{-10}$ cm^3 s^{-1} for the CN + benzene reaction, in good agreement with previous measurements, and $(4.1 \pm 0.2) \times 10^{-10}$ cm^3 s^{-1} for the CN + toluene reaction, which is notably faster than the only previous measurement at 105 K. While the reason for this disagreement is unknown, we discuss the possibility that it is related to enhanced multiphoton effects in the previous work.

4.2 – Introduction

The CN radical has long been known to be abundant in the interstellar medium (ISM), where it was first detected in 1940s,[1-2] and in the atmosphere of Titan, where it leads the formation of nitrile compounds, including C_2H_3CN and HC_3N.[3-5] At the low temperatures found in these environments, reactions between CN and other compounds are known to have fast rate constants, on the order of 10^{-10} cm^3 s^{-1}, and thus must be included in gas-phase models. Reactions between CN and hydrocarbons are among the fastest of these rates, and proceed through either an abstraction or an addition mechanism.[6] A number of cyano-containing molecules linked to these reactions have been found in ISM, including molecules as large as HC_9N[7] and $(CH_3)_2CHCN$.[8] On Titan, the photolysis of these nitrile compounds formed from CN reactions may contribute to the formation of particulate matter.[9]

On Titan, both benzene and toluene have been detected in the upper atmosphere by the Cassini Ion and Neutral Mass Spectrometer,[10-11] and while currently undetected in the lower atmosphere, models suggest both have high abundances there as a product of the fast association reactions between C_6H_5 and H or CH_3.[12] In addition to benzene and toluene, a large number of specific polycyclic aromatic hydrocarbons (PAHs) have also been identified.[13] These PAHs are believed to form from smaller aromatic compounds and to be an important component of the thick haze in Titan's atmosphere.[14]

On the other hand, very few specific aromatic molecules have been directly detected in the ISM, in part due to their low dipole moments making them unable to be observed by radio astronomy. Benzene has been observed through observations of weak infrared transitions,[15] and PAHs are widely believed to be abundant in the ISM owing to observations of the strong infrared bands characteristic of these molecules, but the broad, overlapping nature of these bands has precluded the identification of specific PAHs.[16] Despite this lack of definitive identifications, PAHs are believed to hold a large fraction of carbon in the ISM,[17-18] and so their formation has been the subject of extensive study.[19-21] The formation of the first aromatic ring is believed to be the rate limiting step in PAH formation,[22] and so understanding the chemistry of these monocyclic aromatic compounds is necessary.

The recent detection of benzonitrile in the ISM[23] has suggested a new route for understanding aromatic formation. Benzonitrile is believed to be the product from the CN + benzene reaction. Observations of benzonitrile therefore can be used as a proxy for the abundance of benzene. Other aromatic nitriles may also serve as proxies for undetected aromatic compounds in the ISM, as the addition of the cyano moiety gives these compounds large dipole moments and makes them visible to radio astronomy. The identification of additional specific aromatic compounds would significantly constrain models of PAH formation in the ISM.

However, little is known about the rates and products of the reactions of CN with aromatic molecules. The only previous measurements come from Trevitt et al.[24], who studied the CN + benzene reaction at 105, 165 and 29 K, and the CN + toluene reaction at 106 K, using pulsed laser photolysis – laser induced fluorescence (PLP-LIF) measurements in conjunction with a pulsed Laval nozzle. For the benzene reaction, they found a rate of $(3.9 - 4.9) \times 10^{-10}$ cm^3 s^{-1}, with no change as function of temperature, and for the toluene reaction, they determined a rate constant of $(1.3 \pm 0.3) \times 10^{-10}$ cm^3 s^{-1}. The fact that the rate constant of the CN + toluene reaction is a factor of 3 lower than the rate constants measured for the CN + benzene reaction suggest that the structure of aromatic molecules can play a large role in the reaction rates. Furthermore, they observed non-exponential decays of CN at room temperature in the presence of toluene and were therefore unable to measure a rate constant, in contrast with their measurements of benzene under the same conditions. They suggested that this could be due to dissociation of the products back to the CN + toluene reactants, and that further studies would be necessary to better understand these results.

The lack of experimental rate constants for the CN + benzene reaction at temperatures relevant to the interstellar medium would improve our understanding of this reaction and determine whether it may be the pathway that forms benzonitrile in the ISM. Furthermore, the difference between the rate constants of the CN + benzene and CN + toluene reactions suggests that the structure of an aromatic compound can play a large role in the reaction dynamics. This makes it questionable whether nitrile compounds may be formed from the reactions of CN with larger, more complex aromatic compounds, and it is essential to verify the reliability of using cyano-substituted compounds as a proxy for larger aromatic species. To these ends, we have conducted measurements of the CN + benzene and CN + toluene rate constants between 15 and 294 K to gain further insight into these reactions, especially at the low temperatures relevant to the ISM and Titan. Furthermore, we have computed stationary points on the potential energy surface (PES) of the CN + toluene reaction, which have not been previously determined, to better understand the possible products and mechanism of this reaction.

4.3 – Experimental Methods

Rate constants were determined using the PLP-LIF technique. Temperatures down to 15 K were achieved using the CRESU technique which has been described in detail previously[6, 25-26] and in Chapter 2. Briefly, benzene (Sigma Aldrich, anhydrous 99.8%) or toluene (Sigma Aldrich, 99.9%) were introduced into the gas flow with a Controlled Evaporation and Mixing system (Bronkhorst CEM), as described in Gupta et al.[27] The benzene/toluene and ICN (Acros Organics, 98%), used as the CN precursor, were mixed in a buffer gas of He (99.995%, Air Liquide), Ar (99.998%, Air Liquide) or N_2 (99.995%, Air Liquide), depending on the desired CRESU conditions. Concentrations of benzene/toluene and ICN were kept < 1% of the total density in order not to affect the uniformity of the gas flow. The mixture was flowed isentropically from a high-pressure reservoir through specifically designed convergent-divergent Laval nozzles, into a low-pressure chamber to generate a uniform supersonic flow at the appropriate temperature with a density of $10^{16} – 10^{17}$ cm^{-3}. Each nozzle was characterized with Pitot probe impact pressure measurements prior to experiments to determine the temperature, density and uniformity of the gas flow. For measurements at 294 K, where a supersonic expansion is not required, the pumping speed was decreased such that the pressure in the reservoir and the chamber were equal, while maintaining complete gas turnover for each laser shot.

As detailed in Chapter 2, CN radicals were generated by the 248 nm photolysis of ICN using a KrF excimer laser operating at 10 Hz, with a laser fluence of 25 mJ cm^{-2}. The third harmonic of a Nd:YAG laser, also operating at 10 Hz, was used to pump a dye laser containing Exalite 389 in 1,4-dioxane to produce ~389 nm light to excite the CN $B^2\Sigma^+$ - $X^2\Sigma^+$ (0,0) transition. Fluorescence was detected from the CN (0,1) transition at ~420 nm by a photomultiplier tube preceded by a 420 nm bandpass filter. The delay time between the excimer and the Nd:YAG pump laser was varied from -5 to 200 microseconds to record the time dependence of the CN signal. The LIF signal was recorded by a gated integrator at 400 evenly spaced points and averaged 5 times. The resulting kinetic trace was fit to an exponential decay starting ≥ 10 μs after photolysis to allow for rotational thermalization of CN.

Kinetic measurements were taken under pseudo-first order conditions with [aromatic] >> [CN]. Typical benzene and toluene concentrations were on the order of 10^{12} – 10^{13} cm^{-3}, while we estimate the CN concentration to be roughly 10^{10} cm^{-3} based on the ICN concentration (~10^{12} cm^{-3}) and 248 nm absorption cross section of 4.7×10^{-19} cm^2.[28] More than 90% of the CN radicals from the photolysis of ICN at 248 nm are in the ground vibrational state[29] and we do not observe any influence of the relaxation of excited vibrational states on our kinetic measurements.

4.4 – Computational Methods

Investigation of possible channels for the reaction between CN and toluene, with identification of all the stationary points (minima, complexes, and transition states), was done by Divita Gupta using Gaussian 09 software[30]; all included channels can be seen in Figure 4.1. All the species, including the reaction complexes and transition states were optimized at (U)M06-2X/aug-cc-pVTZ level[31-33] and zero-point corrected energies were calculated for each. In addition, intrinsic reaction coordinate (IRC) calculations were performed at (U)M06-2X/6-311G to determine the minimum energy path that the transition states followed to confirm the connection between the appropriate reactants and products. Gibbs energies ($\Delta_r G^o$ 298 K) at 298 K for all included channels were also calculated at (U)M06-2X/aug-cc-pVTZ method. Both addition-elimination channels, leading to nitrile formation, and abstraction channels, leading to HCN formation, are considered. While reactions involving the CN radical may produce both cyano and isocyano compounds, only the former pathways are considered in these calculations. Previous work on the CN + benzene reaction[34] showed a significant barrier (28 kJ mol^{-1}) to isocyano products, which suggests that this pathway will not be relevant in the ISM.

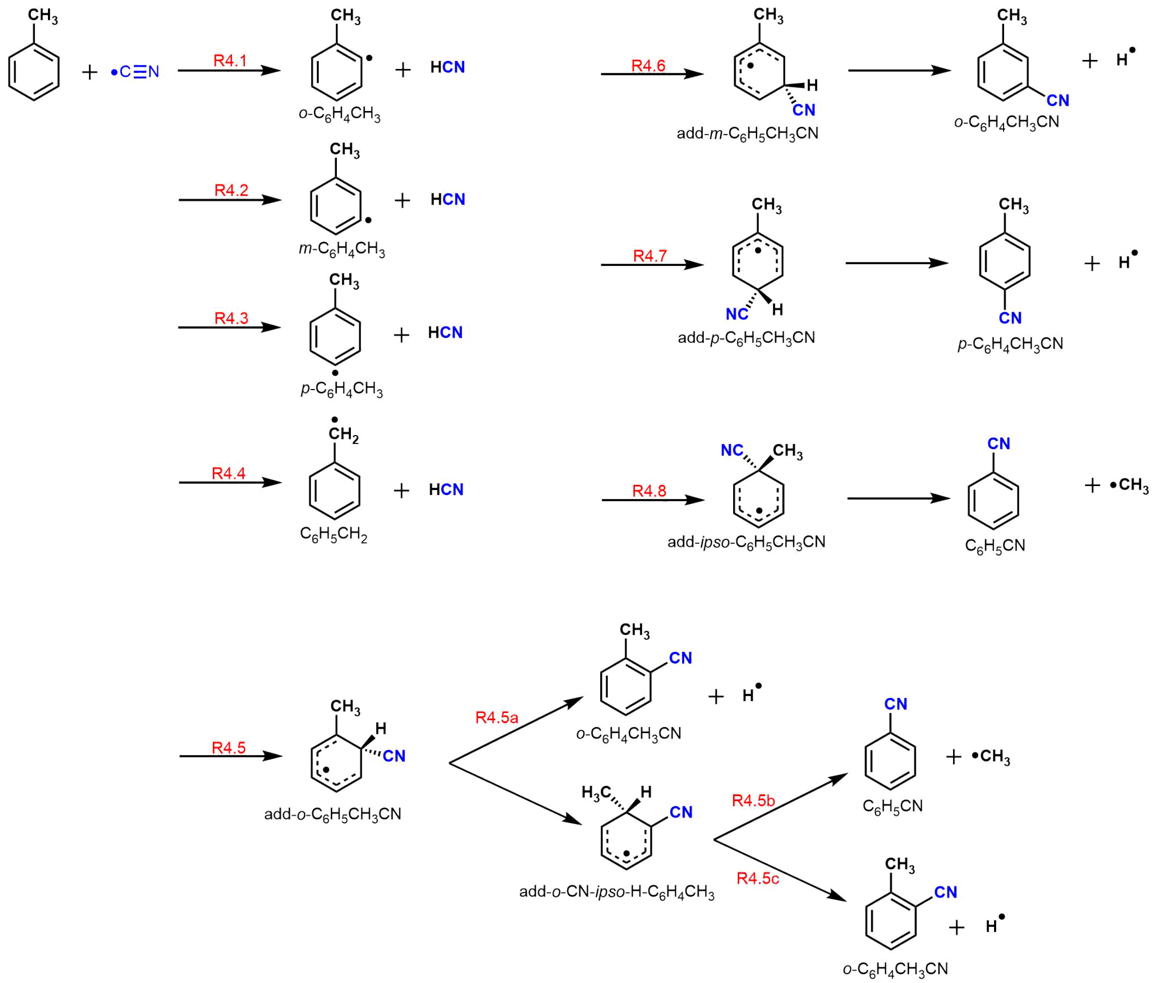

Figure 4.1: The reaction pathways of the CN + toluene reaction and possible products of the abstraction (R4.1-R4.4) and CN-addition (R4.5-R4.8) channels that are considered in the theoretical calculations.

4.5 – Results

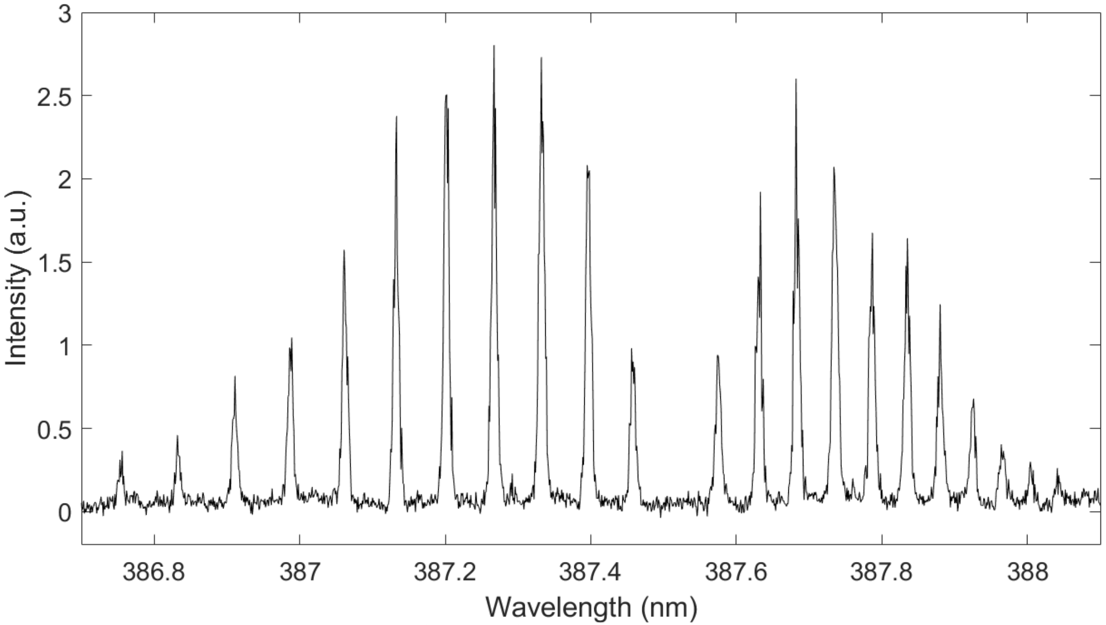

Figure 4.2: LIF spectrum of the $B^2\Sigma^+$ - $X^2\Sigma^+$ (0,0) transition of the CN radical at 72 K in He.

An experimental spectrum of the CN $B^2\Sigma^+$ - $X^2\Sigma^+$ (0,0) spectrum at 72 K can be seen in Figure 4.2. As the temperature decreases, fewer rotational states of CN have significant populations and therefore fewer transitions are observed. Typical LIF decays of CN from the CN + toluene reaction at 83 K and 294 K and the second-order plots can be seen in Figures 4.3 and 4.4, respectively. The non-zero intercepts seen on the second-order plots arise from the loss of CN via side chemistry and diffusion out of the region probed by LIF. From experiments at room temperature, using He and N_2 as the buffer gases, and varying the total density of the gas flow, we found that the rate constants for both reactions have no pressure dependence, implying that the reactions are either bimolecular reactions, or termolecular reactions in the high pressure limit in our experimental conditions. Unlike the room temperature measurements of the CN + toluene reaction by Trevitt et al., we see no evidence for non-exponential decays at any toluene concentration or total gas density used in these experiments, and the measured rate constants are in good agreement with our values at all other temperatures.

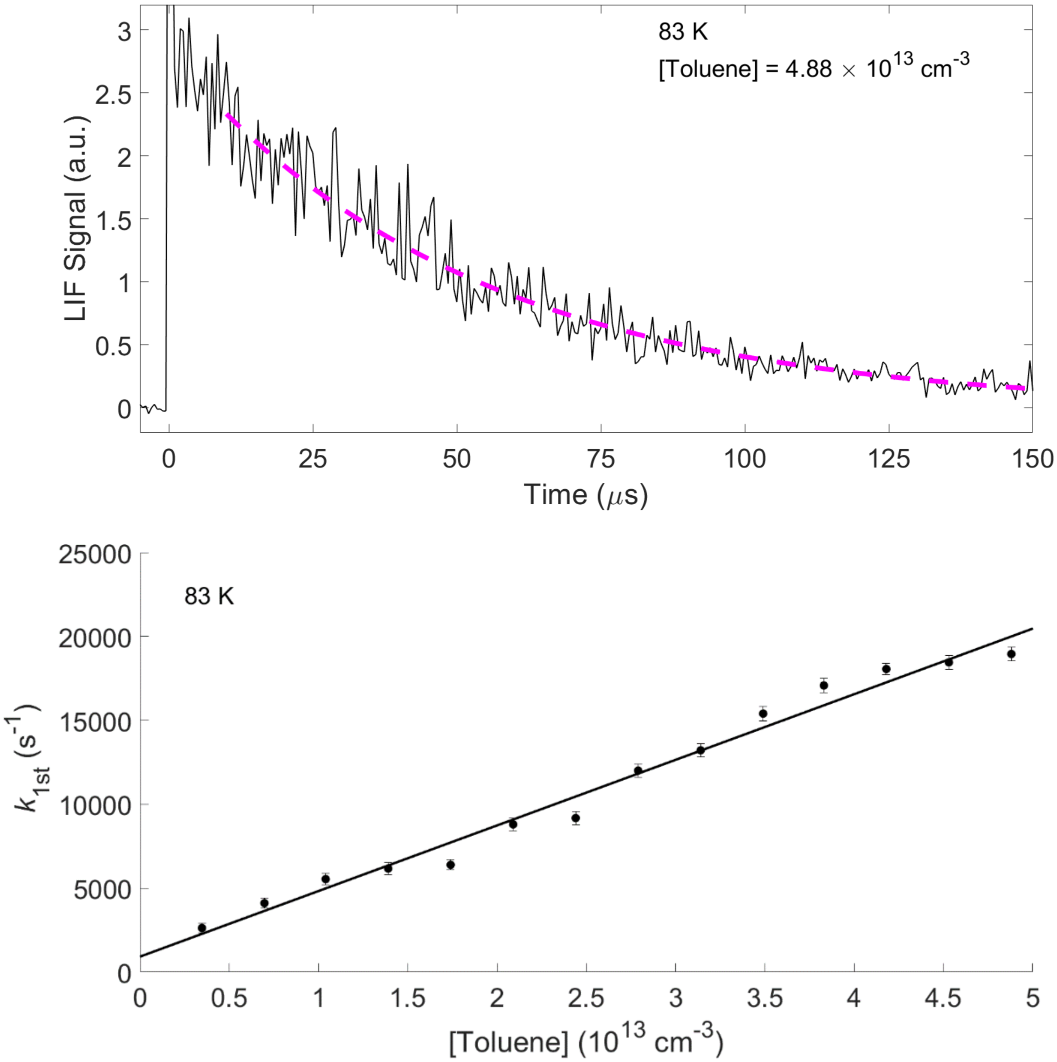

Figure 4.3: Typical experimental kinetics of the CN + toluene reaction measured using PLP-LIF, showing the decay of the CN signal (top) and resulting second-order plot at 83 K (bottom).

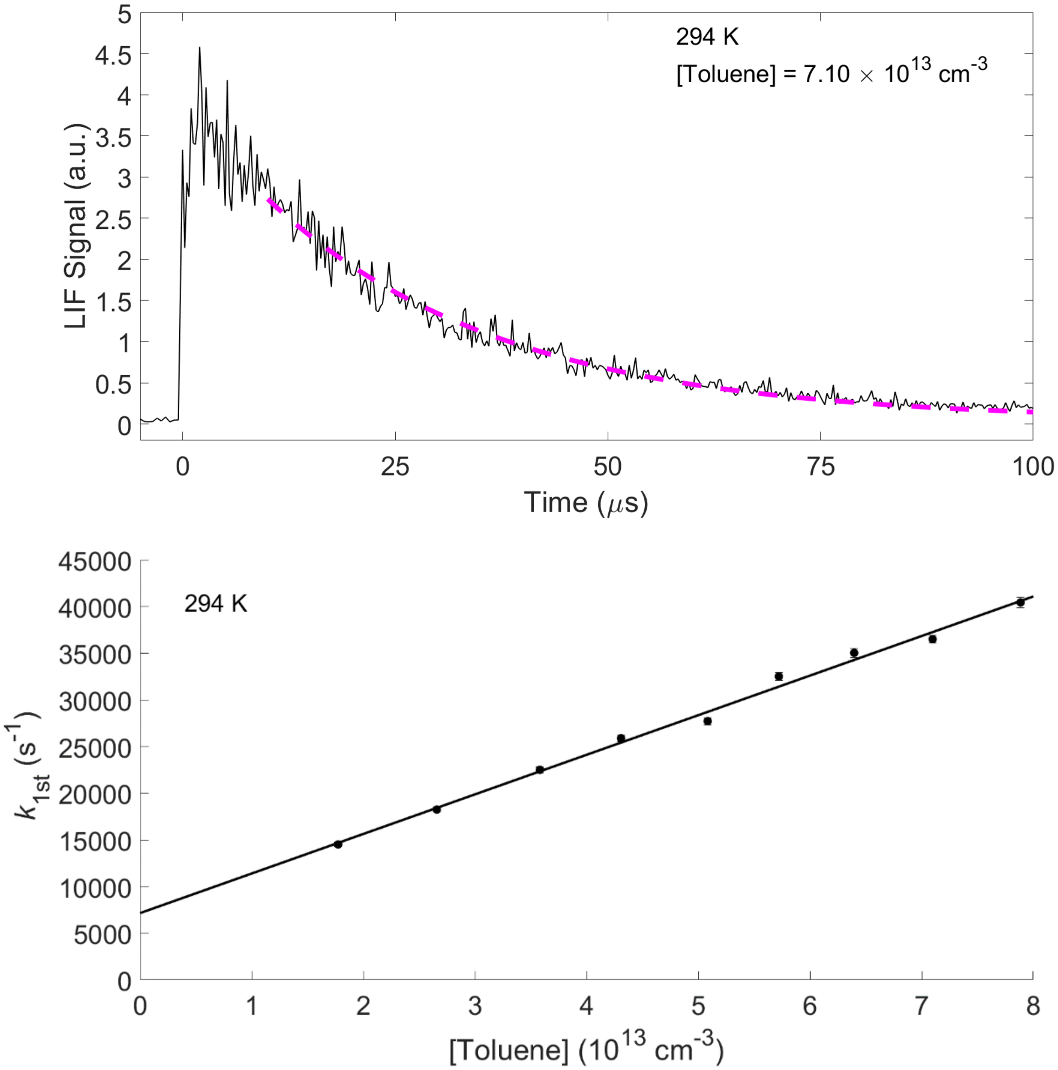

Figure 4.4: Typical experimental kinetics of the CN + toluene reaction measured using PLP-LIF, showing the decay of the CN signal (top) and resulting second-order plot at 294 K (bottom).

Results of the experiments between 15 and 294 K are shown in Table 4.1 and Figure 4.5 for the CN + benzene reaction, and Table 4.2 and Figure 4.6 for the CN + toluene reaction. At least eight points with varying benzene/toluene concentrations were taken for each measurement under pseudo-first order conditions, with the aromatic molecule in excess. At high aromatic concentrations, the formation of benzene or toluene dimers causes nonlinear behavior in the second-order plots at the lowest temperatures. This therefore imposes an upper limit on the benzene and toluene concentrations used in experiments in order to minimize any effect of the reaction between CN and aromatic dimers on our measurements.

Table 4.1: Rate coefficients determined for the CN + benzene reaction between 15 and 294 K, along with experimental parameters for each measurement. Uncertainties in the rate constant are the 95% confidence interval from the appropriate Student's *t* test combined in quadrature with a 10% systematic error. Bolded values represent the weighted average and uncertainty for temperatures with multiple measurements.

Temperature (K)	Buffer Gas	Total Density (10^{16} cm^{-3})	[Benzene] (10^{12} cm^{-3})	Number of Points	Rate Constant (10^{-10} cm^3 s^{-1})
15	He	5.02	2.19 – 19.7	13	5.5 ± 0.9
15	He	5.02	2.19 – 17.5	14	5.4 ± 0.9
					5.4 ± 0.6
17	He	4.85	2.03 – 14.2	13	4.5 ± 0.7
24	He	4.85	2.08 – 22.8	11	5.1 ± 0.7
36	He	5.31	1.48 – 14.8	11	5.4 ± 0.7
36	He	5.27	1.47 – 20.6	14	5.5 ± 0.9
36	He	5.27	1.47 – 14.7	11	5.2 ± 0.8
					5.3 ± 0.6
72	He	6.01	1.54 – 24.6	14	5.5 ± 0.6
72	He	6.01	3.00 – 16.5	12	5.1 ± 0.7
					5.4 ± 0.6
83	N_2	4.61	2.06 – 16.5	8	3.9 ± 0.7
83	N_2	4.61	2.04 – 24.6	12	3.9 ± 0.6
					3.9 ± 0.4
110	Ar	2.71	1.66 – 19.9	11	4.2 ± 0.6
200	N_2	5.27	2.52 – 20.2	13	3.7 ± 0.8
294	N_2	7.04	1.52 – 76.1	9	3.5 ± 0.4
293	N_2	9.78	1.53 – 76.6	9	3.5 ± 0.4
293	N_2	18.5	2.21 – 69.6	8	3.3 ± 0.5
293	He	5.27	6.25 – 37.5	9	4.0 ± 0.6
293	He	6.92	2.03 – 81.3	10	3.4 ± 0.5
293	He	9.39	2.16 – 63.4	6	4.1 ± 0.6
295	He	9.10	1.50 – 74.8	9	4.0 ± 0.5
					3.6 ± 0.4

Table 4.2: Rate coefficients determined for the CN + toluene reaction between 15 and 294 K, along with experimental parameters for each measurement. Uncertainties in the rate constant are the 95% confidence interval from the appropriate Student's *t* test combined in quadrature with a 10% systematic error. Bolded values represent the weighted average and uncertainty for temperatures with multiple measurements.

Temperature (K)	Buffer Gas	Total Density (10^{16} cm^{-3})	[Toluene] (10^{12} cm^{-3})	Number of Points	Rate Constant (10^{-10} cm^3 s^{-1})
15	He	5.04	1.87 – 10.4	10	4.4 ± 0.8
24	He	4.83	1.76 – 19.5	11	4.7 ± 0.6
36	He	5.27	1.25 – 17.7	14	5.9 ± 0.8
36	He	5.32	1.28 – 12.7	9	4.9 ± 1.0
					5.7 ± 0.7
70	He	6.00	2.54 – 15.2	11	4.4 ± 0.7
70	He	6.09	1.34 – 18.7	13	4.2 ± 0.7
					4.3 ± 0.6
83	N_2	4.63	3.48 – 48.8	14	3.9 ± 0.5
83	N_2	4.63	1.72 – 31.3	14	3.8 ± 0.4
					3.9 ± 0.4
110	Ar	2.71	1.28 – 14.1	11	3.3 ± 0.5
197	N_2	5.32	2.13 – 21.4	11	3.7 ± 0.6
294	N_2	10.5	15.4 – 92.9	11	3.7 ± 0.6
294	N_2	3.75	9.50 – 47.6	9	4.3 ± 0.6
294	N_2	8.20	17.7 – 78.9	9	4.3 ± 0.5
294	He	9.41	18.0 – 54.0	11	4.5 ± 0.5
					4.3 ± 0.5

To test whether the photolysis of benzene or toluene at 248 nm affected our measurements, we also conducted experiments varying the power of the excimer laser, by determining whether the decay of the CN radical changed as a function of excimer power. The benzene experiments were conducted at 24 K and [benzene] = 2×10^{12} cm^{-3}, and the toluene experiments were conducted at 110 K, with [toluene] = 9×10^{12} cm^{-3}. We found no significant change in the measured k_{1st} as a function of our laser power for either. With the excimer laser fluence of 25 mJ cm^{-2} and the absorption cross sections at 248 nm (1.4×10^{-19} cm^2 for benzene[35] and 2.9×10^{-19} cm^2 for toluene[36]) we expect roughly 1% of the aromatic compounds to photolyze if the photolysis quantum yield is 1, which should not measurably affect the observed rate constants. However, it has been suggested that photolysis does not occur after single photon absorption at 248 nm, only two-photon absorption, which can photolyze the aromatics to form H atoms among other potential processes.[37] The total absorption cross section for the second photon experimentally determined to be 2.8 × 10^{-17} cm^2 for benzene and 1.7 × 10^{-17} cm^2 for toluene.[37] For the highest aromatic concentrations used (~1 × 10^{14} cm^{-3}), we estimate at most 4.8 × 10^{11} cm^{-3} of benzene or toluene undergoes two-photon absorption, though it is likely much less than that, as discussed in greater detail in the following section in the case of toluene, and is unlikely to affect the rate constants measured.

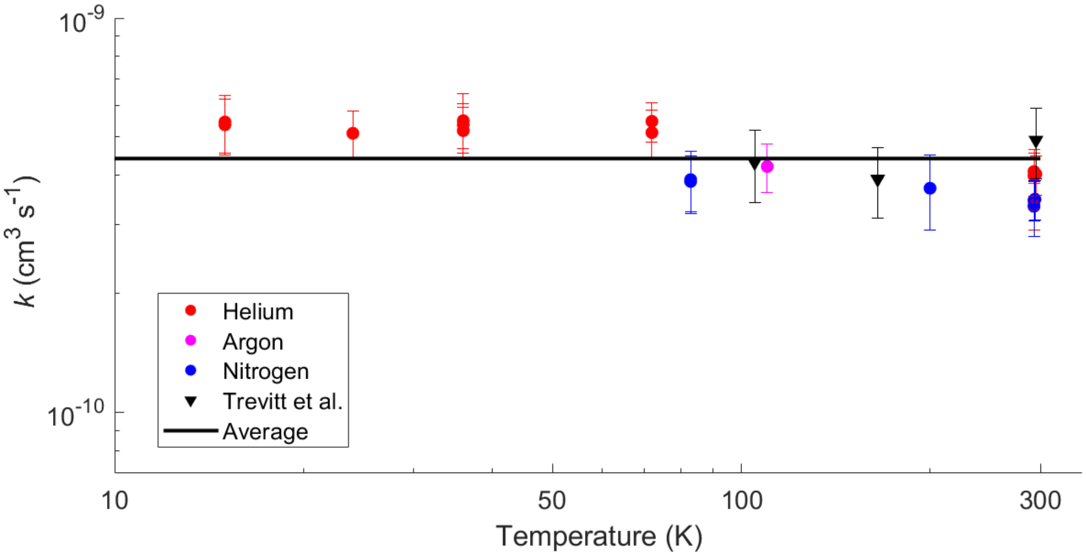

Figure 4.5: The experimental measurements for the CN + benzene rate constant from this work (circles) and Trevitt et al. (triangles); the weighted average value of the measurements presented in this work, 4.4 × 10^{-10} cm^3 s^{-1}, is also plotted.

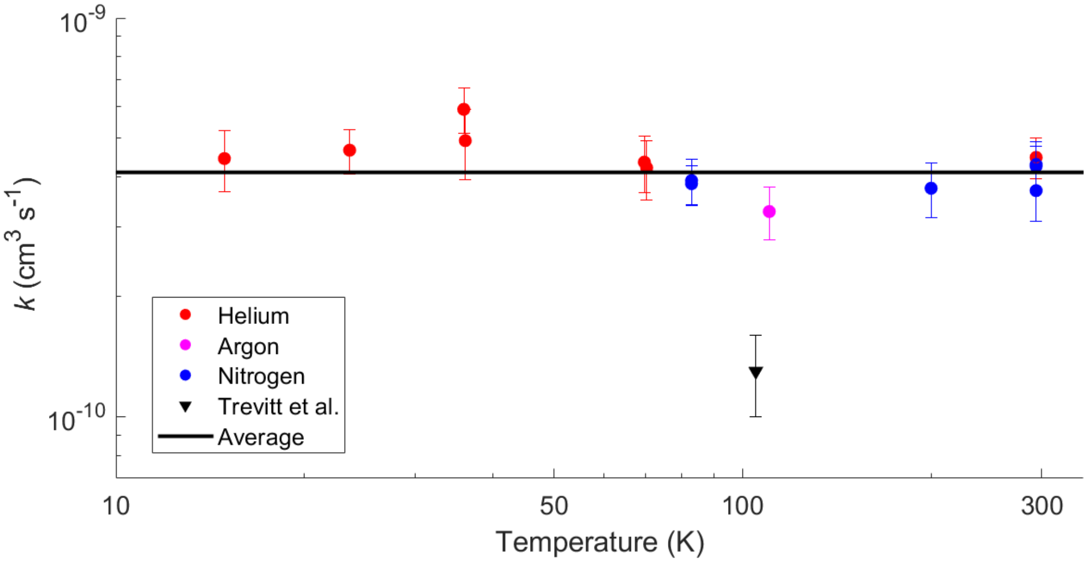

Figure 4.6: The experimental measurements for the CN + toluene rate constant from this work (circles) and Trevitt et al. (triangle); the weighted average value of the measurements presented in this work, 4.1 × 10^{-10} cm^3 s^{-1}, is also plotted.

Table 4.3: Zero-point corrected reaction energies and Gibbs energies of the CN + toluene reaction products calculated in this work. Note that some reaction pathways result in the same products.

Reaction channel products	Reaction energy $\Delta_r U^o$ (kcal mol^{-1})	Gibbs energy $\Delta_r G^o$ (298 K) (kcal mol^{-1})
R4.1 (o-$C_6H_4CH_3$ + HCN)	-18.1	-18.1
R4.2 (m-$C_6H_4CH_3$ + HCN)	-18.3	-18.6
R4.3 (p-$C_6H_4CH_3$ + HCN)	-17.8	-18.2
R4.4 ($C_6H_5CH_2$ + HCN)	-39.1	-38.1
R4.5a (= R5c, o-$C_6H_4CH_3CN$ + H)	-28.0	-23.6
R4.5b (= R8, C_6H_5CN + CH_3)	-35.4	-35.5
R4.5c (= R5a, o-$C_6H_4CH_3CN$ + H)	-28.0	-23.6
R4.6 (m-$C_6H_4CH_3CN$ + H)	-26.8	-22.5
R4.7 (p-$C_6H_4CH_3CN$ + H)	-27.2	-23.8
R4.8 (= R5b, C_6H_5CN + CH_3)	-35.4	-35.5

As shown in the Figure 4.7, both stationary points (reactants, products, intermediates, transition states) for both the abstraction (R4.1-R4.4) and addition-elimination (R4.5-R4.8) channels were characterized for the reaction between CN and toluene. An additional substitution channel, leading to the formation of benzyl cyanide, was found to be exothermic at (U)M06-2X/aug-cc-pVTZ, but has a large barrier (~20 kcal mol^{-1}), and hence will not be relevant under interstellar conditions and is excluded. The relative reaction energy $\Delta_r U^o$ and Gibbs energy at 298 K $\Delta_r G^o$ for all calculated product channels can be seen in Table 4.2. Intermediates formed from the addition of CN to the aromatic ring were found to form barrierlessly, subsequently followed by submerged barriers leading to the formation of stable nitrile products. This mechanism closely resembles the mechanism of benzonitrile formation from the reaction of benzene and CN,[34,38] although it does differ from the reaction between toluene and OH, which features both pre-reactive complexes and barriers before formation of the addition product.[39] The energies determined for the addition-elimination channels are generally similar to those calculated for the CN + benzene reaction done at G3//B3LYP and BCCSD(T)//B3LYP.[34]

Abstraction pathways, shown in blue in Figure 4.5, were found to have slightly submerged transition states, and therefore are possible products at low temperatures. However, higher level calculations are needed to confirm these barrier values, as similar abstraction pathways from aromatic compounds have been shown to possess positive barriers[38-39]. At the level of theory used, these barrier values are likely within the error of the calculations. An important point to note is that no transition state or complex could be characterized for the abstraction channels, though we do not rule out the existence of these stationary points.

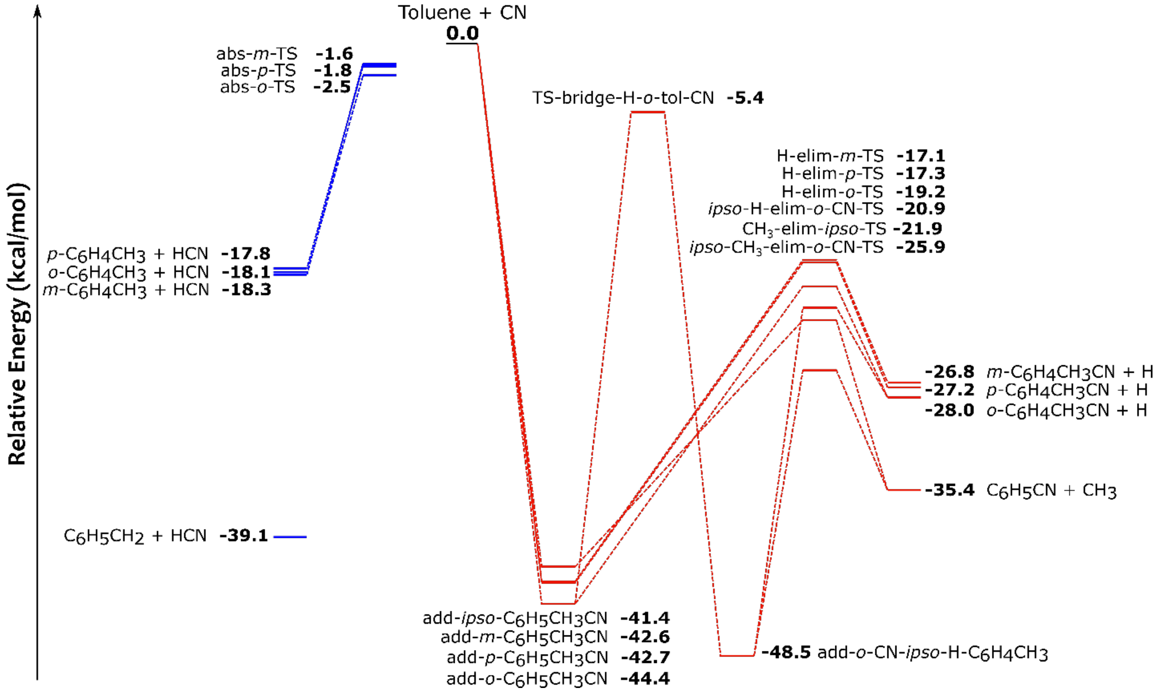

Figure 4.7: The stationary points for PES for the CN + toluene reaction, performed at (U)M06-2X/aug-cc-pVTZ including zero-point energy corrections. Both the abstraction (abs-) pathways (blue) and addition-elimination (add- and elim-) pathways (red) are shown, the latter of which can undergo an internal hydrogen shift (-bridge). Note that neither a barrier leading to the formation of $C_6H_5CH_2$ + HCN nor any pre-reactive complexes for the abstraction pathways are included, though we do not preclude their existence.

4.6 – Discussion

As Figures 4.5 and 4.6 demonstrate, we find that the rate constant of both the CN + benzene reaction and the CN + toluene reactions are independent of temperature over the 15 – 294 K range. We find that the CN + benzene reaction rate constant has a weighted average value of $(4.4 \pm 0.2) \times 10^{-10}$ cm^3 s^{-1} , while the CN + toluene reaction rate constant has a weighted average value of $(4.1 \pm 0.2) \times 10^{-10}$ cm^3 s^{-1}. Our results for the CN + benzene reaction are in good agreement the results of Trevitt et al., but there is a notable discrepancy when comparing our CN + toluene results, as they measured a rate constant of (1.3 ± 0.3) $\times 10^{-10}$ cm^3 s^{-1} for that reaction at 106 K in their LIF experiments. They used a similar LIF method to detect CN, under similar experimental conditions of total density, and CN and toluene concentrations. Furthermore, the agreement our respective CN + benzene rate constants suggests that this discrepancy is related somehow to the toluene system.

Trevitt et al. reported observing non-exponential decays of CN at room temperature, which they suggested might be due to back-dissociation of adduct complexes. However, no such behavior was observed in this work, suggesting that the discrepancy might have arisen from differences in the photolysis step. Trevitt et al. photolyzed their sample at a wavelength of 266 nm, with a laser fluence of 40 mJ cm^{-2} (5.0×10^{16} photons cm^{-2}, in a probable 3-5 ns long pulse), in contrast to the 248 nm laser beam with a fluence of 25 mJ cm^{-2} (3.1×10^{16} photons cm^{-2}, 22 ns long pulse) used in this work. The ICN photolysis cross sections are similar at these two wavelengths.[28, 40] At room temperature, the toluene absorption cross section to the S_1 state at 266 nm is 1.3×10^{-19} cm^2.[41] The S_1 state fluoresces with a lifetime of 86 ns when excited at 266 nm at low pressures.[42] At 248 nm, the cross section is larger (2.9×10^{-19} cm^2)[41] but the fluorescence lifetime is much shorter due to rapid internal conversion to S_0, displaying approximately equal intensity 3 ns and 26 ns components at low pressures.[43] As discussed above, multiphoton absorption at 248 nm of toluene is known to lead to photolysis,[37] and may additionally lead to photoionization, as the excited toluene is higher in energy than the ionization onset of toluene (8.3 eV).[44] Both of these processes are also likely to occur in the 266 nm experiments.

The above considerations suggest that single photon excitation of toluene is occurring at both photolysis wavelengths, but only multiphoton effects are likely to give rise to interferences. Possible pathways for CN generation on the timescale of the experiment exist by either two-photon photodissociation or two-photon ionization, particularly at 266 nm by quadrupled Nd:YAG lasers. Such effects are likely to be significantly lower when toluene is excited at 248 nm light produced by an excimer, due to the longer pulse duration and rapid internal conversion of the S_1 state. This is in good agreement with the experimental measurements reported here, showing no relationship between excimer power and k_{1st}, and no evidence for non-exponential decays. In the experiments of Trevitt et al. at 266 nm, however, the long lifetime of the S_1 state, short photolysis pulse duration and higher laser fluence may have caused larger amounts of multi-photon absorption to occur, such that photodissociation or photoionization products could have affected their measurements.

Further work from Trevitt et al. measured the products of the CN + benzene and CN + toluene reactions at room temperature, using slow flow reactors in conjunction with product detection by multiplexed photoionization mass spectrometry (MPIMS) to identify species by mass and photoionization spectrum. They found that the reaction between CN and benzene exclusively forms benzonitrile, while the CN and toluene exclusively forms tolunitrile (methylbenzonitrile), with no evidence for the hydrogen abstraction channels or methyl-loss channels. Due to the similarities in the calculated photoionization spectra of the *ortho*, *meta*, and *para* isomers of the tolunitrile, they were unable to distinguish the precise isomers of tolunitrile formed from CN + toluene. Lenis and Miller also measured the products of the CN + toluene reaction using the 254 nm photolysis of ICN and analyzing the resulting products with GC-MS[45] and observed both tolunitrile and a small yield (9%) of benzonitrile. While it is unclear if this benzonitrile is formed as a result of CN + toluene or side chemistry, particularly in light of its non-detection in the MPIMS experiments by Trevitt et al., our calculations do show potential pathways to benzonitrile formation from *ortho* or *ipso* addition of CN to the aromatic ring.

The rate constants measured here for the CN + benzene and the CN + toluene systems are in good agreement with each other. In conjunction with the similarities in products measured by MPIMS, this suggests that the major mechanism is the same for reactions between the CN radical and either benzene or toluene, and results in formation of cyano-substituted aromatic compounds. Investigation of other substituted compounds, such as xylenes or deuterium-substituted benzene, may yield further insight into whether this mechanism is general for these reactions. This will aid in future astronomical searches to improve our understanding of the formation of small aromatic rings in the ISM.

The submerged barriers found for the various channels of the CN + toluene reaction using quantum chemical calculations highlight the diversity of the products that could be formed from this reaction at low temperatures. While the abstraction channels were found to have slightly submerged barriers, calculations at higher level of theory are necessary to correctly estimate their energies. Furthermore, the transition state(s) and/or a possible complex in the case of the hydrogen abstraction from the methyl group pathway remain to be explored further. This will also provide the accuracy necessary for master equation calculations, which would further elucidate the mechanism and product branching ratios of this reaction.

On Titan, the CN radical is mainly generated from the photolysis of HCN, which is formed through reactions of N(^{4}S) or through ion chemistry.[4-5] Once formed, CN reacts primarily with the highly abundant CH_4 to reform HCN. This cycle can be interrupted, however, by CN reactions with other compounds, most commonly C_2H_2 or HC_3N. While this reaction has not explicitly been included in models, recent work has suggested that the concentrations of benzene and toluene in the Titan atmosphere are similar, peaking at a mole fraction of 10^{-6} at an altitude of roughly 1000 km above the surface.[12] Benzonitrile has not been detected on Titan and is predicted to be formed in low quantities, largely due to CN being sequestered by reaction with CH_4. Even with the larger rate constants measured in this work, this is likely also the case for the products of the reaction between CN and toluene, though implementation of these results into Titan models may still be beneficial to determine if they have any influence in the atmosphere.

Astronomical searches for toluene and the tolunitrile products of this reaction would test the robustness of using cyano-containing species as proxies for the unsubstituted hydrocarbons. While benzene has no permanent dipole moment, toluene has a small one (0.37 Debye)[46] and may be observable via radio astronomy, thought it would have to be present in higher abundance than molecules with large dipole moments, like benzonitrile, to be detectable. The use of velocity stacking, which averages the signal of multiple transitions together to increase the signal-to-noise ratio,[47-49] may assist in searching for toluene in the ISM. While there have been no previous detections of toluene in the ISM, it has been argued that the protonated toluene ion, $C_7H_9^+$,[50] and methyl-substituted PAHs[51-52] are possible carriers of the 6.2 and the 3.4 μm unidentified infrared bands, respectively. Definitive detection of toluene and related compounds, such as these, would allow us to constrain aromatic pathways and, in particular, could test the bottom-up mechanism for PAH formation, wherein small molecules, such as toluene, react progressively to form large clusters.

The origin of the first aromatic ring in the interstellar medium in molecules such as benzene and toluene remains unknown. It has been argued that the reaction between C_2H and the unsaturated hydrocarbons 1,3-butadiene and isoprene (C_5H_8; 2-methyl-1,3-butadiene), which are barrierless reactions that produce benzene and toluene, respectively, may be a source of them at low temperatures.[53-54] However, neither 1,3-butadiene nor isoprene have been detected in the ISM. Isoprene is also not included in astrochemical databases such as the Kinetic Database for Astrochemistry[55] (kida.obs.u-bordeaux1.fr, accessed July 2020). Other mechanisms, such as ion-neutral reactions, may also contribute, but further investigation is necessary. The reaction of C_2H and 1,3-butadiene has been used in astrochemical models of the ISM to explain benzene formation,[23] but there is debate as to how much benzene is actually formed from this reaction, as it has been shown that fulvene is the major product.[56]

In order to better understand the potential formation pathways of these products of the CN + toluene in the ISM, more accurate measurements of the product ratios are required, and specifically, the branching ratio for the tolunitrile and potential benzonitrile products. While challenging for many techniques due to the similarities of the isomers, recent work has coupled low temperature supersonic uniform flows to microwave spectrometers[57-58] in order to determine branching ratios relevant for astrochemistry. As each of these compounds will have a unique rotational spectrum, this technique is well suited for quantitatively measuring the product branching ratio of this reaction. Low temperature product measurements of the CN + benzene reaction would also provide further evidence that this reaction is responsible for the formation of benzonitrile in ISM.

4.7 – Conclusions

We have measured rate constants for the CN + benzene and CN + toluene reactions between 15 and 294 K, and find that these rate constants are independent of temperature over this range. These results closely match the previous measurements down to 105 K for the CN + benzene reaction, but are a factor of three higher than the only previous measurement of CN + toluene rate constant at 105 K. The reasons for this discrepancy remain unresolved, but may be related to multiphoton effects at the higher laser intensities and 266 nm photolysis wavelength used in that study. This similarly suggests that the reactions between CN and simple aromatics proceed through an analogous mechanism, which is supported by our theoretical calculations and previous product measurements. Further work, particularly on the products formed from the CN + toluene, would be beneficial to determine their potential detectability in the ISM. The ability to detect and use cyano-substituted aromatics, which have large dipole moments, as proxies for unsubstituted aromatic compounds in the ISM would help advance our knowledge of PAH formation.

4.8 – References

1. Adams, W. S., Some Results with the Coude Spectrograph of the Mount Wilson Observatory. *Astrophys J* **1941**, *93*, 11-23.

2. McKellar, A., Evidence for the Molecular Origin of Some Hitherto Unidentified Interstellar Lines. *Publ Astron Soc Pac* **1940**, *52*, 187 - 192.

3. Yung, Y. L.; Allen, M.; Pinto, J. P., Photochemistry of the Atmosphere of Titan - Comparison between Model and Observations. *Astrophys J Suppl S* **1984**, *55*, 465-506.

4. Loison, J. C.; Hebrard, E.; Dobrijevic, M.; Hickson, K. M.; Caralp, F.; Hue, V.; Gronoff, G.; Venot, O.; Benilan, Y., The Neutral Photochemistry of Nitriles, Amines and Imines in the Atmosphere of Titan. *Icarus* **2015**, *247*, 218-247.

5. Wilson, E. H.; Atreya, S. K., Current State of Modeling the Photochemistry of Titan’s Mutually Dependent Atmosphere and Ionosphere. *J Geophys Res* **2004**, *109*, E06002.

6. Cooke, I. R.; Sims, I. R., Experimental Studies of Gas-Phase Reactivity in Relation to Complex Organic Molecules in Star-Forming Regions. *ACS Earth Space Chem* **2019**, *3*, 1109-1134.

7. Broten, N. W.; Oka, T.; Avery, L. W.; Macleod, J. M.; Kroto, H. W., The Detection of HC_9N in Interstellar Space. *Astrophys J* **1978**, *223*, L105-L107.

8. Belloche, A.; Garrod, R. T.; Muller, H. S. P.; Menten, K. M., Detection of a Branched Alkyl Molecule in the Interstellar Medium: Iso-Propyl Cyanide. *Science* **2014**, *345*, 1584-1587.

9. Gudipati, M. S.; Jacovi, R.; Couturier-Tamburelli, I.; Lignell, A.; Allen, M., Photochemical Activity of Titan’s Low-Altitude Condensed Haze. *Nat Commun* **2013**, *4*, 1648.

10. Magee, B. A.; Waite, J. H.; Mandt, K. E.; Westlake, J.; Bell, J.; Gell, D. A., INMS-Derived Composition of Titan's Upper Atmosphere: Analysis Methods and Model Comparison. *Planet Space Sci* **2009**, *57*, 1895-1916.

11. Vuitton, V.; Yelle, R. V.; Cui, J., Formation and Distribution of Benzene on Titan. *J Geophys Res-Planet* **2008**, *113*.

12. Loison, J. C.; Dobrijevic, M.; Hickson, K. M., The Photochemical Production of Aromatics in the Atmosphere of Titan. *Icarus* **2019**, *329*, 55-71.

13. Lopez-Puertas, M.; Dinelli, B. M.; Adriani, A.; Funke, B.; Garcia-Comas, M.; Moriconi, M. L.; D'Aversa, E.; Boersma, C.; Allamandola, L. J., Large Abundances of Polycyclic Aromatic Hydrocarbons in Titan's Upper Atmosphere. *Astrophys J* **2013**, *770*.

14. Wilson, E. H.; Atreya, S. K., Chemical Sources of Haze Formation in Titan's Atmosphere. *Planet Space Sci* **2003**, *51*, 1017-1033.

15. Cernicharo, J.; Heras, A. M.; Tielens, A. G. G. M.; Pardo, J. R.; Herpin, F.; Guelin, M.; Waters, L. B. F. M., Infrared Space Observatory's Discovery of C_4H_2, C_6H_2, and Benzene in CRL 618. *Astrophys J* **2001**, *546*, L123-L126.

16. Lovas, F. J.; McMahon, R. J.; Grabow, J. U.; Schnell, M.; Mack, J.; Scott, L. T.; Kuczkowski, R. L., Interstellar Chemistry: A Strategy for Detecting Polycyclic Aromatic Hydrocarbons in Space. *J Am Chem Soc* **2005**, *127*, 4345-4349.

17. Chiar, J. E.; Tielens, A. G. G. M.; Adamson, A. J.; Ricca, A., The Structure, Origin, and Evolution of Interstellar Hydrocarbon Grains. *Astrophys J* **2013**, *770*.

18. Dwek, E., et al., Detection and Characterization of Cold Interstellar Dust and Polycyclic Aromatic Hydrocarbon Emission, from COBE Observations. *Astrophys J* **1997**, *475*, 565-579.

19. Wakelam, V.; Herbst, E., Polycyclic Aromatic Hydrocarbons in Dense Cloud Chemistry. *Astrophys J* **2008**, *680*, 371-383.

20. Kaiser, R. I.; Parker, D. S. N.; Mebel, A. M., Reaction Dynamics in Astrochemistry: Low-Temperature Pathways to Polycyclic Aromatic Hydrocarbons in the Interstellar Medium. *Annu Rev Phys Chem, Vol 66* **2015**, *66*, 43-67.

21. Tielens, A. G. G. M., Interstellar Polycyclic Aromatic Hydrocarbon Molecules. *Annu Rev Astron Astr* **2008**, *46*, 289-337.

22. Tielens, A. G. G. M.; Charnley, S. B., Circumstellar and Interstellar Synthesis of Organic Molecules. *Origins Life Evol B* **1997**, *27*, 23-51.

23. McGuire, B. A.; Burkhardt, A. M.; Kalenskii, S.; Shingledecker, C. N.; Remijan, A. J.; Herbst, E.; McCarthy, M. C., Detection of the Aromatic Molecule Benzonitrile (c-C_6H_5CN) in the Interstellar Medium. *Science* **2018**, *359*, 202-205.

24. Trevitt, A. J.; Goulay, F.; Taatjes, C. A.; Osborn, D. L.; Leone, S. R., Reactions of the CN Radical with Benzene and Toluene: Product Detection and Low-Temperature Kinetics. *J Phys Chem A* **2010**, *114*, 1749-1755.

25. James, P. L.; Sims, I. R.; Smith, I. W. M.; Alexander, M. H.; Yang, M. B., A Combined Experimental and Theoretical Study of Rotational Energy Transfer in Collisions between NO(X $^2\Pi_{1/2}$, v = 3, J) and He, Ar and N_2 at Temperatures Down to 7 K. *J Chem Phys* **1998**, *109*, 3882-3897.

26. Sims, I. R.; Queffelec, J. L.; Defrance, A.; Rebrionrowe, C.; Travers, D.; Bocherel, P.; Rowe, B. R.; Smith, I. W. M., Ultralow Temperature Kinetics of Neutral-Neutral Reactions - the Technique and Results for the Reactions CN+O_2 Down to 13 K and CN+NH_3 Down to 25 K. *J Chem Phys* **1994**, *100*, 4229-4241.

27. Gupta, D.; Ely, S. C. S.; Cooke, I. R.; Guillaume, T.; Khedaoui, O. A.; Hearne, T. S.; Hays, B. M.; Sims, I. R., Low Temperature Kinetics of the Reaction between Methanol and the CN Radical. *J Phys Chem A* **2019**, *123*, 9995-10003.

28. Felps, W. S.; Rupnik, K.; Mcglynn, S. P., Electronic Spectroscopy of the Cyanogen Halides. *J Phys Chem* **1991**, *95*, 639-656.

29. O'Halloran, M. A.; Joswig, H.; Zare, R. N., Alignment of CN from 248 nm Photolysis of ICN - a New Model of the a Continuum Dissociation Dynamics. *J Chem Phys* **1987**, *87*, 303-313.

30. Frisch, M. J., et al. *Gaussian 09*, Gaussian, Inc.: Wallingford, CT, USA, 2009.

31. Kendall, R. A.; Dunning, T. H.; Harrison, R. J., Electron-Affinities of the 1st-Row Atoms Revisited - Systematic Basis-Sets and Wave-Functions. *J Chem Phys* **1992**, *96*, 6796-6806.

32. Woon, D. E.; Dunning, T. H., Gaussian-Basis Sets for Use in Correlated Molecular Calculations 3. The Atoms Aluminum through Argon. *J Chem Phys* **1993**, *98*, 1358-1371.

33. Zhao, Y.; Truhlar, D. G., The M06 Suite of Density Functionals for Main Group Thermochemistry, Thermochemical Kinetics, Noncovalent Interactions, Excited States, and Transition Elements: Two New Functionals and Systematic Testing of Four M06-Class Functionals and 12 Other Functionals. *Theor Chem Acc* **2008**, *120*, 215-241.

34. Lee, K. L. K.; McGuire, B. A.; McCarthy, M. C., Gas-Phase Synthetic Pathways to Benzene and Benzonitrile: A Combined Microwave and Thermochemical Investigation. *Phys Chem Chem Phys* **2019**, *21*, 2946-2956.

35. Nakashima, N.; Yoshihara, K., Laser Photolysis of Benzene - 5. Formation of Hot Benzene. *J Chem Phys* **1982**, *77*, 6040-6050.

36. Koban, W.; Koch, J. D.; Hanson, R. K.; Schulz, C., Absorption and Fluorescence of Toluene Vapor at Elevated Temperatures. *Phys Chem Chem Phys* **2004**, *6*, 2940-2945.

37. Kovacs, T.; Blitz, M. A.; Seakins, P. W.; Pilling, M. J., H Atom Formation from Benzene and Toluene Photoexcitation at 248 nm. *J Chem Phys* **2009**, *131*.

38. Woon, D. E., Modeling Chemical Growth Processes in Titan's Atmosphere: 1. Theoretical Rates for Reactions between Benzene and the Ethynyl (C_2H) and Cyano (CN) Radicals at Low Temperature and Pressure. *Chem Phys* **2006**, *331*, 67-76.

39. Zhang, R. M.; Truhlar, D. G.; Xu, X. F., Kinetics of the Toluene Reaction with OH Radical. *Research-China* **2019**, *2019*.

40. Myer, J. A.; Samson, J. A. R., Vacuum-Ultraviolet Absorption Cross Sections of CO, HCl, and ICN between 1050 and 2100 Å. *J Chem Phys* **1970**, *52*, 266-&.

41. Fally, S.; Carleer, M.; Vandaele, A. C., UV Fourier Transform Absorption Cross Sections of Benzene, Toluene, Meta-, Ortho-, and Para-Xylene. *J Quant Spectrosc Ra* **2009**, *110*, 766-782.

42. Hickman, C. G.; Gascooke, J. R.; Lawrance, W. D., The S_1-S_0($^1B_2$-$^1A_1$) Transition of Jet-Cooled Toluene: Excitation and Dispersed Fluorescence Spectra, Fluorescence Lifetimes, and Intramolecular Vibrational Energy Redistribution. *J Chem Phys* **1996**, *104*, 4887-4901.

43. Zimmermann, F. P.; Koban, W.; Roth, C. M.; Herten, D. P.; Schulz, C., Fluorescence Lifetime of Gas-Phase Toluene at Elevated Temperatures. *Chem Phys Lett* **2006**, *426*, 248-251.

44. Lu, K. T.; Eiden, G. C.; Weisshaar, J. C., Toluene Cation - Nearly Free Rotation of the Methyl-Group. *J Phys Chem* **1992**, *96*, 9742-9748.

45. Henis, N. B. H.; Miller, L. L., Mechanism of Gas-Phase Cyanation of Alkenes and Aromatics. *J Am Chem Soc* **1983**, *105*, 2820-2823.

46. Rudolph, H. D.; Dreizler, H.; Jaeschke, A.; Wendling, P., Mikrowellenspektrum Hinderungspotential Der Internen Rotation Und Dipolmoment Des Toluols. *Z Naturforsch Pt A* **1967**, *A 22*, 940-&.

47. Loomis, R. A., et al., Non-Detection of $HC_{11}N$ Towards TMC-1: Constraining the Chemistry of Large Carbon-Chain Molecules. *Mon Not R Astron Soc* **2016**, *463*, 4175-4183.

48. Walsh, C.; Loomis, R. A.; Oberg, K. I.; Kama, M.; van't Hoff, M. L. R.; Millar, T. J.; Aikawa, Y.; Herbst, E.; Weaver, S. L. W.; Nomura, H., First Detection of Gas-Phase Methanol in a Protoplanetary Disk. *Astrophys J Lett* **2016**, *823*.

49. Langston, G.; Turner, B., Detection of ^{13}C Isotopomers of the Molecule HC_7N. *Astrophys J* **2007**, *658*, 455-461.

50. Douberly, G. E.; Ricks, A. M.; Schleyer, P. V. R.; Duncan, M. A., Infrared Spectroscopy of Gas Phase Benzenium Ions: Protonated Benzene and Protonated Toluene, from 750 to 3400 cm^{-1}. *J Phys Chem A* **2008**, *112*, 4869-4874.

51. Joblin, C.; Tielens, A. G. G. M.; Allamandola, L. J.; Geballe, T. R., Spatial Variation of the 3.29 and 3.40 Micron Emission Bands within Reflection Nebulae and the Photochemical Evolution of Methylated Polycyclic Aromatic Hydrocarbons. *Astrophys J* **1996**, *458*, 610-620.

52. Wagner, D. R.; Kim, H. S.; Saykally, R. J., Peripherally Hydrogenated Neutral Polycyclic Aromatic Hydrocarbons as Carriers of the 3 Micron Interstellar Infrared Emission Complex: Results from Single-Photon Infrared Emission Spectroscopy. *Astrophys J* **2000**, *545*, 854-860.

53. Dangi, B. B.; Parker, D. S.; Kaiser, R. I.; Jamal, A.; Mebel, A. M., A Combined Experimental and Theoretical Study on the Gas-Phase Synthesis of Toluene under Single Collision Conditions. *Angew Chem Int Ed Engl* **2013**, *52*, 7186-9.

54. Jones, B. M.; Zhang, F. T.; Kaiser, R. I.; Jamal, A.; Mebel, A. M.; Cordiner, M. A.; Charnley, S. B., Formation of Benzene in the Interstellar Medium. *P Natl Acad Sci USA* **2011**, *108*, 452-457.

55. Wakelam, V., et al., A Kinetic Database for Astrochemistry (KIDA). *Astrophys J Suppl S* **2012**, *199*.

56. Lockyear, J. F.; Fournier, M.; Sims, I. R.; Guillemin, J. C.; Taatjes, C. A.; Osborn, D. L.; Leone, S. R., Formation of Fulvene in the Reaction of C_2H with 1,3-Butadiene. *Int J Mass Spectrom* **2015**, *378*, 232-245.

57. Abeysekera, C.; Joalland, B.; Ariyasingha, N.; Zack, L. N.; Sims, I. R.; Field, R. W.; Suits, A. G., Product Branching in the Low Temperature Reaction of CN with Propyne by Chirped-Pulse Microwave Spectroscopy in a Uniform Supersonic Flow. *J Phys Chem Lett* **2015**, *6*, 1599-1604.

58. Hays, B. M.; Guillaume, T.; Hearne, T. S.; Cooke, I. R.; Gupta, D.; Abdelkdaer Khedaoui, O.; Le Picard, S. D.; Sims, I. R., Design and Performance of an E-Band Chirped Pulse Spectrometer for Kinetics Applications: OCS - He Pressure Broadening. *J Quant Spectrosc Ra* **2020**, *250*.

Chapter 5 – Acceleration of the OH + CO Reaction at Low Temperatures: Measurements of the OH (v = 0, 1) + CO Rate Constant Down to 30 K

5.1 – Abstract

The reaction between OH and CO to form H and CO_2 is important in a wide variety of systems, including atmospheric and combustion chemistry, but is complicated by a number of intermediates, including *cis*- and *trans*-HOCO and a prereactive hydrogen-bonded complex. Inspired by the high abundance of these molecules in the interstellar medium and the recent discovery of similar reactions becoming faster at low (< 100 K) temperatures, we have used the CRESU technique combined with PLP-LIF to study this rate constant down to 30 K, providing the first measurements below 80 K. Additionally, we have studied the OH (v = 1) + CO reaction, which serves as a proxy for the high-pressure termolecular rate constant of the OH (v = 0) + CO reaction, also down to 30 K. We find that the two rate constants converge at low temperatures, reaching a minimum at ~55 K, before increasing at lower temperatures. This minimum and turnaround is explained through semiclassical transition state calculations, which suggest that they are due to tunneling of the prereactive hydrogen-bonded complex to products, and competition between this and the dissociation pathway of the hydrogen-bonded complex.

5.2 – Introduction

One of the most important reactions in both atmospheric and combustion chemistry is the reaction between OH and CO

$OH + CO \rightarrow H + CO_2$ (R5.1)

In Earth's atmosphere, this reaction is a key component in the HO_x ($HO_x = OH + HO_2$) cycle, as the atomic H produced reacts immediately with O_2 to form HO_2.

$H + O_2 + M \rightarrow HO_2 + M$ (R5.2)

The cycling of HO_x is key in understanding the oxidation processes in the atmosphere. The CO is produced from the oxidation of methane or the breakdown of larger hydrocarbons, or through anthropogenic emissions from incomplete combustion chemistry.

In combustion chemistry, on the other hand, this reaction is the final oxidation step, where the CO produced from the breakdown and oxidation of starting materials (fuels, such as propane or butane) is converted into the stable CO_2 that is ultimately emitted through the exhaust. Furthermore, it is this reaction that releases the majority of heat during combustion.[1] With the focus on decreasing CO_2 emissions into the atmosphere due to its importance in global warming and climate change, this reaction has been studied extensively at higher temperatures (up to 2500 K).

The previous measurements of this rate constant show that despite this reaction only involving four atoms, its dynamics are complex, leading to unusual temperature and pressure dependencies. At low pressures and room temperature (298 K), the rate constant remains constant, with a value on the order of 1×10^{-13} cm^3 s^{-1}, but as the density increases and approaches 1×10^{19} cm^{-3}, the rate increases to 2×10^{-13} cm^3 s^{-1}. At even higher densities, which have been measured up to 10^{22} cm^{-3} using a He buffer gas, the rate constant increases to 1×10^{-12} cm^3 s^{-1}.[2] The high-pressure limit, however, is difficult to experimentally measure, and even at the highest pressures studied, the rate constant continues to increase. While this pressure dependence suggests a termolecular component to the reaction, the reaction's behavior suggests that it is more complicated than a third-body stabilization of the product, as in other termolecular reactions. The rate constant of ~1-2 × 10^{-13} cm^3 s^{-1} is constant over the 80 – 500 K range, before beginning to increase at higher temperatures.[2] Both the temperature and pressure dependencies of this reaction were recently evaluated and compared to results from semiclassical transition state theory by Barker et al.[3]

This unusual behavior is explained by the potential energy surface (PES) of the reaction, which shows that this reaction proceeds through multiple intermediates, as seen in Figure 5.1. The reactants initially form a weakly bound hydrogen-bonded complex (OH-CO), before passing over a small barrier to form the *trans*-HOCO intermediate, which can then proceed to isomerize through two different channels before forming the H + CO_2 products.

The unusual pressure dependence originates from competition between a termolecular reaction resulting in the stabilization of the HOCO radicals, and a chemically activated bimolecular reaction which forms H and CO_2. At low pressures, the bimolecular channel dominates, but more HOCO is stabilized as the pressure increases. Currently, the JPL Data Evaluation parameterizes this reaction by using the sum of the chemically activated bimolecular and the termolecular rate constants.[5]

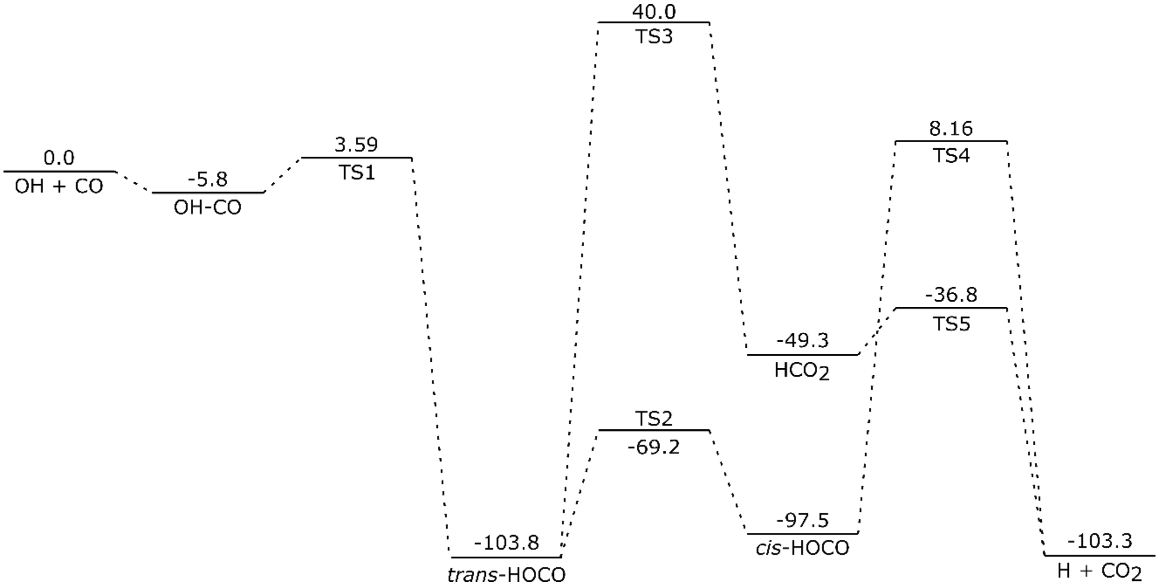

Figure 5.1: Potential energy surface of the OH + CO reaction (in kJ/mol), using the values calculated by the HEAT (High accuracy extrapolated *ab initio* thermochemistry) protocol in Nguyen et al.[4]

The HOCO intermediates were first proposed in the 1970s,[6-7] but were not directly detected from this reaction under thermal conditions until Bjork et al. in 2016, who used time resolved mid-infrared frequency comb spectroscopy to detect the *trans*-DOCO formed from OD + CO.[8] The *cis*-HOCO isomer was later directly detected using the same method in Bui et al.[9] The OH-CO hydrogen-bonded complex was suggested to play a role in the reaction from experiments down to 80 K,[10] which is to date the lowest temperature where rate constants have been measured. It has not been directly observed from this reaction, but its dynamics and stability have been studied extensively using infrared OH action spectroscopy.[11-13] These experimental values give an upper limit of 410 cm^{-1} (4.9 kJ/mol) for the dissociation energy[11], in contrast with the 5.8 kJ/mol determined from *ab initio* calculations.[4]

While experimental measurements have shown the difficulties in reaching the high-pressure limit rate constant for this reaction, it has been argued by Ian Smith and coworkers that studying the rate constant of the reaction of vibrationally excited OH, OH (v = 1), with CO can be used as a proxy of the high pressure rate constant.[14] While the additional energy in the OH stretch is separated from the reaction coordinate and thus can not be used to proceed over TS1, if the OH (v = 1) and CO are able to overcome the barrier and result in HOCO product formation, the energy in the OH stretch will be scrambled throughout the HOCO molecules before it dissociates back to reactants, stabilizes, or proceeds to H + CO_2 products. In this way, measuring the OH (v = 1) + CO rate constant is a measurement of the rate of HOCO formation, which is equivalent to measuring the rate of the high-pressure rate constant, where only HOCO is formed, as it is the initial formation of the energetically excited HOCO that is the rate limiting step.

Thus, by monitoring OH (v = 1), the high-pressure rate constant of OH (v = 0) + CO can be determined. Previous work has demonstrated that OH (v > 0) + CO rate constants are larger than OH (v = 0), though the rate constants for OH (v = 1 – 4) + CO do not show a significant change.[15]

OH and CO are both abundant in the interstellar medium (ISM). CO is the second most common molecule throughout the ISM, with only H_2 being more abundant,[16] and is a widely used tracer for the presence of molecular clouds. In the Taurus Molecular Cloud-1 (TMC-1), CO has a fractional abundance of 10^{-4} relative to H_2,[17] while OH's fractional abundance is 10^{-7}.[18]

The possible products of this reaction are also of astrochemical interest. HOCO has not been detected in the gas or solid phases in the ISM, but it has been suggested that HOCO is a precursor that leads to the formation of glycine, the simplest amino acid, in the ISM.[19] CO_2 is ubiquitous in the ISM, with high abundances in ices but low abundances in the gas phase.[20] However, its origins are still debated and cannot be fully explained by gas phase mechanisms alone.[20-21] The surface reaction of OH and CO on ices is believed to be important in its formation.[22]

As discussed in Chapter 1, previous studies of low temperature (< 100 K) reactions has demonstrated that some reactions reach a minimum as the temperature decreases, before increasing in rate at colder temperatures, due to the presence of prereactive hydrogen-bonded complexes. Due to the complicated PES of the OH + CO reaction suggesting that this reaction may also exhibit a rate turnaround at low temperatures, as well as their abundance in the ISM, we have studied the rate constant of this reaction down to 30 K, including measurements at different densities at 38 and 55 K. Furthermore, to determine any pressure dependencies of this reaction at low temperatures, we have also studied the reaction of OH (v = 1) + CO down to 30 K.

5.3 – Experimental Methods

Rate constants were measured using the pulsed laser photolysis-laser induced fluorescence (PLP-LIF) method in conjunction with the CRESU technique, as described previously[23-25] and in Chapter 2. Nitrogen passes through a bubbler containing 60% H_2O_2 solution (Arkema), and is mixed with a continuous flow of N_2 (99.995%, Air Liquide) and CO (99%, Air Liquide). This mix was cooled down to 30 K in an N_2 buffer gas using the CRESU technique. Briefly, a gas flow containing the reactant, CO, and radical precursor, H_2O_2, are isentropically expanded through a specially designed convergent-divergent Laval nozzle from a high-pressure reservoir into a low-pressure chamber to generate a uniform supersonic flow at the appropriate temperature with a density of $10^{16} – 10^{17}$ cm^{-3}.

Each nozzle is characterized by Pitot impact measurements prior to experiments, in order to determine the temperature, pressure and density, of the supersonic flow.

In typical CRESU experiments, concentrations of precursors and reactants are limited to < 1% of the total flow to not disrupt the flow. However, N_2 and CO are aerodynamically equivalent due to the similarities in their masses, viscosities, and heat capacity ratios, allowing us to go to much higher concentrations of CO. As seen in Figure 5.2, CRESU flows at 30 K show no difference between 100% N_2 gas flow and 50% N_2/50% CO gas flow. No signs of N_2 or CO clustering were observed in Pitot measurements down to 30 K, which would be observed as a loss of uniformity in the supersonic flow. Additional experiments used the structured LIF spectrum of the CN radical to confirm that high concentrations of CO did not affect the temperature of the flow at 38 K, using the CN generation method described in Chapter 2. The time-dependent signal of the CN radical did not change as a function of [CO], indicating that no reaction between CN and CO was occurring. The spectrum was fit with the PGOPHER program to determine the rotational temperature of CN.[26] Again, the results found no change in the temperature of the CRESU flow as the [CO] was increased.

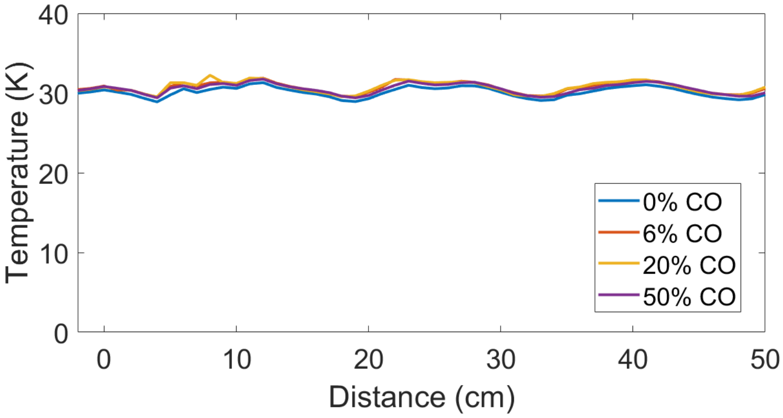

Figure 5.2: The temperatures of the 30 K nozzle, as measured by Pitot impact test measurements, at CO concentrations ranging from 0% – 50% of the total flow. No discernable change can be observed as a function of CO concentration.

OH radicals are generated by a 10 Hz excimer laser firing at 248 and 193 nm to photolyze H_2O_2, in order to form the ground and first excited vibrational states, respectively. The laser fluences at 248 and 193 nm are 31.2 and 39.5 mJ/cm^2, respectively. The second harmonic of a 10 Hz Nd:YAG laser is used to excite a dye laser containing either rhodamine 6G (for OH v = 0) or a mix of rhodamine 6G and B (for v = 1), the output of which is sent through BBO doubling crystals to produce ~1 mJ of UV light to excite the OH radicals. The (1,0) and (2,1) bands of the $A^2\Sigma^+ \leftarrow X^2\Pi$ electronic transition are used to excite the OH (v = 0) and OH (v = 1) radicals, respectively, at ~282 and ~289 nm. The resulting fluorescence is detected by a photomultiplier tube proceeded by either a 310 nm (for OH v = 0) or 320 nm (for OH v = 1) bandpass filter. The delay between the excimer and the Nd:YAG is varied from -5 – hundreds of microseconds to record the OH signal over a series of 400 evenly-spaced points, and is averaged 7-10 times to obtain the decay trace. The length of the decay is limited by the hydrodynamic time of the uniform flow of any particular nozzle. The decay is fit after 10 – 20 μs after photolysis in order to allow for rotational thermalization of the OH radical.

Kinetic measurements were taken under pseudo-first order conditions, with [CO] >> [OH]; typical CO concentrations varied from $10^{15} – 10^{16}$ cm^{-3}. We estimate [OH (v = 0)] to be ~2×10^{11} cm^{-3}, based on the typical H_2O_2 concentration of ~2.7×10^{13} cm^{-3} in experiments and the H_2O_2 cross sections at 248 nm (8.92×10^{-20} cm^2, OH quantum yield of 2.09 ± 0.36).[27-28] No evidence for vibrational excitation of OH produced from the 248 nm photolysis of H_2O_2 has been observed.[28-29]

The branching fraction of OH (v = 1) from the 193 nm photolysis of H_2O_2 has not been experimentally measured; Ondrey et al. and Vaghjiani et al. estimate the upper limit to be 5 – 15% of the total OH produced.[29-30] Based on this upper limit and the 193 nm cross section of H_2O_2 (58.9×10^{-20} cm^2, OH quantum yield 1.51 ± 0.18),[27,30] we estimate the upper limit of [OH (v = 1)] to be ~9×10^{10} cm^{-3} in our experiments.

5.4 – Theoretical Methods

Theoretical calculations were conducted by our collaborator John Barker, in collaboration with John Stanton and Lam Nguyen. They have previously calculated a high quality PES of this reaction and used it to calculate rate constants over the 100 – 2000 K range[3-4] and extended this analysis to 5 K for comparison to our experimental measurements.

The *ab initio* PES of the reaction was determined with the HEAT protocol which has been shown to produce energies accurate to < 1 kJ/mol,[31-34] with the resulting energies shown in Figure 5.1. As discussed above, experimental measurements of OH-CO complex give it a dissociation energy of 410 cm^{-1} (4.9 kJ/mol),[11] in contrast with the 5.8 kJ/mol determined with the HEAT method. At the low temperatures used in this work, the rate constants from using the experimental dissociation energy and the HEAT dissociation energy differ by roughly 15%, with the rate constants using the experimental value being faster. Here we report rate constants determined using the experimental 4.9 kJ/mol for the OH-CO hydrogen-bonded complex.

After determination of the PES, semi-classical transition state theory (SC-TST) was used to calculate the low- and high-pressure limit rate constants of the reaction. SC-TST is an extension of classical TST, which calculates the number of reactants that are able to overcome the activation energy to form products, based on the partition functions and energies of the reactants and transition state. SC-TST incorporates quantum mechanical effects, including tunneling effects, into the TST calculations, and is a computationally inexpensive method to determine rate constants theoretically.[35] Details of the HEAT and SC-TST calculations on the OH + CO reaction have been published previously.[3-4,36]

5.5 – Experimental Results

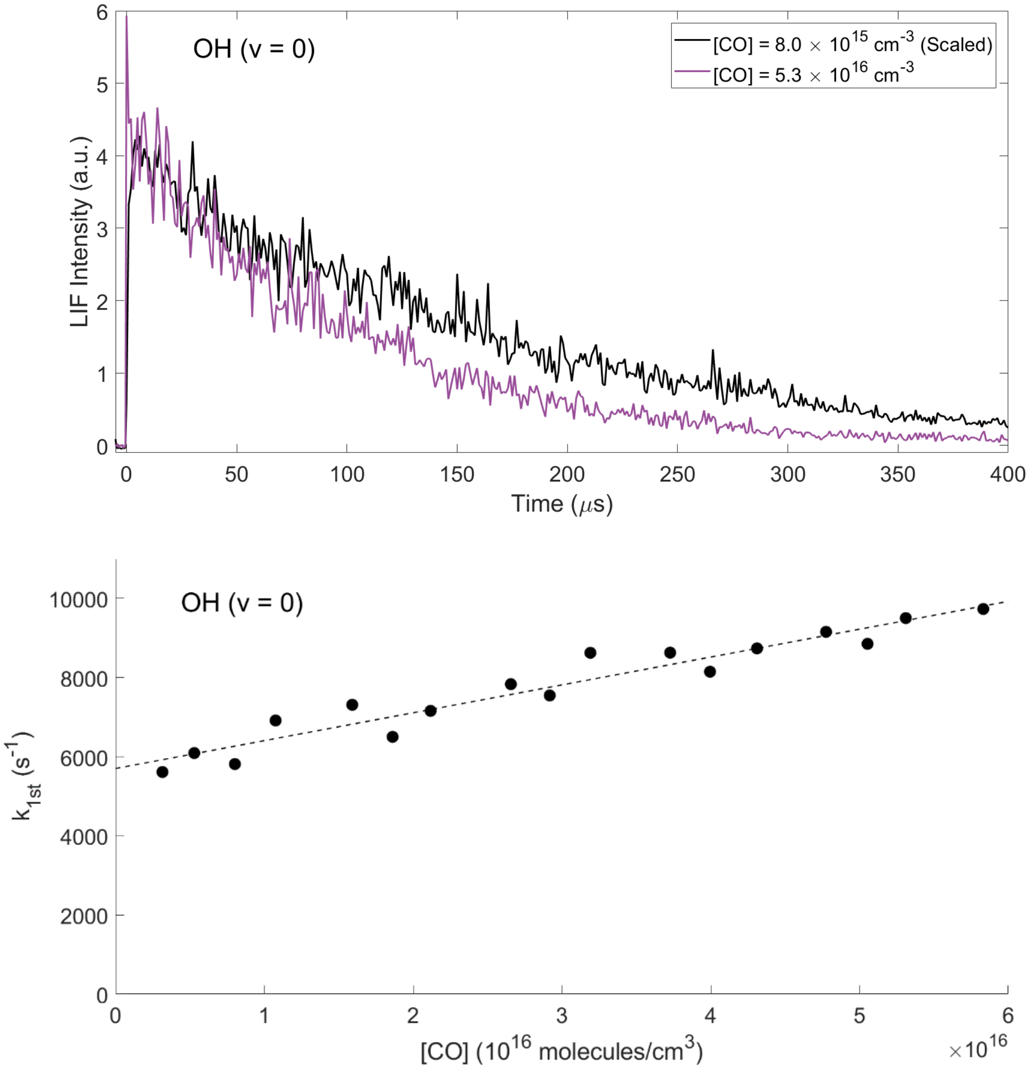

Figure 5.3: The decay of the OH (v = 0) for two different CO concentrations at 55 K (top), and the resulting second-order plot (bottom).

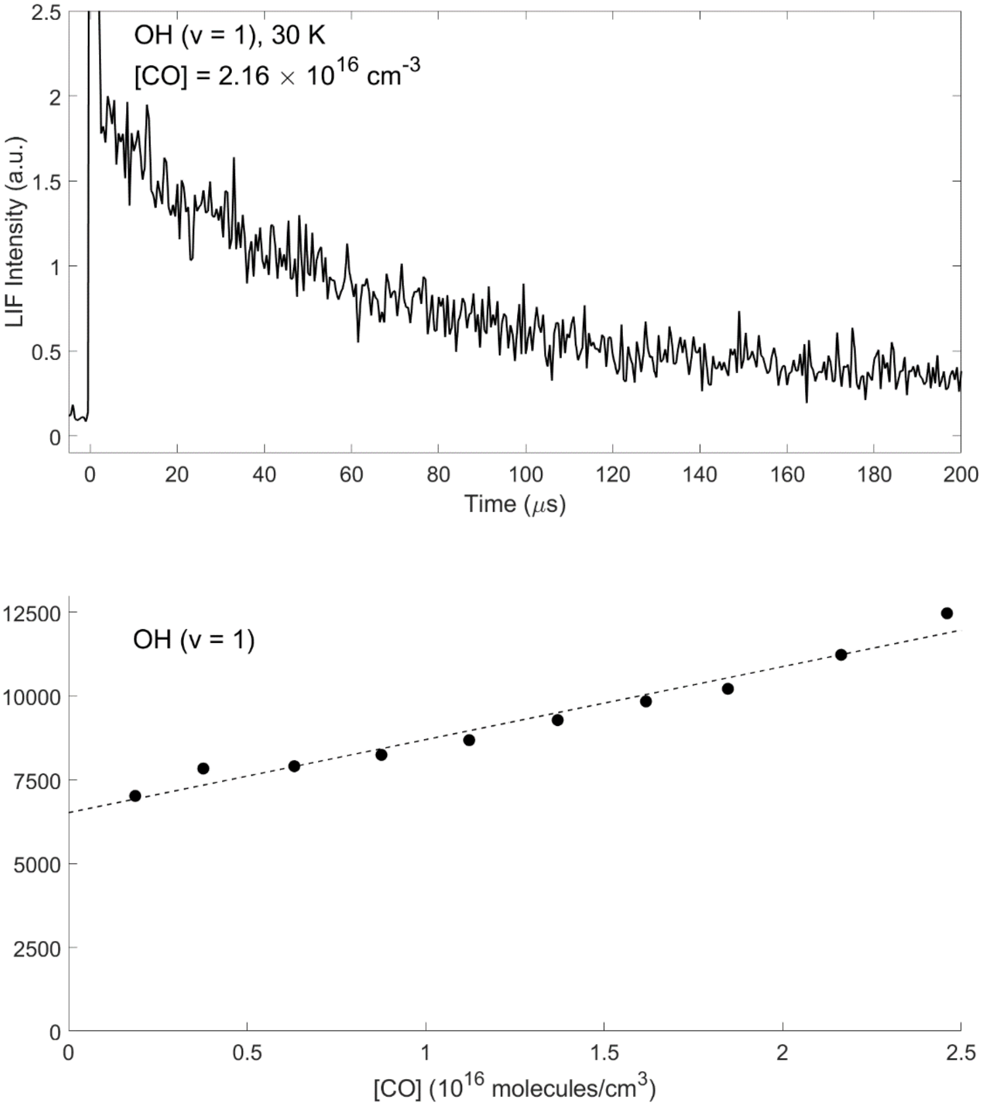

Figure 5.4: The decay of the OH (v = 1) at 30 K (top), and the resulting second-order plot (bottom).

A typical OH decay and the resulting second-order plot for OH (v = 0) and OH (v = 1) can be seen in Figures 5.3 and 5.4, respectively. The non-zero intercept on the second-order plot results from diffusion of the OH out of the region probed by LIF and from secondary chemistry resulting in OH loss. The H_2O_2 concentration and excimer laser power are kept constant for each measurement in order to prevent this secondary chemistry, such as OH + H_2O_2 and reactions of OH with other photolysis products, from interfering with our measurements of $k_{OH + CO}$, as they will only affect the intercept on the second-order plot. We see no evidence of non-linearities in our second-order plots at high [CO], which is further evidence that CO is not clustering under our experimental conditions.

Rate constants for the OH (v = 0) + CO and OH (v = 1) + CO reactions can be seen in Tables 5.1 and 5.2, respectively, and Figure 5.5. Between 8 and 17 points at varying [CO] are taken for each measurement, in addition to points taken at the same [CO] to examine the reproducibility of the data. Measurements are taken at two densities at both 38 and 55 K to determine what effect this has on the rate constants. The v = 1 measurements display no dependence on pressure, while the results for v = 0 may display a slight dependence on pressure, but the rate coefficients fall within the experimental error. Room temperature measurements also demonstrate no pressure dependence for the v = 1 reaction; the pressure dependence of v = 0 at room temperature is well-characterized and summarized by the JPL and IUPAC data evaluations.

Table 5.1: Rate coefficients determined for the OH (v = 0) + CO reaction between 30 and 295 K, along with experimental parameters for each measurement. Uncertainties in the rate constant are the 95% confidence interval from the appropriate Student's *t* test combined in quadrature with a 10% systematic error.

Temperature (K)	Density (10^{16} cm^{-3})	[CO] range (10^{16} cm^{-3})	Number of points	$k_{OH (v = 0) + CO}$ (10^{-13} cm^3 s^{-1})
30	3.73	0.95 – 2.51	15	2.11 ± 0.37
38	3.28	0.15 – 1.97	13	0.91 ± 0.15
38	6.92	1.70 – 4.55	16	1.13 ± 0.21
55	7.06	0.32 – 5.83	17	0.70 ± 0.13
55	9.65	0.64 – 5.11	17	0.81 ± 0.19
83	4.73	0.13 – 2.22	11	1.05 ± 0.20
200	5.27	0.17 – 2.54	10	1.46 ± 0.26
295	9.50	1.44 – 7.60	11	1.44 ± 0.16

Table 5.2: Rate coefficients determined for the OH (v = 1) + CO reaction between 30 and 294 K, along with experimental parameters for each measurement. Uncertainties in the rate constant are the 95% confidence interval from the appropriate Student's *t* test combined in quadrature with a 10% systematic error. Bolded values represent the weighted average and uncertainty for temperatures with multiple measurements.

Temperature (K)	Density (10^{16} cm^{-3})	[CO] range (10^{16} cm^{-3})	Number of points	$k_{\mathrm{OH\ (v = 1) + CO}}$ (10^{-13} cm^3 s^{-1})
30	3.73	0.19 – 2.46	10	2.17 ± 0.40
38	3.28	0.15 – 1.80	12	1.30 ± 0.49
38	6.92	0.46 – 4.04	9	1.30 ± 0.45
				1.30 ± 0.11
55	7.05	0.45 – 4.28	10	1.09 ± 0.20
55	9.65	0.84 – 4.28	9	1.07 ± 0.33
				1.08 ± 0.03
83	4.72	0.22 – 1.98	9	1.93 ± 0.75
200	5.33	0.54 – 2.14	8	3.96 ± 1.20
294	4.50	0.67 – 2.01	11	7.62 ± 1.71
294	8.94	1.36 – 2.66	11	6.00 ± 1.94
294	14.50	0.26 – 2.81	13	6.37 ± 1.24
				6.63 ± 0.79

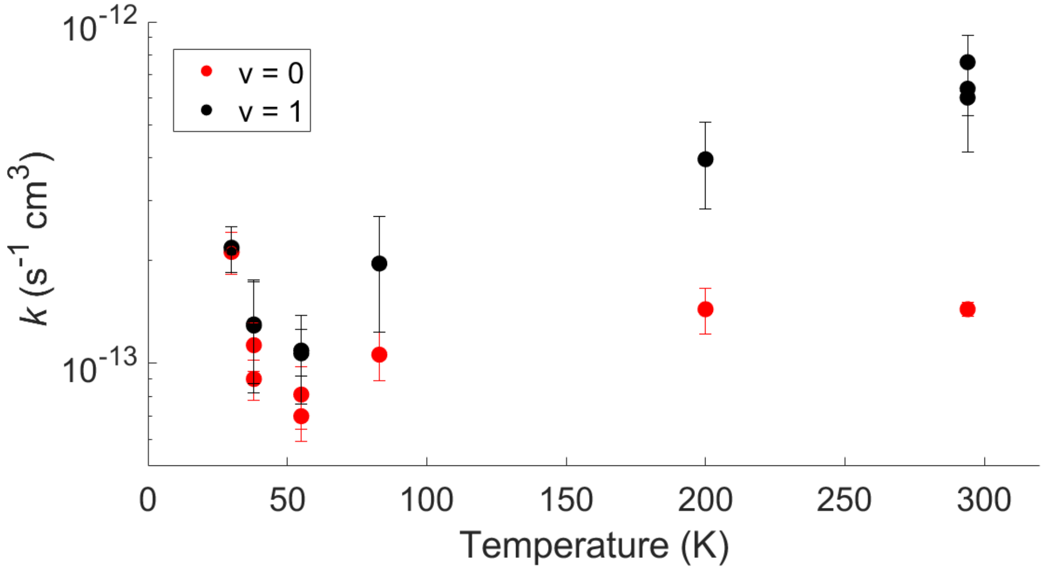

Figure 5.5: The temperature dependent rate constants of the OH (v = 0) + CO reaction (red) and the OH (v = 1) + CO reaction (black) over the 30 – 295 K range.

5.6 – Theoretical Results

The preliminary results of the SC-TST calculations by John Barker of the low-pressure limit rate constant for the OH (v = 0) + CO reaction are shown in Figure 5.6. Work on the high-pressure limit rate constants and refinement of the low-pressure limit rate constants is ongoing. Like the experimental measurements, the calculated rate constants clearly display a minimum, here located at 30 K, before increasing at lower temperatures. The calculated rate constants underestimate the experimental measurements by a factor of 2 to 5, however. It is worth noting that previous calculations using SC-TST by Barker et al. showed that the low-pressure rate constant does not change with density up to 10^{18} cm^{-3} at 100 K,[3] which suggests our results are in the low-pressure limit and the difference is not due to the densities of the nozzles.

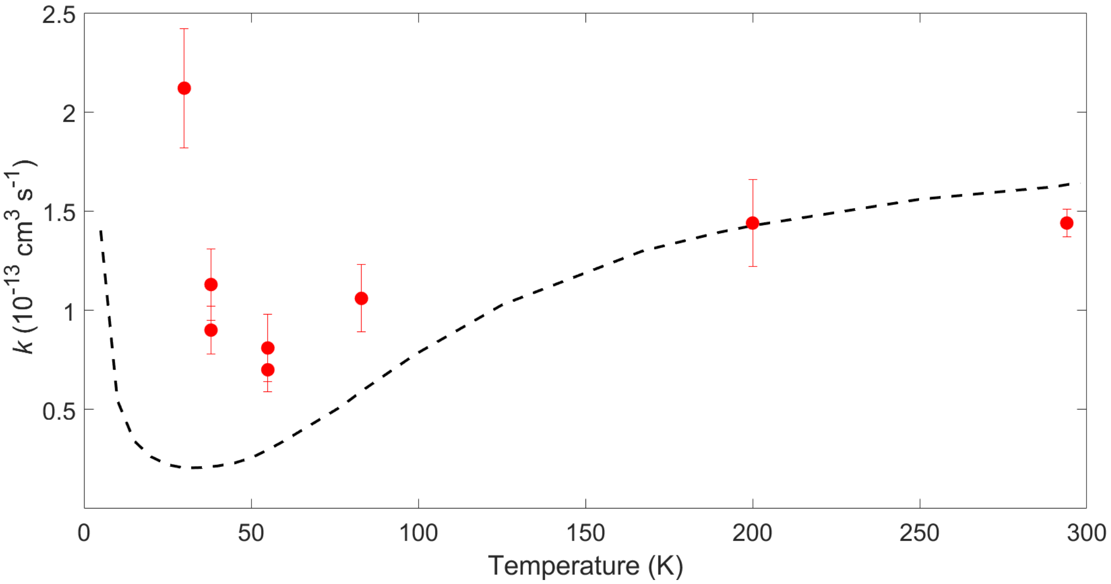

Figure 5.6: The rates of the OH (v = 0) + CO reaction measured in this work (red), as compared to the preliminary SC-TST calculations of the low-pressure limit rate constant (dashed black line).

Because the theoretical calculations are in qualitative agreement with our experimental measurements, we can use the results from the calculations to inform us of the dynamics at play at low temperatures. This work indicates that these cold temperatures, the OH + CO proceeds through formation of the hydrogen-bonded OH-CO complex. The OH-CO complex does not become collisionally stabilized, leading it to remain thermally hot. The complex can either dissociate back to the reactants, or proceed to form HOCO via tunneling through TS1, which is 9.4 kJ/mol above the complex in energy.[4] The energy that remains in the complex allows this tunneling mechanism to proceed, where it would not be able to if it was collisionally stabilized. Like the hydrogen-bonded complex, the HOCO and HCO_2 intermediates are also not collisionally stabilized, and the products of this reaction are H and CO_2. While TS3 and TS4 are higher in energy than the reactants, it has previously been shown that H-atom tunneling plays an important role in the dissociation of the intermediates to form H and CO_2.[4]

The minimum in the rate constants and subsequent turnaround are explained through the competing fates of the hydrogen-bonded OH-CO complex, either through dissociation to reform the OH + CO reactants, or through tunneling to form the H + CO_2 products. The calculations indicate that the rates of these processes have different energy dependencies, and as the available energy changes as the temperature decreases, the fraction of the OH-CO complex that proceeds to react becomes less favorable until it reaches the minimum, after which this becomes more favorable. Further investigation into these different energy dependencies and the rate constant minimum is ongoing.

5.7 – Discussion

The rate constants for the OH ($v = 0$) + CO reaction at higher temperatures are in good agreement with the literature. At the 80 K measurements, Frost et al. measured the rate to be $(1.0 \pm 0.1) \times 10^{-13}$ cm^3 s^{-1},[10] which agrees with our rate of $1.05 \pm 0.20 \times 10^{-13}$ cm^3

s^{-1}. Using the values from the JPL data evaluation,[5] which give values of 1.49 × 10^{-13} cm^3 s^{-1} at the appropriate densities at both 200 and 295 K, agrees with our values of (1.46 ± 0.26) × 10^{-13} cm^3 s^{-1} at 200 K and (1.44 ± 0.16) × 10^{-13} cm^3 s^{-1} at 295 K.

The rate constant for the OH (v = 1) + CO rate constant at room temperature, however, is lower than literature values; Kohno et al. measured it to be (10.8 ± 0.6) × 10^{-13} cm^3 s^{-1},[15] and Brunning et al. measured it to be (10 ± 0.2) × 10^{-13} cm^3 s^{-1}.[14] The weighted average of our measurements, on the other hand, are (6.63 ± 0.62) × 10^{-13} cm^3 s^{-1}. It is worth noting that the recent theoretical calculations from Barker et al. are unable to replicate the 10 × 10^{-13} cm^3 s^{-1} rate constant at the high-pressure limit at 298 K, and instead give a value of roughly 8 × 10^{-13} cm^3 s^{-1}.[3]

The convergence between the low- and high-pressure limit rate constants, however, is predicted by the calculations of Barker et al., who observe a similar trend at 100 K. Experimental measurements from Fulle et al. at 100 K do not show this trend,[2] but the disagreement between the high-pressure rate constants from Barker et al. and Fulle et al. has not been resolved. The work done here clearly aligns with the SC-TST results at low temperatures. Further low temperature experiments, both of the OH (v = 1) + CO rate constant and of OH (v = 0) + CO at high densities, would assist in resolving this discrepancy. The lack of pressure dependence on the rate constant suggests that the reaction is in the bimolecular regime at all pressures at cold temperatures, which is in line with the calculations indicating that H and CO_2 are the dominant products.

While other rate constants have been shown to reach a minimum before increasing in rate at lower temperatures, these reactions are all hydrogen-abstraction reactions, like OH + CH_3OH[37] and CN + C_2H_6,[38] where the hydrogen atom tunnels through the barrier to form products. This work demonstrates that this tunneling mechanism and subsequent increase in rate constant at low temperatures can also occur for other reactions, due to the lack of collisional stabilization at low temperatures. This therefore opens the possibility for other reactions occurring through similar mechanisms.

The rate constants measured here suggest that the OH + CO reaction may play a larger role in the ISM than currently thought. Extrapolation of the our measurements to 10 K, the most used temperature in models of molecular clouds, gives a value of ~10^{-12} cm^3 s^{-1}, but current models, such as the Kinetic Database for Astrochemistry[39] (KIDA, kida.obs.u-bordeaux1.fr, accessed November 2020) give a value of 6.4×10^{-21} cm^3 s^{-1}, meaning the rate constant in models is off by more than 10^8 and these values should be implemented into databases. However, to confirm whether this updated rate constant actually influences chemistry in the ISM, lower temperature measurements of the reaction to better determine the rate at 10 K, and modeling of the impact of updated rate constant on the ISM are necessary.

5.8 – Conclusion

The rate constants of the reaction of the OH (v = 0, 1) + CO reactions have been determined over the 30 – 295 K range. The results show a convergence of the low-pressure rate constants, from the OH (v = 0) + CO reaction, and the high-pressure rate constants, as determined by the OH (v = 1) + CO measurements through the proxy method, which agrees with recently published SC-TST calculations. This indicates that this reaction is likely in the bimolecular regime at low temperatures and is forming H + CO_2 products. The results also show a minimum at 55 K before increasing at lower temperatures, which suggests that tunneling through the barrier may play a role in this reaction at low temperatures. This is confirmed by preliminary SC-TST calculations performed by collaborators, which observe a similar turnaround and suggest that this is due to the competing fates of the prereactive OH-CO hydrogen-bonded complex, which can dissociate back to reactants or proceed through tunneling to result in H + CO_2 formation.

5.9 – References

1. Miller, J. A.; Kee, R. J.; Westbrook, C. K., Chemical-Kinetics and Combustion Modeling. *Annu Rev Phys Chem* **1990**, *41*, 345-387.

2. Fulle, D.; Hamann, H. F.; Hippler, H.; Troe, J., High Pressure Range of Addition Reactions of HO - 2. Temperature and Pressure Dependence of the Reaction HO + CO ↔ HOCO → H+CO_2. *J Chem Phys* **1996**, *105*, 983-1000.

3. Barker, J. R.; Stanton, J. F.; Nguyen, T. L., Semiclassical Transition State Theory/Master Equation Kinetics of HO + CO: Performance Evaluation. *Int J Chem Kinet* **2020**.

4. Nguyen, T. L.; Xue, B. C.; Weston, R. E.; Barker, J. R.; Stanton, J. F., Reaction of HO with CO: Tunneling Is Indeed Important. *J Phys Chem Lett* **2012**, *3*, 1549-1553.

5. Burkholder, J. B., et al., "Chemical Kinetics and Photochemical Data for Use in Atmospheric Studies, Evaluation No. 19" Jpl Publications 19-5, Jet Propulsion Laboratory, Pasadena, 2019 http://jpldataeval.jpl.nasa.gov Publications, J., Ed. 2019.

6. Smith, I. W. M.; Zellner, R., Rate Measurements of Reactions of OH by Resonance-Absorption - 2. Reactions of OH with CO, C_2H_4 and C_2H_2. *J Chem Soc Farad T 2* **1973**, *69*, 1617-&.

7. Smith, I. W. M., Mechanism of OH + CO Reaction and Stability of HOCO Radical. *Chem Phys Lett* **1977**, *49*, 112-115.

8. Bjork, B. J., et al., Direct Frequency Comb Measurement of OD + CO → DOCO Kinetics. *Science* **2016**, *354*, 444-448.

9. Bui, T. Q.; Bjork, B. J.; Changala, P. B.; Nguyen, T. L.; Stanton, J. F.; Okumura, M.; Ye, J., Direct Measurements of DOCO Isomers in the Kinetics of OD. *Sci Adv* **2018**, *4*.

10. Frost, M. J.; Sharkey, P.; Smith, I. W. M., Reaction between OH (OD) Radicals and CO at Temperatures Down to 80 K - Experiment and Theory. *J Phys Chem* **1993**, *97*, 12254-12259.

11. Pond, B. V.; Lester, M. I., Decay Dynamics of the Vibrationally Activated OH-CO Reactant Complex. *J Chem Phys* **2003**, *118*, 2223-2234.

12. Lester, M. I.; Pond, B. V.; Marshall, M. D.; Anderson, D. T.; Harding, L. B.; Wagner, A. F., Mapping the OH+CO → HOCO Reaction Pathway through IR Spectroscopy of the OH-CO Reactant Complex. *Faraday Discuss* **2001**, *118*, 373-385.

13. Lester, M. I.; Pond, B. V.; Anderson, D. T.; Harding, L. B.; Wagner, A. F., Exploring the OH + CO Reaction Coordinate Via Infrared Spectroscopy of the OH-CO Reactant Complex. *J Chem Phys* **2000**, *113*, 9889-9892.

14. Brunning, J.; Derbyshire, D. W.; Smith, I. W. M.; Williams, M. D., Kinetics of OH (v = 0, 1) and OD (v = 0, 1) with CO and the Mechanism of the OH + CO Reaction. *J Chem Soc Farad T 2* **1988**, *84*, 105-119.

15. Kohno, N.; Izumi, M.; Kohguchi, H.; Yamasaki, K., Acceleration of the Reaction OH + CO → H + CO_2 by Vibrational Excitation of OH. *J Phys Chem A* **2011**, *115*, 4867-4873.

16. Burgh, E. B.; France, K.; McCandliss, S. R., Direct Measurement of the Ratio of Carbon Monoxide to Molecular Hydrogen in the Diffuse Interstellar Medium. *Astrophys J* **2007**, *658*, 446-454.

17. Fuente, A., et al., Gas Phase Elemental Abundances in Molecular Clouds (GEMS) I. The Prototypical Dark Cloud TMC 1. *Astron Astrophys* **2019**, *624*.

18. Harju, J.; Winnberg, A.; Wouterloot, J. G. A., The Distribution of OH in Taurus Molecular Cloud-1. *Astron Astrophys* **2000**, *353*, 1065-1073.

19. Eckhardt, A. K.; Bergantini, A.; Singh, S. K.; Schreiner, P. R.; Kaiser, R. I., Formation of Glyoxylic Acid in Interstellar Ices: A Key Entry Point for Prebiotic Chemistry. *Angew Chem Int Edit* **2019**, *58*, 5663-5667.

20. Hasegawa, T. I.; Herbst, E.; Leung, C. M., Models of Gas-Grain Chemistry in Dense Interstellar Clouds with Complex Organic-Molecules. *Astrophys J Suppl S* **1992**, *82*, 167-195.

21. Minissale, M.; Congiu, E.; Manico, G.; Pirronello, V.; Dulieu, F., CO_2 Formation on Interstellar Dust Grains: A Detailed Study of the Barrier of the CO Plus O Channel. *Astron Astrophys* **2013**, *559*.

22. Watanabe, N.; Mouri, O.; Nagaoka, A.; Chigai, T.; Kouchi, A.; Pirronello, V., Laboratory Simulation of Competition between Hydrogenation and Photolysis in the Chemical Evolution of H_2O-CO Ice Mixtures. *Astrophys J* **2007**, *668*, 1001-1011.

23. Cooke, I. R.; Sims, I. R., Experimental Studies of Gas-Phase Reactivity in Relation to Complex Organic Molecules in Star-Forming Regions. *ACS Earth Space Chem* **2019**, *3*, 1109-1134.

24. James, P. L.; Sims, I. R.; Smith, I. W. M.; Alexander, M. H.; Yang, M. B., A Combined Experimental and Theoretical Study of Rotational Energy Transfer in Collisions between NO($X\,^2\Pi_{1/2}$, v = 3, J) and He, Ar and N_2 at Temperatures Down to 7 K. *J Chem Phys* **1998**, *109*, 3882-3897.

25. Sims, I. R.; Queffelec, J. L.; Defrance, A.; Rebrionrowe, C.; Travers, D.; Bocherel, P.; Rowe, B. R.; Smith, I. W. M., Ultralow Temperature Kinetics of Neutral-Neutral Reactions - the Technique and Results for the Reactions CN+O_2 Down to 13 K and CN+NH_3 Down to 25 K. *J Chem Phys* **1994**, *100*, 4229-4241.

26. Western, C. M., PGOPHER: A Program for Simulating Rotational, Vibrational and Electronic Spectra. *J Quant Spectrosc Ra* **2017**, *186*, 221-242.

27. Nicovich, J. M.; Wine, P. H., Temperature-Dependent Absorption Cross-Sections for Hydrogen-Peroxide Vapor. *J Geophys Res-Atmos* **1988**, *93*, 2417-2421.

28. Vaghjiani, G. L.; Ravishankara, A. R., Photodissociation of H_2O_2 and CH_3OOH at 248 nm and 298 K - Quantum Yields for OH, O(^{3}P) and H(^{2}S). *J Chem Phys* **1990**, *92*, 996-1003.

29. Ondrey, G.; Vanveen, N.; Bersohn, R., The State Distribution of OH Radicals Photodissociated from H_2O_2 at 193 and 248 nm. *J Chem Phys* **1983**, *78*, 3732-3737.

30. Vaghjiani, G. L.; Turnipseed, A. A.; Warren, R. F.; Ravishankara, A. R., Photodissociation of H_2O_2 at 193 and 222 nm - Products and Quantum Yields. *J Chem Phys* **1992**, *96*, 5878-5886.

31. Tajti, A.; Szalay, P. G.; Csaszar, A. G.; Kallay, M.; Gauss, J.; Valeev, E. F.; Flowers, B. A.; Vazquez, J.; Stanton, J. F., Heat: High Accuracy Extrapolated Ab Initio Thermochemistry. *J Chem Phys* **2004**, *121*, 11599-11613.

32. Bomble, Y. J.; Vazquez, J.; Kallay, M.; Michauk, C.; Szalay, P. G.; Csaszar, A. G.; Gauss, J.; Stanton, J. F., High-Accuracy Extrapolated Ab Initio Thermochemistry. II. Minor Improvements to the Protocol and a Vital Simplification. *J Chem Phys* **2006**, *125*.

33. Harding, M. E.; Vazquez, J.; Ruscic, B.; Wilson, A. K.; Gauss, J.; Stanton, J. F., High-Accuracy Extrapolated Ab Initio Thermochemistry. III. Additional Improvements and Overview. *J Chem Phys* **2008**, *128*.

34. Thorpe, J. H.; Lopez, C. A.; Nguyen, T. L.; Baraban, J. H.; Bross, D. H.; Ruscic, B.; Stanton, J. F., High-Accuracy Extrapolated Ab Initio Thermochemistry. IV. A Modified Recipe for Computational Efficiency. *J Chem Phys* **2019**, *150*.

35. Shang, X.; Burd, T. A. H.; Clary, D. C., New Developments in Semiclassical Transition-State Theory. *J Phys Chem A* **2019**, *123*, 4639-4657.

36. Weston, R. E.; Nguyen, T. L.; Stanton, J. F.; Barker, J. R., HO+CO Reaction Rates and H/D Kinetic Isotope Effects: Master Equation Models with Ab Initio SCTST Rate Constants. *J Phys Chem A* **2013**, *117*, 821-835.

37. Shannon, R. J.; Blitz, M. A.; Goddard, A.; Heard, D. E., Accelerated Chemistry in the Reaction between the Hydroxyl Radical and Methanol at Interstellar Temperatures Facilitated by Tunnelling. *Nat Chem* **2013**, *5*, 745-749.

38. Sims, I. R.; Queffelec, J. L.; Travers, D.; Rowe, B. R.; Herbert, L. B.; Karthauser, J.; Smith, I. W. M., Rate Constants for the Reactions of CN with Hydrocarbons at Low and Ultra-Low Temperatures. *Chem Phys Lett* **1993**, *211*, 461-468.

39. Wakelam, V., et al., A Kinetic Database for Astrochemistry (KIDA). *Astrophys J Suppl S* **2012**, *199*.